Università degli Studi di Modena e Reggio Emilia

Dipartimento di Ingegneria "Enzo Ferrari"

Dottorato di Ricerca in
High Mechanics and Automotive Design & Technology
XXVIII Ciclo

ANALYSIS OF INNOVATIVE BURNERS FOR INDUSTRIAL KILNS

Relatore:
Prof. Mauro A. Corticelli

Direttore della Scuola di Dottorato:
Prof. Paolo Tartarini

Candidato:
Elia Agnani

A.A. 2014/2015

Alla mia famiglia

Contents

List of Figures

List of Tables

Abstract

The study and optimization of innovative burners for ceramic industries is presented in this thesis. These machines are widely employed in many applications such as dryers, gasification plants, boilers and continuous roller kilns for ceramic tiles.
In all these systems the energy is provided through the burners by means of fuel combustion. Unfortunately a large amount of this energy is usually wasted. In industrial kilns this is due both to thermal dissipation and the second principle of thermodynamics: when the exhaust gas into the chamber and the products of the firing process reach a thermal equilibrium, they cannot exchange more energy and the flue gas has to be expelled often at high temperature.
During the years many strategies have been developed in order to recover part of the wasted heat such as air recirculation inside the kiln form the hottest zone to the coolest one, or flue gas recycling in other systems of the factory. In particular this thesis focuses on recuperative burners. These burners are equipped with a built-in heat exchanger that recovers thermal power from hot gases, which are extracted from the kiln locally, through the burners themselves. The recovered heat is used for pre-heating combustion air. This process causes an increase in the flame temperature, so that in order to maintain the temperature of the mixture at a given value it is possible to decrease the amount of fuel provided to the system, thus saving energy and money.
The analysis of these systems is carried out by means of CFD (Computational Fluid Dynamics) instruments governed by optimization techniques, which in the recent

years have demonstrated to be valuable tools for the investigation of complex problems in a very efficient and economic way. Therefore the numerical model has been validated with experimental measurements and it has been exploited in a series of parametric simulation in order to optimize the burner's geometry and maximize the heat recovered from the flue gas.

However, one of the problem of recuperative burners is given by the formation of NO_x gases due to the higher flame temperature. Such a drawback can be mitigated by performing a staged combustion or by enhancing the turbulence in the domain, yet the most effective solution is represented by an exhaust recirculation system. With this application the flame's temperature is decreased and the NO_x drastically reduced.

Unfortunately such systems are not yet spread in industrial application due to the high complexity they introduce. In the final part of this thesis a prototype for a recirculation burner is also presented and investigated exploiting design of experiments techniques. This study represents a preliminary analysis of a technology that could be further developed and lead to interesting benefits.

Chapter 1

Introduction

Ceramic tiles are a common type of construction material widely used as floor and wall coverings. They basically derive from atomised clays shaped as thin slab and subjected to various treatments. During their manufacturing process they pass from the receipt and storage of the clays into silos to the delivering operations to the clients. In the middle there are the pressing process, where the raw materials are shaped, the drying operation and the firing process where the ceramic part is submitted to a thermal cycle in specific kilns. The firing process is responsible for endowing the tiles with specific technical and visual characteristic.

In recent years the demand for environmentally responsible industrial processes has considerably increased due to the unfortunately well known problems related to air pollution, global warming and climate change. According to [1], the firing process was identified as the most critical process in the tiles life cycle in terms of pollution and energy consumption.

The machines dedicated to the firing process are continuous roller kilns that can reach a few hundred meters in length. The product is fired by up to a thousand burners placed along the lateral surrounding walls above and below the tiles level (see Fig. 1.1). They expel hot gases at high temperature directly into the kiln room generating a large amount of thermal power, which is not easy to exploit in its entirety.

Figure 1.1: *Industrial continuous roller kiln*

Part of thermal power is dispersed across the furnace walls with peaks of heat losses through openings such as doors or slots. Another portion get lost with conveyor components like the rollers or the carts which enter the furnace cold and leave it at high temperature draining energy from the combustion gases. Also the cooling media, usually water or air, used to protect crucial elements of the kiln, contribute to the overall thermal waste.

All these losses are almost negligible if compared to the waste gas loss. Also known as flue gas loss, the waste gas loss consists of the thermal power that cannot be removed from the combustion gases that flows inside the kiln. This phenomenon is simply due to the second principle of thermodynamics: when combustion gases and product of firing process are at the thermal equilibrium they cannot exchange heat. So for example, if the ceramic products have to be heated to 900°C, the combustion gases cannot be cooled below this temperature and have to be discarded (exhaust gases).

Unfortunately the exhaust gases may still contain more than half of their initial energy depending on their temperature and the excess of air in combustion process.

Therefore possible energy saving solutions for industrial kilns deal with recovery of heat from exhaust gas. This heat can be used for other purpose without providing further energy to the systems. Moreover, recovering heat from exhaust gas implies a temperature drop, in this way specific filters can be placed along the chimney to efficiently absorb the pollutant agent. It is worth noting that a decrease in methane gas supply means a general reduction of annual costs for industries in addition to the already mentioned environmental advantages.

The thermal power of exhaust gases thus can be exploited for example in the drying process of the atomised clays slabs or, as it is usually done, to preheat the combustion air. Preheating combustion air is a common practice to increase the temperature of the flame and as a consequence it is possible to reduce the methane supply and obtain the same temperature of a system without air preheating. In terms of energy balance in a preheated system the enthalpy contribution of air is added to the one deriving from combustion process and, by increasing the former contribution, it is possible to reduce the latter.

In past years many systems have been developed to convey exhaust gases thermal power to combustion air, like regenerative and recuperative burners.

Regenerative burners use a media (ceramic balls or honeycomb) to store heat from waste gas and, after it is sufficiently heated, the combustion air is blown across it. In this way the heat is pulled out of the media and returned to the combustion process and thus less energy is discarded. In practice, as it is shown in Fig. 1.2, this kind of burners usually work in pairs. In this example the first burner is in firing mode with its combustion air blowing across the already hot media, resulting in air preheated temperature. On the other hand, the second burner is in heating mode, drawing the hot exhaust gases out of the kiln across its media, heating it up and cooling the waste gases. When the media of first burner is too cold and the one of the second burner has reached a decent temperature, the burners switch [3].

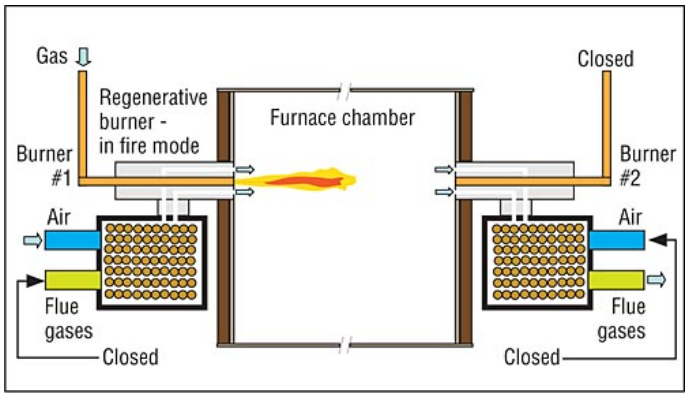

Figure 1.2: *Regenerative burners configuration*

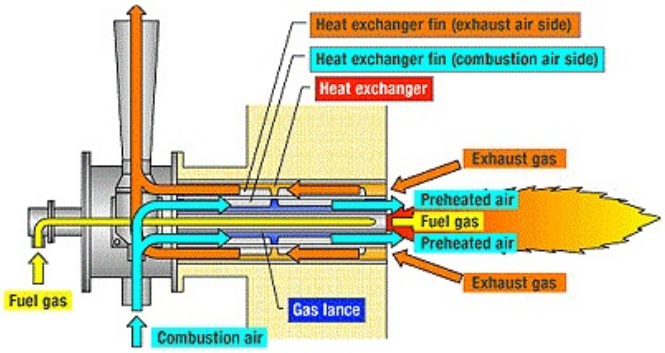

Figure 1.3: *Recuperative burner configuration*

In recuperative technology the combustion air is preheated by means of an heat exchanger installed inside the burner. The most common layout for this kind of system consists in a double pipe heat exchanger where the exhaust gas flows in an external coaxial tube placed around the burner body [2] as it is shown in Fig. 1.3.

Because of their compactness and easier management, recuperative burners have taken root more than the regenerative ones in the industrial sector. Nevertheless this technology can be further developed, therefore in this thesis an investigation of the heat exchanger shape has been performed in conjunction with an assessment of the performance in terms of recovered heat and saved fuel, in order to achieve a complete characterization of these systems.

However, recuperative burners are obviously not free of problems and downsides.

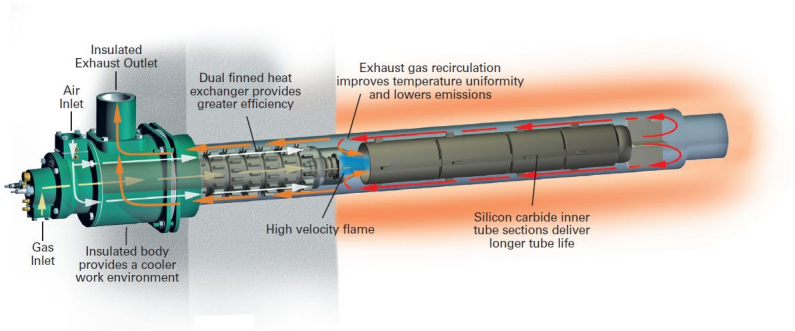

Figure 1.4: *Self-recuperative radiant burner.*

The main concern about them is represented by the larger NO_x formation rates induced by the higher flame temperatures occurring by pre-heating the combustion air. Some strategies that can help in mitigating this problem are represented by the enhancement of turbulence or the adoption of staged combustion [4], both realized in the classic layout of a recuperative burner.

Nevertheless, a more recent and effective solution, that has received increasing attention from researchers interested in burners is the flameless combustion [5]. This technique consists in the recirculation of a given amount of exhaust gases into the combustion chamber, so to smooth out the flame temperature peaks and reduce NO_x formation drastically [6]. Despite this, flameless combustion has not yet widely spread in industrial environment due to the additional complexity in the burner design given by the need of an exhaust gas recirculation system.

The only acknowledged application of this technology consists in radiant tube burner. In these systems the hot gas are expelled in a closed pipe and recirculated before being sucked through an extraction duct (Fig. 1.4). The flue gas are not spread (and wasted) inside the firing chamber and the heat transfer to the products occurs by means of radiation from incandescent tube.

Unfortunately the maximum reachable temperature of this systems is commonly below 1000 °C, which is not enough for ceramic tiles firing process.

Despite its limits, the exhaust gas recirculation is the most efficient techniques

that reduces NO_x formation and for this reason the second topic of this thesis concerns the preliminary analysis of a classic burner with an innovative geometry that can trigger a recirculation of flue gas.

The analysis realized in this thesis have been performed by means of Computational Fluid Dynamics (CFD), an instrument that has proved to be reliable and efficient, and can be considered a viable alternative to experiments in many industrial applications. For instance, CFD analyses have been carried out on cracking furnaces, with [7] and [8] mainly focusing on flow patterns and heat transfer in the firing zone, rather than on the burners. On the other hand, a paltry number of studies on continuous roller kilns in ceramic industry is available in literature. In [9] the temperature and velocity distributions on a module of an industrial kiln are investigated in terms of temperature uniformity on the tiles floor for different synthesis fuel gases used in place of methane. A general overview of a whole industrial furnace for ceramic tiles is given in [10], with regard to the evolution of temperature, pressure and oxygen content along the firing zone. The study gives also an esteem of the energy savings achievable by using the hot air from the cooling zone as combustive agent in the firing process. Non-recuperative industrial burners have been modelled by means of CFD in [11] to assess the behaviour of the system in terms of temperature, oxygen mass fraction and velocity distributions using different synthesis gases as fuel. The available literature on recuperative burners is still scanty, [12] and [13] modelled reheating furnaces used in steel industry and equipped with recuperative burners, showing the capability of CFD to provide information on these systems; however the heat exchanger is not simulated in its entirety and the focus is mainly on the furnace environment.

Chapter 2

Basics of Computational Fluid Dynamics

In this chapter the fundamental equations of Thermo-Fluid Dynamics are summarized. Then short overviews of turbulence, combustion and radiation modelling are presented with a particular focus on the methods used in this study. At last some notes on Finite Volume Method discretization and on existing CFD software are showed.

2.1 Governing Equations

In thermo-fluid dynamic problem the characteristic length and time scales are submitted to considerable changes and can be also very small, but they can still be considered larger than the discrete structure of matter. Therefore every physical property of interest can be described as a continuous function in macroscopic coordinates of time and space. This is the basic idea of continuum mechanics.

$$\phi = \phi(\mathbf{x}, \vartheta) \tag{2.1}$$

The general form of the equation that describes the rate of change in time and space for the generic physical property ϕ is:

$$\frac{\partial}{\partial \vartheta}(\rho\phi) + \nabla \cdot (\rho \mathbf{w} \phi) = \nabla \cdot (\Gamma \nabla \phi) + S \tag{2.2}$$

$$transition + convection = diffusion + source \tag{2.3}$$

All the governing equations of thermo-fluid dynamics can be written in the form of Eq. (2.2).

2.1.1 Continuity Equation

The continuity equation represents the expression of mass conservation principle. There is no diffusion of mass and this overview does not deal with mass generation inside the control volume, so the source term disappears. Therefore the continuity equation can be written as:

$$\frac{\partial \rho}{\partial \vartheta} + \nabla \cdot (\rho \mathbf{w}) = 0 \tag{2.4}$$

For steady-state problems the density does not change with time, so Eq. (2.4) becomes:

$$\nabla \cdot (\rho \mathbf{w}) = 0 \tag{2.5}$$

and if the fluid is incompressible:

$$\nabla \cdot (\mathbf{w}) = 0 \tag{2.6}$$

2.1.2 Momentum Equation

While continuity equation derives from the conservation of the mass in the continuum domain of interest, the momentum equation comes from the imposed equilibrium of the forces acting on the volume of fluid. These forces can have a volumetric origin (weight force) or they can act through the surfaces (viscous and pressure forces). The form of the resulting equation is:

$$\frac{\partial}{\partial \vartheta}(\rho \mathbf{w}) + \nabla \cdot (\rho \mathbf{w}\mathbf{w}) = \rho \mathbf{g} - \nabla p + \mu \nabla^2 \mathbf{w} + \frac{1}{3}\mu \nabla (\nabla \cdot \mathbf{w}) \tag{2.7}$$

which can be rewritten for each component of vector $\mathbf{w} = (w_x, w_y, w_z)$ in the incompressible case as:

$$\frac{\partial}{\partial \vartheta}(\rho w_x) + \nabla \cdot (\rho \mathbf{w} w_x) = \nabla \cdot (\mu \nabla w_x) + \rho g_x - \frac{\partial p}{\partial x} \tag{2.8}$$

$$\frac{\partial}{\partial \vartheta}(\rho w_y) + \nabla \cdot (\rho \mathbf{w} w_y) = \nabla \cdot (\mu \nabla w_y) + \rho g_y - \frac{\partial p}{\partial y} \tag{2.9}$$

$$\frac{\partial}{\partial \vartheta}(\rho w_z) + \nabla \cdot (\rho \mathbf{w} w_z) = \nabla \cdot (\mu \nabla w_z) + \rho g_z - \frac{\partial p}{\partial z} \tag{2.10}$$

Equations (2.8), (2.9), (2.10) respect the scheme of the transport of generic scalar equation (2.2).

2.1.3 Species Transport Equation

The equation for species transport is a fundamental instrument for most of combustion models. It calculates the local mass fraction (or the volume fraction) of each species Y_i inside the fluid mixture. The classic form of the transport equation is:

$$\frac{\partial}{\partial \vartheta}(\rho Y_i) + \nabla \cdot (\rho \mathbf{w} Y_i) = -\nabla \cdot \mathbf{J}_i + R_i + S_i \tag{2.11}$$

where $\mathbf{J}_i$ is the diffusion flux of the i specie and it is due to gradient of concentration and temperature in the mixture:

$$\mathbf{J}_i = -\rho \Gamma_{i,m} \nabla Y_i - \Gamma_{i,T} \frac{\nabla T}{T} \tag{2.12}$$

In Eq. (2.12) the first term is related to the diffusion of species i into the mixture, while the second takes into account the effects of temperature in the diffusion process. The R_i term in Eq. (2.11) represent the net rate of production for the species i due to the chemical reactions modelled. It is also called reaction rate and it will be discussed in more detail in § 2.3.

2.1.4 Energy Equation

The thermal energy equation comes from the first principle of thermodynamics and thus from an equilibrium between incoming, outcoming and generated energy in a finite volume of fluid. The form of the equation written in terms of temperature is [15]:

$$\frac{\partial}{\partial \vartheta}(c_p \rho T) + \mathbf{w} \cdot \nabla (c_p \rho T) = \nabla \cdot (\lambda \nabla T) + S_v \tag{2.13}$$

In this case the transport quantity is the thermal conductivity λ which derives from Fourier's law.

More general formulations of energy equation can be found in [14] and [16] and includes also energy transport due to species diffusion

$$\frac{\partial}{\partial \vartheta}(\rho E) + \nabla \cdot (\rho E \mathbf{w}) = -\nabla \cdot (p\mathbf{w}) + \nabla \cdot \left[\lambda \nabla T - \sum_i h_i \mathbf{J}_i \right] + S_v \tag{2.14}$$

where $\mathbf{J}_i$ is the species diffusion coefficient expressed in Eq. (2.12).

2.2 Turbulence Modelling

Turbulence is not a casual phenomenon. Navier-Stokes equations, in conjunction with continuity equation, are able to describe a turbulent flux in its entirety with a good level of accuracy. From a computational point of view, turbulence should be described as a chaotic event more than a casual one, it is a deterministic phenomenon extremely sensible to the initial and boundary conditions. This is due to the fact that in a turbulent flux viscous forces are not able to oppose the inertia of the fluid and also a small perturbation on the system gets indefinitely propagated instead of being damped like in an ordinary laminar regime.

One distinctive character of turbulence is the great variety of space and time scales that go from the macroscopic dimensions of the problem to microscopic sizes with the Reynolds number increasing. The turbulent problem and the energy transmission between different scales have been studied in the past by Kolmogorov. In fact he defined the *energy cascade* theory which asserts that the energy owned by the flux (which comes from external agent, like a pressure gradient) is transmitted from the bigger vortices that collapse in small ones until the smallest dimension is reached and the residual energy is dissipated through viscous friction. The smallest space scale, called Kolmogorov scale, depends on Reynolds according to this relation:

$$\eta \approx \frac{L}{Re^{\frac{3}{4}}} \tag{2.15}$$

where L is the dimension of the biggest scale. Eq. (2.15) shows clearly the wide range of space scale and the strong dependence of the smallest one on the Reynolds number.

In a similar way it is possible to obtain the velocity of the Kolmogorov scale to have a idea of the time scale of turbulence:

$$\nu \approx \frac{u}{Re^{\frac{1}{4}}} \tag{2.16}$$

In order to discretize in the right way the physical domain and solve all the scales that characterize a certain flow field, the number of elements should be too large and the dimension of time step too small, leading to an overall computational weight that is not of practical engineering interest.

Therefore different approaches have been proposed to the turbulence problem and the three of major interest are discussed below:

- DNS (*Direct Numerical Simulation*): as the name indicates, this is the direct approach to the problem, the closest to the real physics of the problem. The smallest scales are solved without models and for this reason the computational weight is very high. This approach has not yet a real industrial application due to its complexity but it is a fundamental tool for the investigation of detailed turbulent phenomena.

- LES (*Large Eddy Simulation*): this approach is based on the idea that the biggest scales depend directly on the studied system, due to their high energy content they have their own properties and behaviour and so they have to be solved in their entirety. On the other hand, the Kolmogorov scales have more generic characteristics, which are independent from the investigated case and thus can be modelled. The governing equations are hence filtered in space with a moving average, which deletes all the small fluctuations. This operation leads to the appearance of a new term in Navier-Stokes equations, the *Sub-Grid Stress* term, that take into account the macroscopic effects of the fluctuations ignored by the filter. The LES models present different formulation for the *Sub-Grid Stress* term based on the filtered variables. The computational weight decreases with this approach but it is still too much for industrial purposes and thus it is not yet spread in this contest.

- RANS (*Reynols Averaged Navier-Stokes*): the simplest approach, but also the less accurate. It uses averaged quantities in space and time and this operation

generates non-linear sub-grid terms than have to be modelled. The computational complexity is drastically reduced and despite their lack of accuracy these models are the most used for industrial applications. The simulations carried out for this thesis make large use of RANS models and then they are discussed in the next session.

2.2.1 Reynolds-Averaged Navier-Stokes Approach

For simplicity in this section the governing equations are rewritten with the Einstein notation, which implies summation on terms with repeated indexes. Therefore the continuity and Navier-Stokes equations become:

$$\frac{\partial \rho}{\partial \vartheta} + \frac{\partial}{\partial x_j}(\rho w_j) = 0 \tag{2.17}$$

$$\frac{\partial}{\partial \vartheta}(\rho w_i) + \frac{\partial}{\partial x_j}(\rho w_i w_j) = -\frac{\partial p}{\partial x_i} + \frac{\partial}{\partial x_j}\left[\mu\left(\frac{\partial w_i}{\partial x_j} + \frac{\partial w_j}{\partial x_i}\right)\right] \tag{2.18}$$

According to the Reynolds averaging technique, every quantity ϕ can be decomposed as a combination of mean value and fluctuation:

$$\phi(x_i, t) = \overline{\phi}(x_i, t) + \phi'(x_i, t) \tag{2.19}$$

with $\overline{\phi'} = 0$ for every type of average.

The governing equations (2.17) and (2.18) can be rewritten after the application of the filter:

$$\frac{\partial(\rho \overline{u}_i)}{\partial x_i} = 0 \tag{2.20}$$

$$\frac{\partial}{\partial \vartheta}(\rho \overline{w}_i) + \frac{\partial}{\partial x_j}(\rho \overline{w}_i \overline{w}_j + \rho \overline{w'_i w'_j}) = -\frac{\partial \overline{p}}{\partial x_i} + \frac{\partial}{\partial x_j}\left[\mu\left(\frac{\partial \overline{w}_i}{\partial x_j} + \frac{\partial \overline{w}_j}{\partial x_i}\right)\right] \tag{2.21}$$

Due to its non-linearity, averaging the Navier-Stokes equations, cause the formation of a new term $\rho\overline{w'_i w'_j}$ (called *Reynolds stresses*) that has to be modelled. It is common to consider it as an additional viscous term:

$$-\rho\overline{w'_i w'_j} = \mu_t\left(\frac{\partial \overline{w}_i}{\partial x_j} + \frac{\partial \overline{w}_j}{\partial x_i}\right) - \frac{2}{3}\rho\delta_{ij}k \tag{2.22}$$

The RANS equations become then:

$$\frac{\partial}{\partial \vartheta}(\rho \overline{w}_i) + \frac{\partial}{\partial x_j}(\rho \overline{w}_i \overline{w}_j) = -\frac{\partial \overline{p}}{\partial x_i} + \frac{\partial}{\partial x_j}\left[(\mu + \mu_t)\left(\frac{\partial \overline{w}_i}{\partial x_j} + \frac{\partial \overline{w}_j}{\partial x_i}\right)\right] - \frac{2}{3}\rho \delta_{ij} k \quad (2.23)$$

where μ_t is called *turbulent viscosity*, it is a characteristic of the flux (not of the fluid as the molecular viscosity), varies in space and time and takes into account the effects of the *Reynolds stresses* ignored by the filter. The last term of the second member of Eq. (2.23) is necessary to respect mass conservation, the k term is the *turbulent kinetic energy*.

Therefore the core of the problem is the calculation of the turbulent viscosity (also called eddy viscosity) coefficient. In the last decades many strategies have been proposed, it is possible to assemble them depending on the number of additional transport equations implemented:

- *Algebraic Models*: also called *zero-equations models*, in this kind of models the eddy viscosity is computed directly from flow filtered variables. They are very fast and simple but they make use of empirical closure coefficient and hence they lack in accuracy when applied to general situations. They represent a valuable tool when modelling simple flow geometry or as initialization application. The most known algebraic models are the Cebeci-Smith and the Baldwin-Lomax models.

- *One-equation models*: as the name suggests in these models just one transport equations is solved. Usually it is associated to the turbulent kinetic energy k like in the Prandtl's model, but also other quantities can be solved, for example the Spalart-Allmaras model implements a transport equation for the modified turbulent viscosity variable $\tilde{\mu}$.

- *Two-equations models*: in these models other turbulent quantities in addition to the turbulent kinetic energy are solved through a transport equation with

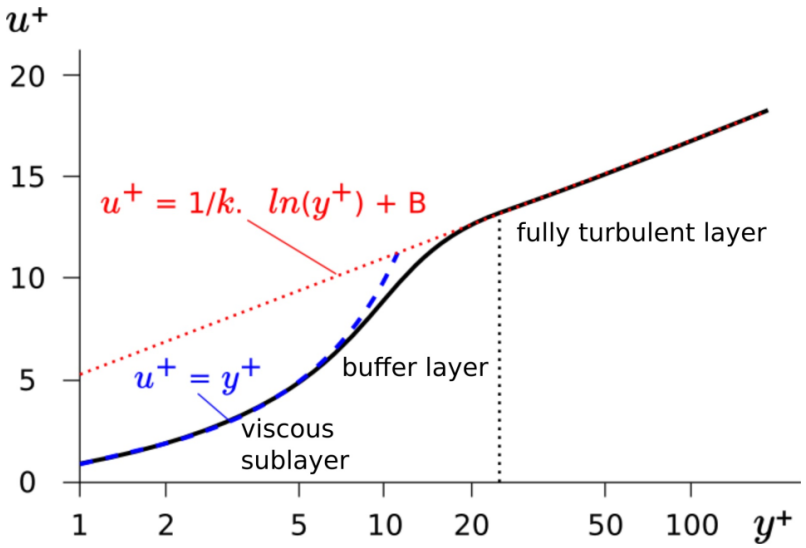

Figure 2.1: *Different layers in the near-wall region of a turbulent flow.*

appropriate terms that take into account generation, dissipation, convection and diffusion. With these models it is possible to achieve a decent level of accuracy for a wide range of systems and problems. The most used two-equation models are the k-epsilon, that associates a transport equation for the quantity ϵ (called turbulent dissipation rate), and the k-omega, that solves an additional equation for the quantity ω (called specific dissipation rate). In this thesis a particular k-omega model, the k-omega SST model, is used, which is explained in more details in § 2.2.2.

The use of RANS methods implies the adoption of particular boundary conditions for the walls. The turbulent boundary layer can be completely computed or it can be modelled with appropriate *wall functions*. It is common to observe three different layers in the near-wall region of a turbulent flow as shown in Fig. 2.1. The inner layer, also called *viscous sublayer*, is characterized by an almost laminar flow ruled by the molecular viscosity. In the outer region, also called *fully-turbulent layer*, turbulence plays a fundamental role, while in between (*buffer layer*) both effects are valuable.

In order to investigate the near-wall problem from a universal point of view, the following dimensionless quantities are defined (they are also used in Fig. 2.1):

$$y^+ = \frac{yu_\tau}{\nu} \tag{2.24}$$

$$u^+ = \frac{u}{u_\tau} \tag{2.25}$$

where y is the distance from the wall, u is the velocity of the fluid at y distance from the wall and $u_\tau = (\tau_w/\rho)^{1/2}$ is called *friction velocity*.

As mentioned before there are two different approaches to solve the near-wall region:

- *low Reynolds*: with this approach the turbulent boundary layer is completely computed through the inner layer. The turbulence models have to be modified in order to take into account the presence of the wall with appropriate damping functions and the grid should be adequate for the problem with the first cell characterized by an $y^+ < 1$. This results in a very fine grid and a heavy computational weight which are not always affordable.

- *high Reynolds*: in this case the flow in the viscous and buffer layer is not resolved, so it is necessary to use *wall functions* in order to correlate the near-wall information with the flow data in the fully-turbulent region. This approach requires lower computational costs, but to obtain acceptable results the assumptions for the use of *wall functions* have to be respected and the centroid of the first cell has to be characterized by an $y^+ > 30$.

2.2.2 k-omega SST Model

One of the most appreciated models for industrial applications is the k-omega SST (*Shear Stress Transport*), which have been widely used in the simulation carried out for this thesis. This approach implements two additional transport equation, the first one dedicated to the turbulent kinetic energy and the second one that solves

the ω quantity, called *specific dissipation*, that can be thought of as the variable related to the scale of the turbulent phenomenon.

Its strength relies in the capability to combine two different approaches with a complex set of blending functions controlled by the traits of the flux and the distance from the wall. In particular this model goes gradually from a standard k-omega in the inner layer to a modified k-epsilon in the fully-turbulent region. Therefore it is possible to adopt a *low Reynolds* approach without any damping functions exploiting the robustness and accuracy of k-omega model in the inner layer, while for the far field the k-epsilon model allows to avoid a series of problems due to the high sensitivity of k-omega to the free-stream conditions. The implemented transport equations are:

$$\frac{\partial(\rho k)}{\partial \vartheta} + \frac{\partial(\rho \overline{w}_i k)}{\partial x_i} = \frac{\partial}{\partial x_j}\left(\left(\mu + \frac{\mu_t}{\sigma_k}\right)\frac{\partial k}{\partial x_j}\right) + G_k - Y_k \tag{2.26}$$

$$\frac{\partial(\rho \omega)}{\partial \vartheta} + \frac{\partial(\rho \overline{w}_i \omega)}{\partial x_i} = \frac{\partial}{\partial x_j}\left(\left(\mu + \frac{\mu_t}{\sigma_\omega}\right)\frac{\partial \omega}{\partial x_j}\right) + G_\omega - Y_\omega + D_\omega \tag{2.27}$$

In the diffusion terms the turbulent viscosity μ_t and the turbulent Prandtl numbers σ_k and σ_ω are defined as:

$$\mu_t = \frac{\rho k}{\omega}\frac{1}{max\left[\frac{1}{\alpha^*}; \frac{SF_2}{a_1 \omega}\right]} \tag{2.28}$$

$$\sigma_k = \frac{1}{\frac{F_1}{\sigma_{k,1}} + \frac{1-F_1}{\sigma_{k,2}}} \tag{2.29}$$

$$\sigma_\omega = \frac{1}{\frac{F_1}{\sigma_{\omega,1}} + \frac{1-F_1}{\sigma_{\omega,2}}} \tag{2.30}$$

where F_1 and F_2 are the blending functions mentioned before. They affect also the production terms (G_k and G_ω), the dissipation terms (Y_k and Y_ω) and the cross-diffusion term (D_ω). Their form is not reported in this thesis but is deeply discussed in appropriate documents.

2.3 Combustion Modelling

Combustion is a very complex process that involves a strong coupling between chemistry and fluid dynamics. Fuel and oxidant are mixed together and react with an exothermic behaviour producing a self-sustainable flame. This phenomenon has a great importance in the analysis of burners, its fundamental concepts are briefly reported in this section, for a wide review of the problem the readers can look at more specific works [16].

2.3.1 Flame Classification

In the study of combustion problems it is a common practice to divide flame types in premixed, partially premixed and non-premixed [17], [16].

- **Premixed**: fuel and oxidizer are mixed at a molecular level, a thin reaction zone (flame thickness) divide burnt and unburnt gases. A typical example of premixed combustion is represented by aspirated internal combustion engines.
- **Non-premixed**: fuel and oxidizer enter the combustion zone in different streams, they are also called diffusion flames because the burning rate is mainly controlled by diffusion of reactants towards the reaction zones. Typical examples of non-premixed combustion are diesel internal combustion engine and also the burners which are the topic of this thesis.
- **Partially premixed**: intermediate characteristics between non-premixed and premixed, in those flames fuel and oxidizer are imperfectly mixed at inlets and the combustion is partially controlled by diffusion processes.

Another fundamental classification is made between laminar and turbulent flames. Typical industrial systems deal with turbulent combustion and so do the burners analysed in this thesis.

The turbulence directly affects the diffusion terms of governing equations, different combustion regimes can be individuated depending on the interaction between turbulence and chemistry. A dimensionless number is introduced to describe the properties of a turbulent flame, the Damkohler number, defined as [17]:

$$Da = \frac{\tau_t}{\tau_c} \tag{2.31}$$

where τ_t represents the turbulent time scale and τ_c the chemical time scale.

- **Da** $>>$ **1**: for high Damkohler numbers the chemical time is short compared to the turbulent one, in this regime the assumption of very fast chemistry can be done, the reaction zone results very thin and the reaction rates are controlled by turbulent structures that wrinkle and strain the flame surface (mixing limited).

- **Da** $<<$ **1**: low values of Damkohler number correspond to a slow chemical reaction, the turbulence affects the reaction zone mixing reactants and products at molecular level. The mean reaction rates can be expressed from detailed Arrhenius laws

In most practical situations Damkohler number assumes medium or high values, especially when dealing with fuel oxidation which is characterized by very short chemical time scales ($Da >> 1$), while pollutant formation (CO or NO_x) are generally slower.

2.3.2 Numerical Models

There is a large variety of combustion models available in literature, some of them are implemented in the most widespread commercial CFD software. They can be summarized in three main categories:

- **Premixed Combustion Models**: these models solve transport equations for scalars related to the typical structure of a premixed flames. For example

the *C-equation* model deals with a reaction progress variable, called c, which assumes the value of zero for unburnt reactants and one for the burnt products.

- **Non-Premixed Combustion Models**: developed specifically for diffusion problems, these models exploit some features of non-premixed flames to solve the governing equations avoiding complex chemical calculations. The most common approach introduces a conserved scalar, the mixture fraction, defined as the mass fraction originated from fuel stream. The related transport equation does not contain a source term, combustion is reduced to a mixing problem and non-linear reaction rates calculation is avoided.

- **Finite-Rate Chemistry**: species transport equations are solved for each species in the mixture. The reaction rate terms are calculated with different approaches depending on the level of interaction between turbulence and chemistry.

In order to avoid simplifications and obtain a detailed map of the major components of the mixture, in this thesis the last family of models has been employed and it is now discussed with further details.

The common goal of these models is the definition of the R_i term in Eq. (2.11), related to the net rate of production of species i by chemical reaction. This term can be defined in different ways [14], depending on the turbulent combustion regime and on the level of accuracy that the users want to achieve.

- **Laminar Finite-Rate Model (FR)**: calculates the reaction term with the classic Arrhenius expression, ignoring effects of turbulent fluctuations. For the species i in a reversible reaction r the reaction term $R_{i,r}$ can be computed as:

$$R_{i,r} = \Gamma(\nu''_{i,r} - \nu'_{i,r}) \left(k_{f,r} \prod_{j=1}^{N} [C_{j,r}]^{\nu'_{j,r}} - k_{b,r} \prod_{j=1}^{N} [C_{j,r}]^{\nu''_{j,r}} \right) \tag{2.32}$$

where,

N = number of species in the system

$\nu'_{i,r}$ = stoich. coeff. of reactant i in reaction r

$\nu''_{i,r}$ = stoich. coeff. of product i in reaction r

Γ = represents the effect of third bodies

$C_{j,r}$ = molar concentration of species j in reaction r

$k_{f,r}$ = forward rate constant for reaction r

$k_{b,r}$ = backward rate constant for reaction r

The forward rate constant is defined with the Arrhenius expression

$$k_{f,r} = A_r T^{\beta_r} e^{-E_r/RT} \tag{2.33}$$

where A_r, β_r and E_r are quantities that depend on the type of reaction involved and are not easy to set in a proper way.

This model is designed for laminar flames and it is inapplicable to turbulent flames but it can still be accepted for slow chemistry problems ($Da << 1$).

- **Eddy-Dissipation Model (ED)**: proposed by Magnussen [18], this model compute the reaction term with the assumption of very fast chemistry ($Da >> 1$). The process in mixing controlled, complex and often unknown chemical kinetic rates can be neglected and reaction term is related to turbulent quantities:

$$R_{i,r} = A\nu'_{i,r} M_{w,i} \rho \frac{\epsilon}{k} min\left(min_R \left(\frac{Y_R}{\nu'_{R,r} M_{w,R}} \right), B \frac{\sum_P Y_P}{\sum_j^N \nu''_{j,r} M_{w,j}} \right) \tag{2.34}$$

where,

A, B = constants of the model

$M_{w,i}$ = molecular weight of the species i

Y_P = mass fraction of any product species P

Y_R = mass fraction of a particular reactant R

ϵ = turbulent dissipation rate

k = turbulent kinetic energy

This model is very fast and stable but has some disadvantages, in particular the combustion proceeds whenever turbulence is present and for this reason it does not need an ignition and it can't capture local extinctions. Furthermore the fuel consumption is overestimated and the temperatures are locally too high.

- **Finite-Rate Eddy-Dissipation (FR/ED)**: a combination of FR and ED, for each cell the reaction rate is computed with the two methods and the minimum is taken to solve the governing equations. This model is able to choose locally between chemistry- and mixing- controlled combustion, it is applicable to a wide range of problems but it does not take into account the turbulence/chemistry interaction.

- **Eddy-Dissipation Concept (EDC)**: extension of the ED Model in which the interaction between turbulence and chemistry is fully implemented. The results are very accurate and the range of applicability very wide, but computational time are consistently increased.

2.4 Radiation Modelling

When dealing with combustion problems radiation effects cannot be neglected because of the high temperatures that come into play. The net radiant heat flux has a fourth order dependence on temperatures and can be estimated as:

$$Q_{rad} = \sigma(T_{max}^4 - T_{min}^4) \tag{2.35}$$

Radiative heat transfer is generally described by the following transport equation:

$$\frac{dI(\mathbf{r},\mathbf{s})}{ds} + (a+\sigma_s)I(\mathbf{r},\mathbf{s}) = an^2\frac{\sigma T^4}{\pi} + \frac{\sigma_s}{4\pi}\int_0^{4\pi} I(\mathbf{r},\mathbf{s}')\Phi(\mathbf{s},\mathbf{s}')d\Omega' \tag{2.36}$$

where,

I = radiation intensity

$\mathbf{r}$ = position vector

$\mathbf{s}$ = direction vector

a = absorption coefficient

σ_s = scattering coefficient

n = refractive index

There are many radiation model in literature, in the following paragraphs the two models used in this thesis are briefly described.

2.4.1 P-1 Radiation

The P-1 radiation model comes from the family of the P-N models, which are based on the spherical harmonic expansion of radiation intensity I. The model is quite simple, Eq. (2.36) is reduced to a diffusion equation very easy to solve and based on the incident radiation G

$$\nabla\cdot(\Gamma\nabla G) - aG + 4an^2\sigma T^4 = S_G \tag{2.37}$$

where

$$\Gamma = \frac{1}{(3(a+\sigma_s) - C\sigma_s)} \tag{2.38}$$

The radiation flux q_r can be directly computed from incident radiation G with the relation:

$$q_r = -\Gamma \nabla G \tag{2.39}$$

and it can be substituted into energy equation, closing the problem.

As mentioned above, this model is very simple and it can be resolved with little CPU demand. It includes effects of scattering and it can be applied to complicated geometries. On the other hand, some limitations of this model are the assumption of diffuse surfaces and the lack of reliability in problems with medium characterized by low values of optical thickness $(a + \sigma_s)s$), as it may occur in some combustion systems with opaque flue gases.

2.4.2 Discrete Ordinates

With Discrete Ordinates radiation model, Eq. (2.36) is solved for a finite number of directions in space chosen by user. This model is the most complete and it is applicable to every practical problem, it spans the entire range of optical thicknesses and it is also well suited for combustion problem. On the other hand the computational weight of this model can heavily increase if the chosen spatial discretization is too dense. The radiative transfer equation for the direction $\mathbf{s}$ becomes:

$$\nabla \cdot (I(\mathbf{r}, \mathbf{s}), \mathbf{s}) + (a + \sigma_s) I(\mathbf{r}, \mathbf{s}) = an^2 \frac{\sigma T^4}{\pi} + \frac{\sigma_s}{4\pi} \int_0^{4\pi} I(\mathbf{r}, \mathbf{s}') \Phi(\mathbf{s}, \mathbf{s}') d\Omega' \tag{2.40}$$

2.5 Finite Volume Method

vAlmost all the governing equations presented in the previous paragraphs cannot be solved in an analytical way, but it is possible to obtain an acceptable approximated solution on a discrete computational domain. In this section a general overview of the Finite Volume Method (FVM) is given, leaving a more detailed discussion on the topic to specific books [15], [19].

In every governing equation is possible to identify recurrent terms: a time-dependent term, one related to advection, one to diffusion and finally a source term. It is then possible to define the general scalar transport equation as:

$$\frac{\partial}{\partial \vartheta}(\rho\phi) + \nabla \cdot (\rho \mathbf{w}\phi) = \nabla \cdot (\Gamma \nabla \phi) + S \tag{2.41}$$

The FVM is the most widespread integration method for partial differential equation in fluid dynamics for its simplicity and its closeness to the first principles of conservation. An algebraic system is obtained from the integration of the balance equations on each control volume of the domain.

2.5.1 Discretization of the Equations

In every control volume V_{ij} of a bi-dimensional computational grid an integral equation can be written in the form:

$$\int_{V_{ij}} \left[\frac{\partial}{\partial \vartheta}(\rho\phi) + \nabla \cdot (\rho \mathbf{w}\phi) - \nabla \cdot (\Gamma \nabla \phi) - S \right] dV = 0 \tag{2.42}$$

that can be simplified as:

$$\int_{V_P} \frac{\partial}{\partial \vartheta}(\rho\phi) dV + \int_{S_P} (\mathbf{J} \cdot \mathbf{n}) dS + \int_{V_P} S dV = 0 \tag{2.43}$$

where $\mathbf{J} = \rho\phi\mathbf{w} - \Gamma\nabla\phi$ and $\mathbf{n}$ represents the direction normal to surface.

It is possible to define each term of the Eq. (2.43) as a function of the variable computed in the cell-centres of the surrounding elements. The final product of this

operation is an algebraic equation in the form:

$$A_P\phi_P^{n+1} + A_E\phi_E^{n+1} + A_W\phi_W^{n+1} + A_N\phi_N^{n+1} + A_S\phi_S^{n+1} = \tilde{S}_P^n \tag{2.44}$$

where the $n+1$ superscript identifies the unknown variables in the temporal step t_{n+1}, while in the right hand side, the n superscript is for known quantities at the last time step t_n. It is possible to write one algebraic equation for every cell of the computational domain. All equations written together and modified by the boundary conditions contribute to generate the resolving system of the fluid dynamic problem.

2.5.2 Pressure-Velocity Coupling

Governing equations are non-linear and strongly coupled one to another because of the advection term that contains velocity information. The fluid dynamic problem has then to be solved in an iterative way and during the years many methods have been developed. These methods can be summarized in segregated methods and coupled methods. The fundamental steps of the two methods are shown in Fig. 2.2:

- **Segregated**: the individual governing equations are solved sequentially (in a segregated way one from another). The properties are calculated from the current solution, the momentum equations are solved and the flow field is then modified with the pressure correction equation in order to respect the balance of mass (continuity equation). After that all other quantities and scalars are updated. Examples of segregated algorithms are SIMPLE, SIMPLEC and PISO methods [19].

- **Coupled**: with this method momentum and pressure correction equation are solved simultaneously in a fully coupled solving system. The convergence of the solution is improved compared to the segregated method, but the memory

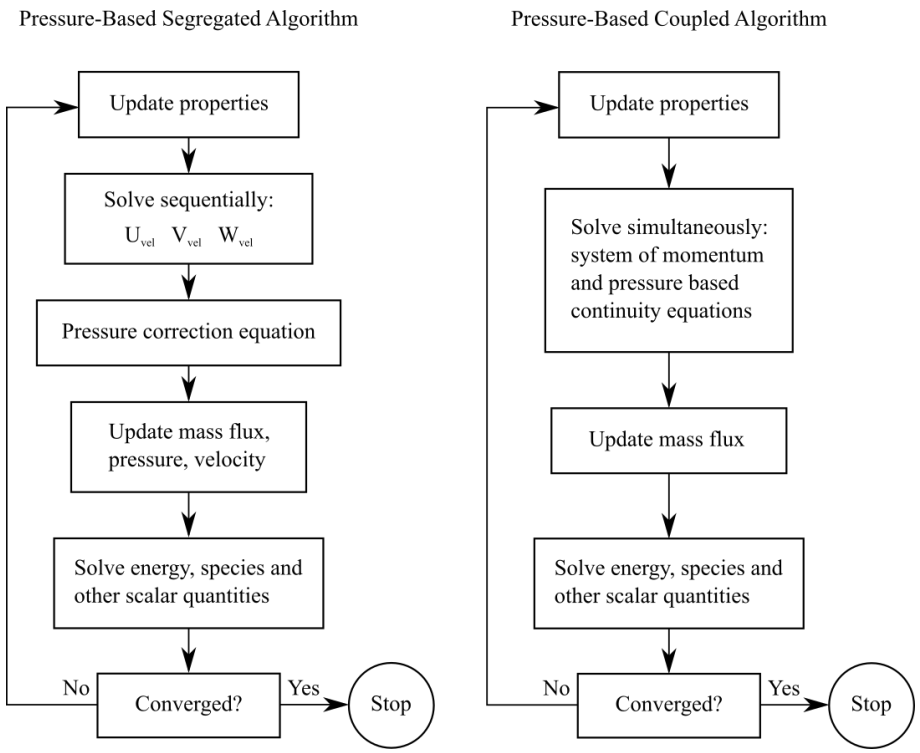

Figure 2.2: *Schematics of the segregated and the coupled solving algorithm*

demand is increased. The remaining governing equations (energy, species, turbulence, ecc.) are solved in a decoupled way, as in segregated algorithms.

2.6 CFD Software

All governing equations, discretization and solving methods are implemented in many CFD software packages. In this thesis two different software have been exploited, with different features and for different goals.

- **OpenFOAM**: free and open source code, it is not yet widespread in industrial environments because of its steep learning curve. This software has a lot of capabilities, it is able to deal with compressible and incompressible flows, energy equation is then implemented such as multi-phase and multi-region solvers. In this thesis it has been used for the simplest models, where a lot of tests have been done and the absence of a license turned out to be very convenient.

- **ANSYS Fluent**: for the complete models of the burners it was necessary to use this commercial code. Very reliable and expensive it provides models and algorithms for the full range of the possible fluid dynamics problems. With Fluent it was possible to develop simulations with radiation, combustion and turbulence on a domain with fluid and solid zones.

Chapter 3

Basics of Optimization Techniques

In recent years a lot of interest has risen around the topic of optimization. Its powerful and versatile techniques can be applied to a wide range of disciplines from engineering to biology at academic or industrial level.

In Fig. 3.1 the typical steps of an optimization process are highlighted [20]. The first aspects deal with the definition of the problem that is *what should be optimized*. After that, there are the input variables that fully characterize the problem and affect its performance. The performance has to be evaluated in order to link input and output and this could be done either in experimental or numerical way.

The n chosen input variables define a n-dimensional Euclidean geometrical space called *design space* and a set of input variables can be seen as a dot in this space and it is called *sample*. From experiment or numerical simulations is then possible to obtain output parameters, which are functions of the input variables. The output parameters then define one or more objective functions in the solution space (or they can be themselves an objective function). The aim of optimization is to minimize (or maximize) these objective functions. Therefore optimization techniques are a set of criteria to state the goodness of a certain sample and generate a new one *ad-hoc* in order to achieve the minimum (or maximum) of the objective function.

In the next section the concept of *Design of Experiment* (DOE) is presented, it is not an optimization technique itself, but it is related to the way of choosing

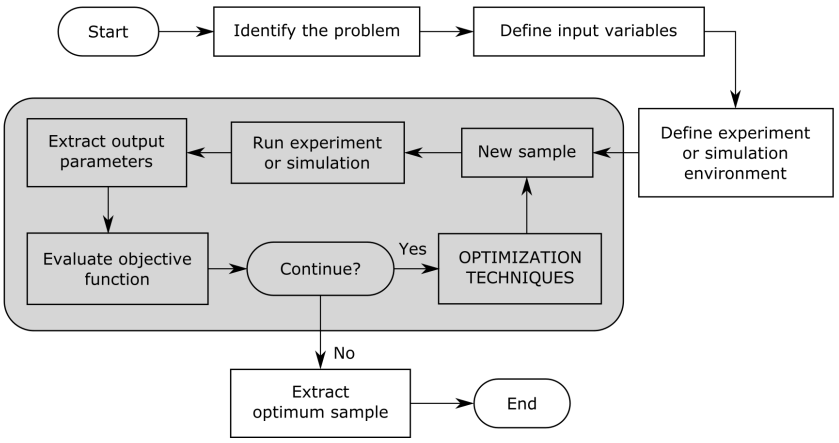

Figure 3.1: *Flowchart of a typical optimization process.*

samples in the design space in the most efficient ways. Whereas in the final section real optimization techniques are briefly described.

3.1 Design of Experiment

Experimental procedures, such as numerical simulations, can take a lot of time and resources. A rigorous optimization process require a large number of samples to converge and find a solution and for this reason it is often inapplicable to certain types of problem, such as CFD ones.

However it is possible to obtain enough information with a limited number of simulations (samples) properly chosen in the design space. The aim of DOE is exactly to obtain the maximum amount of information using the minimum amount of samples and, hence, of resources.

Usually the DOE analysis is followed by a *Response Surface Modelling* (RSM). This topic will be discussed in § 3.2 and it consists of an optimization on a mathematical surface obtained from the interpolation of samples results. It is a very fast technique, but its reliability strongly depends on the quantity and the quality of

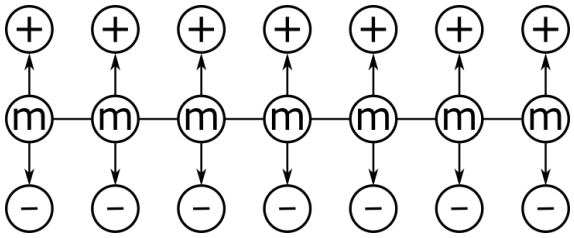

Figure 3.2: *Example of star-point DOE approach.*

chosen points in the design space. The distribution of samples is due to the adopted DOE approach.

3.1.1 Star-points

The star-point method is very simple and fast, hence the information it returns can be considered incomplete and fragmented. Nevertheless in many problems this approach is applied in order to quickly study the individual influence of each parameter and leave out from further analysis the negligible ones.

The founding criterion of this method in fact consists in changing every parameters from its minimum ($-$) to its maximum ($+$) starting from a medium value (m). As it is shown in Fig. 3.2 for each sample just one parameter is changed and all the others are fixed at m value. Therefore for N input parameters the total number of simulations/experiments needed to complete a star-point DOE is $2 \cdot N + 1$ and it is called *sample size* of the method.

The name star-point comes from the schematic visualization of the sample size. As shown in Fig. 3.3, the chosen design points with two input parameters remind the tips of a star.

With this method just three levels can be tested for each variable ($-$, m, $+$) and no mutual influence between parameters is investigated. For this reason it can be considered a good approach in the first phases of a new project in order to under-

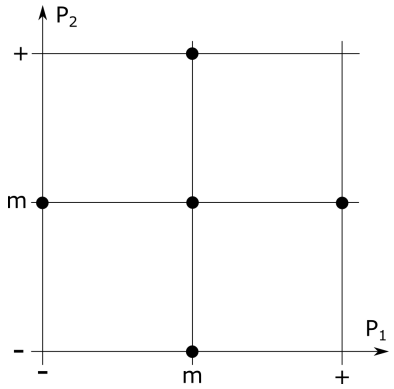

Figure 3.3: *Schematic visualization of star-point DOE approach with two input variables.*

stand the importance of individual parameters, but it is not designed for detailed approach like RSM.

3.1.2 Full-factorial

Full factorial approach, as opposed to star-point, contemplates a lot of design point resulting in a sample size that can be very large. All the possible combination between the chosen levels of each parameter are tested. In general, named n_1, n_2, ... n_k the levels of discretization of the k input variables of the problem, the sample size can be calculated as $n_1 \cdot n_2 \cdot ... \cdot n_k$.

For example, as shown in Fig. 3.4, with $k = 2$ variables and respectively $n_1 = 3$ and $n_2 = 4$, the sample size amount to $3 \cdot 4 = 12$. Unfortunately the number of design points grow very fast, with $k = 5$ variables, each one discretized in $n = 3$ levels, the sample size can be calculated as $3^5 = 243$.

Therefore this method can be considered a brute force approach. In fact, by increasing the number of levels for each input variable is possible to obtain a rich and complete filling of the design space that results in a highly reliable RSM. On the other hand this accuracy is achieved with a large and inefficient number of tests, which often translates to high levels of money and resources wasting.

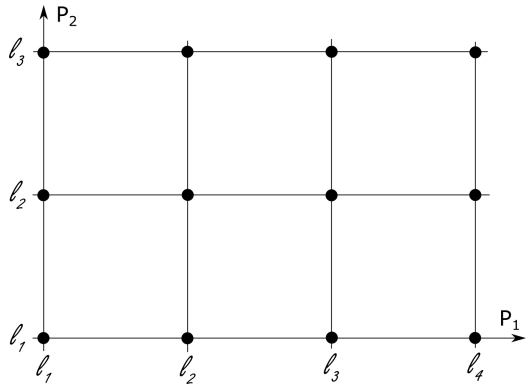

Figure 3.4: *Schematic visualization of full-factorial DOE approach with two input variables and different levels.*

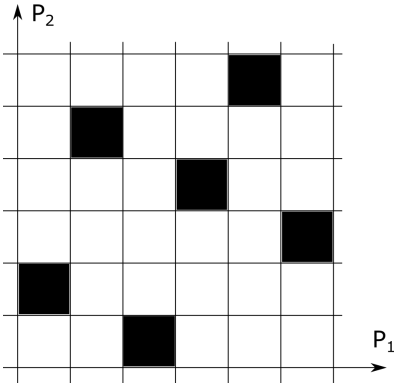

Figure 3.5: *Schematic visualization of latin-hypercube DOE approach with two input variables and six samples.*

3.1.3 Latin-hypercube

With latin-hypercube approach it is possible to fill the design space in a decent way without realizing an exceeding number of tests. In this method the user has to choose the number N of samples he wants to (or he can afford to) evaluate and the algorithm allocates them around the design space in the most efficient measure.

Each parameter interval is subdivided in N segment in order to create a multi-dimensional grid into the design space. Within this grid N sub-volumes are detected so that along each row and column only one sub-volume is chosen. Then a random sample is individuated inside each sub-volume.

An example is shown in Fig. 3.5 for a problem with $k = 2$ input parameters and $N = 6$ samples, the typical crossword-like graphical representation of the latin-hypercube scheme is highlighted. With dedicated algorithms [21] it is possible to ensure an uniform and efficient samples distribution within the design space and avoid any significant correlations (for example around the diagonal of a bi-dimensional design space).

3.2 Response Surface Modelling

The basic idea of Response Surface Modelling (RSM) is to create an analytical approximation of the objective function over the design space starting from the samples of the DOE analysis. Although it is just an approximation the response surface is related to the input parameters and can be instantly evaluated without needing new simulations or experiments. Usually an optimization process is carried out on the response surface because thousands of samples can be evaluated in few minutes.

However it is important to consider that the optimum sample found is based on an approximation and thus it strictly depends on the design space exploration which has been performed in the DOE analysis. Moreover, if the response function is particularly irregular, also a complete and efficient DOE approach can miss some local minimum or maximum which will not be included in the analytical response surface.

In order to avoid these problems, a common practice is to test the optimum found on the response surface with a new simulation or experiment. Then it is possible to check the predictive capability of the model and if it is necessary the new sample can be added to the original design points family in order to obtain a more accurate response surface.

3.3 Optimization

The aim of optimization is to generate new samples for the iterative process previously shown in Fig. 3.1. The existing algorithms can be divided in two main families according to the principles by which they suggest new samples in order to achieve the minimization (or maximization) of the objective function.

- **Deterministic Optimization**: the algorithms of this family strongly relies on linear algebra and are commonly based on the calculation of the gradient (and in some case of the Hessian matrix) of the objective function. The main advantage of these algorithm is their relative fast convergence to the optimum solution in terms of the low number of samples (simulations/experiments) needed to complete the process. On the other hand these methods are not free from drawbacks: for example, driven by the gradient progress, they can get stuck in local minimum (or maximum). Moreover this kind of algorithms is intrinsically single objective. In § 3.3.1 is presented the Simplex Method, one of the most efficient and reliable deterministic optimization algorithm, which has been exploited in this thesis.

- **Stochastic Optimization**: the primary characteristic of these methods is the introduction of random criteria in the optimization process. Another interesting fact is the way in which the randomness is implemented in the algorithm: through natural processes imitation. In fact, the leading role in stochastic optimization has to be acknowledged to evolutionary and genetic algorithms. These curious names come from the working principle of the methods, where an initial population of samples evolves up to the optimum, in the same way in which from the monkey we arrived to the *Sapiens Sapiens* (in this case maybe more steps are needed for the full convergence!). There are also methods that adopt a different nature-mimicking approach based on the replication of the

collective behaviour of self-organized community of the animal kingdom, such as ant or bee colony. They are also known as *Swarm Intelligence* algorithms. It is common to say that the advantages of this family of optimization algorithms relies in the thorough exploration of the design space, while the noticeable drawback is the slow convergence. This is generally true because the intrinsic randomness of the algorithms avoids stuck in local minima (or maxima) with the casual generation of new samples that can also be far from their parents in a continuous exploration of the design space. However, with specific control parameters of the algorithms, it is possible to balance between speed of convergence and design space exploration. Furthermore it is possible to implement multi-objective research. For this reason such methods are very reliable but also flexible and in the last years have been widely used in many research field. In § 3.3.2 the basic working principle of genetic algorithms are presented as they have been exploited in this thesis.

3.3.1 Nelder and Mead Simplex

The simplex method was originally introduced by Spendley [22] in 1962 and then it has been improved by Nelder and Mead [23] in 1965. In general a simplex is a geometrical figure defined by $k+1$ vertices in a k-dimensional space. The first step in the process consists in the definition of $k+1$ samples which locate a simplex in the design space. Then the objective function is evaluated at each vertex and the results are compared. The following procedures yield to continuous transformation of the simplex into the design space until it sticks around the optimum value found (that could also be a local minimum or maximum because this is a deterministic algorithm).

There are different mechanisms that move the simplex. Denoting $\mathbf{x}_{k+1}$ the point to be transformed and $\mathbf{x}_0$ the centroid of other k vertices, there are:

- **Reflection**: the worst sample is reflected through the centroid of other k vertices, the new point is

$$\mathbf{x}_r = \mathbf{x}_0 + \alpha(\mathbf{x}_0 - \mathbf{x}_{k+1}) \tag{3.1}$$

- **Contraction**: if after the reflection the new sample $\mathbf{x}_r$ is still the worst (becoming the $\mathbf{x}_{k+1}$ vertex for this operation), the simplex is contracted and the new point is computed with

$$\mathbf{x}_c = \mathbf{x}_{k+1} + \rho(\mathbf{x}_0 - \mathbf{x}_{k+1}) \tag{3.2}$$

- **Expansion**: if after reflection the new sample becomes the best, it is pushed further along the $\mathbf{x}_r$-$\mathbf{x}_{k+1}$ direction

$$\mathbf{x}_e = \mathbf{x}_0 + \gamma(\mathbf{x}_0 - \mathbf{x}_{k+1}) \tag{3.3}$$

- **Shrinking**: if a vertex $\mathbf{x}_1$ is sufficiently old (never changed in the last m operations), then the simplex can be shrunk and the new points ($i = 2, ..., k+1$) become

$$\mathbf{x}_i = \mathbf{x}_1 + \sigma(\mathbf{x}_i - \mathbf{x}_1) \tag{3.4}$$

The terms α, ρ, γ and σ mentioned in previous equations are the reflection, contraction, expansion and shrinking coefficients and their typical values are: $\alpha = 1$, $\rho = 0.5$, $\gamma = 2$ and $\sigma = 0.5$. Although this method is not characterized by a fast convergence, it is very useful for noisy and irregular objective function due to its robustness.

3.3.2 Multi-Objective Genetic Algorithm

Before talking about *Multi-Objective Genetic Algorithm* a small introduction to the main concepts of evolutionary and genetic algorithms has to be done. Both of them aim at finding the optimal solution by simulating the evolution of a population

through successive generation of better performing individuals. Basically the new generation is created by applying some operators to their parents of the previous generation.

The thin but fundamental difference between evolutionary and genetic algorithms just relies in the operator which is used. In fact evolutionary methods are mainly based on the *mutation* operator: one mutant individual is created for each member of the population, combining its information with those coming from its parents a trial individual is defined and finally the best between trial and parent is kept for the next generation.

On the other hand in genetic algorithms the evolution process is mainly due to cross-over operators. Therefore it is a common practice to encode the input variables into binary strings and the individual is then represented with a sort of chromosome composed of zeros and ones. For that purpose the design space has to be discretized in such a way that the number of values the variables can assume in an integer power of 2, in order to realize the binary representation.

For example, for a problem with two input variables x_1 and x_2, which attain values between 0 and 1, the range of x_1 is discretized into $2^2 = 4$ nodes, while x_2 into $2^3 = 8$ nodes. The design space then allows $2^2 \cdot 2^3 = 2^5 = 32$ possible solutions regularly dislocated in a grid shape. Now every individual of the population can be represented as a string made by 5 (the integer power of 2) bits. Because of the parallelism with genetics, the string is also called chromosome and the bits are the alleles. One possible individual for the considered example could have a chromosome of 10110, which can be seen 10-110 by highlighting the two different genotypes that corresponds to the phenotypes $x_1 = 0.667$ and $x_2 = 0.857$ following the scheme shown in Tab. 3.1. In general, the main steps of a genetic algorithm are:

- **Initialization**: the first population is generated on the discretized design space and the objective function (also called *fitness function*) is evaluated for

Table 3.1: *Binary vs. real representation of input variables for genetic algorithm optimization.*

x_1		x_2	
Binary	Real	Binary	Real
00	0.000	000	0.000
01	0.333	001	0.143
10	0.667	010	0.286
11	1.000	011	0.429
		100	0.571
		101	0.714
		110	0.857
		111	1.000

each point.

- **Crossover**: a new generation of children is defined with the following process:
  - two parents are randomly selected, however the probability of being selected is not the same for each member of the population. The most common rules adopted in the selection process are:
    - *roulette-wheel selection*: the probability of being chosen is proportional to the fitness of the individual
    - *tournament selection*: few individuals are randomly selected to take part to the tournament, they are ranked according to their fitness. The best has a probability p_t of winning the tournament and be selected, the second best has a probability of $p_t \cdot (1 - p_t)$, the third best of $p_t \cdot (1 - p_t)^2$ and so on. Typical values for the probability p_t lies in range 0.5, 1.0.
  - the cross-over operator is applied with the probability p_c and the offspring is generated. If no cross-over takes place, the children are the copies of their parents. The probability p_c is generally high, around 0.90. There

are different cross-over operators, the most common are the *one-point cross-over*, the *two-point cross-over* and the *uniform cross-over*, which are explained in Fig. 3.6.

- **Mutation**: each allele of each child has a quite low probability of being switched from o to 1 or vice-versa. The probability p_m is usually around 0.01 because, as mentioned before, genetic algorithms are mainly trained by cross-over operators rather than mutations.

- **Offspring**: the previous generation is completely replaced by the new one, which is evaluated in terms of fitness function.

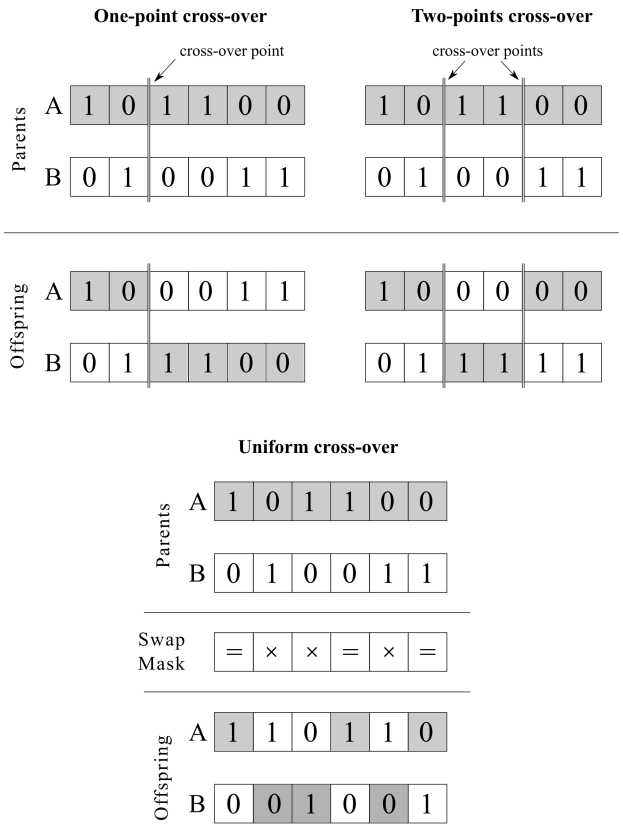

Figure 3.6: *Representation of different cross-over operators.*

Different choices in input variables discretization or method control parameters (such as p_c, p_m or p_t) can heavily affect the behaviour and the results of the algorithm. Between the non-ordinary operators, one of the most popular, which is often included in genetic algorithms is the *elitism operator*. Its mechanism allows the most performing individual in the population to survive through successive generations.

The working principles of MOGA are the same presented above, except for some measures in order to handle the multi-objective characteristic. In particular the selection operators are included in this modification: in a roulette-wheel selection, for example, the probability of an individual of being selected is proportional to its distance to the *Pareto frontier*; while the probability of winning the tournament, in the namesake operator, is higher for the individuals that lie on the *Pareto frontier*. Elitism operators are often adopted in these methods in order to increase the probability of a generation to be addressed to the *Pareto frontier*.

Chapter 4

The Recuperative Burner: Analysis and Optimization

4.1 Current Design of the Burner

In the introductory chapter the principal features of recuperative burners have been presented. Basically with these machines it is possible to exploit part of the waste power, contained in exhaust gases, to preheat combustion air and increase the mean temperature of the mixture. Then, in order to bring temperature back to ordinary values, a certain amount of fuel can be preserved.

The amount of saved fuel can be roughly estimated with a simplified approach. The adiabatic flame temperature of a methane-air mixture at 25°C with an air excess of 20% is approximately 1800°C; if the inlet temperature of the products is raised by 100°C, in order to obtain again the same mean flame temperature it is possible to save about 5% of fuel. Then, ideally, if the temperature of the products could be increased by 300°C, the saving of fuel could reach 17%.

Unfortunately, the standard control systems of industrial burners are not yet very sophisticated and, to avoid quenching or flame separation phenomena, the flow rate of natural gas fed into the process is not reduced as expected by theoretical calculations. This inaccuracy causes an increase in the mean temperature of the mixture and a consequent raise in NO_x production. However, the higher tempera-

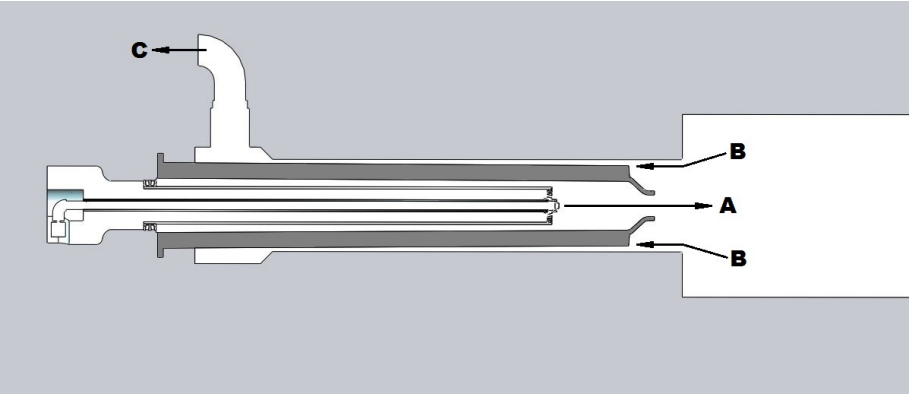

Figure 4.1: *Sketch of the investigated recuperative burner. Exhaust gases flow around the burner body through B and are expelled in C. Preheated mixture comes out from A.*

tures have a positive effect on the quality of the firing process, since the fluid velocity at the burner's mouth is increased, the penetration capability of the hot jet into the kiln room is improved and the mixing is enhanced, resulting in a more uniform temperature distribution.

The burner presented in this chapter (Fig. 4.1) has been designed to generate about 13 kW of thermal power; its basic working principles are the same mentioned above for general recuperative burners. Air and methane are fed into the system at ambient temperature, the natural gas flows directly towards the burner's head, while the combustion air is split in *primary* and *secondary* (or *external*) streams before entering the heat exchange zone, as it is shown in Fig. 4.2. Primary air flows in the inner part of the burner, just around the methane tube and it can also be called *internal*. The secondary air is forced to stream in an annular duct between the primary air and the solid body of the burner. The burner's solid body, made by silicon infiltrated silicon carbide (SiSiC), acts also as heat exchanger. The exhaust gases flow around it counter-currently, releasing part of their thermal power to secondary air.

The design of the burner, then, reflects in general the classical recuperative burners layout, however it differs from the common state of the art because of two

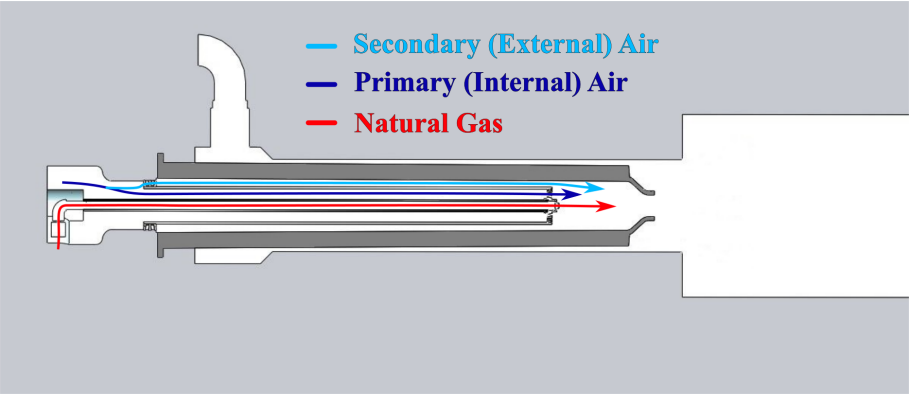

Figure 4.2: *Scheme of the three streams in the recuperative burner investigated.*

distinctive features:

- **Swirl effect**: with a specific component, a swirl motion is impressed to the secondary air that flows near the heat exchanger in order to enhance the amount of recovered thermal power. For that reason, a preliminary study of the influence of swirl effect on the Nusselt number of annular ducts has been carried out and it is presented in § 4.2.

- **Heat exchanger**: as reported above, heat is exchanged through the burner's body, whose shape has to be studied carefully in order to increase the amount of recovered thermal power. A number of solutions have been presented in past years and most of them are patent protected, the one proposed for this case involves an heat exchanger with longitudinal fins (Fig. 4.3). This particular geometry has been preliminarily investigated with a simplified model governed by a direct optimization process and the results are shown in § 4.3.

The aim of the project is the enhancement of the heat recovered from exhaust gases by modifying some geometric parameters. Therefore, after the theoretical studies mentioned above, it has been necessary to develop a simulation of the entire system, which is presented in § 4.4. Then, an experimental campaign has been carried out in order to validate the numerical model and the results are summarized in § 4.5.

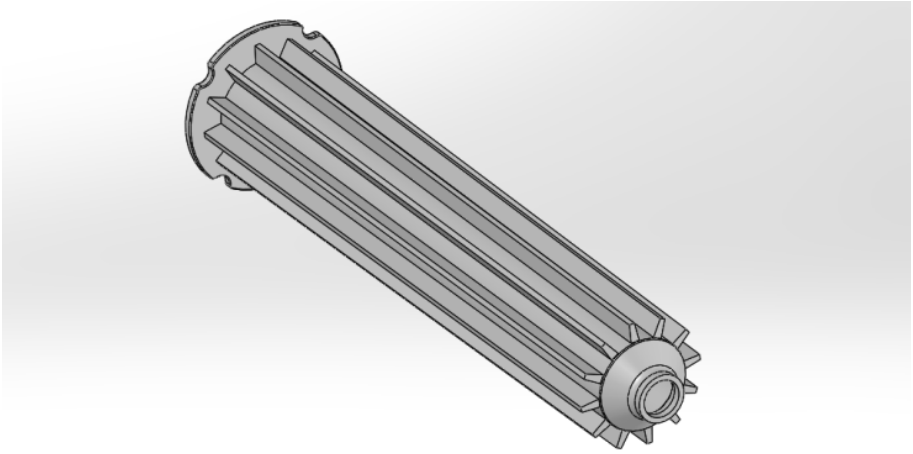

Figure 4.3: *Heat exchanger with longitudinal fins.*

Unfortunately, due to the high computational requirements of the complete simulation, a direct optimization has been considered unaffordable for the purpose of the study. In § 4.6 the approach adopted, based on DoE techniques, is presented and the best burner configuration found is described.

As final past of the project, in § 4.7 the recuperative burner has been scaled in order to generate 50 kW of thermal power, testing the above approach on a system of larger size.

4.2 Correlation for the Convective Heat Transfer Coefficient for Swirling Flows in Annular Pipes

In this section the influence of the swirl effect on heat transfer is investigated in the case of flux through an annular pipe. The simplified system described represents a portion of the macro-system analysed in this chapter.

The thermal power exchanged is proportional to h [W/m^{2}K], the convective heat transfer coefficient, following the Newton's Law

$$\dot{Q} = hA(T_{bulk} - T_s) \tag{4.1}$$

where A is the heat transfer surface, T_{bulk} is the bulk temperature of the fluid and T_s is the surface temperature. The convective heat transfer coefficient is in turn related to the dimensionless Nusselt number

$$\mathrm{Nu} = \frac{hL}{\lambda} \tag{4.2}$$

where L is a characteristic length of the problem and λ [W/mK] is the thermal conductivity of the fluid.

As it will be explained in next sections the Nusselt number can be estimated with empirical correlations taking into account other dimensionless numbers for the specific class of problems. Unfortunately there is a lack of references in literature about the influence of swirl motion on such correlations.

Therefore, it has been necessary to propose a new correlation for the Nusselt number, which have been calibrated with numerical simulations varying some specific parameters.

4.2.1 Existing Correlations

The literature abounds of empirical correlations for the Nusselt number. These correlations, like the Nusselt number itself, depend on the type of fluid, on its flow

regime (forced or natural convection, laminar or turbulent) and on the geometry of the problem. For those reasons, other dimensionless numbers are taken into account, such as:

- **Reynolds number**: ratio between the inertia of the flow and the viscous dissipation.

$$\mathrm{Re} = \frac{uL}{\nu} \tag{4.3}$$

  where u and L are characteristic velocity and dimension of the problem and ν is the kinematic viscosity. This number gives information on the regime of the flow, typically it is laminar for $\mathrm{Re} < 2300$ and fully turbulent for $\mathrm{Re} > 10000$.

- **Prandtl number**: related to the fluid, it measures the ratio between the momentum and the heat diffusion, for gases it can be considered constant with temperature

$$\mathrm{Pr} = \frac{c_p \mu}{\lambda} = \frac{\nu}{\alpha} \tag{4.4}$$

  where c_p is the specific heat of the fluid, μ its dynamic viscosity and α its thermal diffusivity.

In case of buoyancy driven flows, also the Rayleigh or the Grashof numbers are included in empirical correlations. However all the systems considered in this thesis are in forced convection conditions, so the buoyancy aspects are not treated in this work.

As mentioned above, the empirical correlations depend also on the geometry of the problem. In the following list the most known correlations for circular and annular pipes are presented with their characteristics.

- **Dittus-Boelter correlation**

$$\mathrm{Nu} = 0.023 \cdot \mathrm{Re}^{0.8} \cdot \mathrm{Pr}^{n} \tag{4.5}$$

where $n = 0.3$ for cooling of the fluid ($T_s < T_{bulk}$) or $n = 0.4$ for heating of the fluid ($T_s > T_{bulk}$). This correlation is valid for fully turbulent flows ($\mathrm{Re} > 10000$) in smooth tubes, it does not take into account high temperature variations and for this reason it is inaccurate when large temperature gradients occur across the flow.

- **Gnielinski correlation**

$$\mathrm{Nu} = \frac{(f/8)(\mathrm{Re} - 1000) \cdot \mathrm{Pr}}{1 + 12.7 \cdot (f/8)^{0.5} \cdot (\mathrm{Pr}^{2/3} - 1)} \tag{4.6}$$

where f is the Darcy friction factor that can be estimated, for instance, with Petukhov equation as $f = [0.79 \cdot \ln(\mathrm{Re}) - 1.64]^{-2}$. This alternative formulation for Nusselt number is also valid for transient flow regimes with $\mathrm{Re} > 3000$ but it lacks in temperature dependence as Dittus-Boelter equation does.

- **Sieder-Tate correlation**

$$\mathrm{Nu} = 0.027 \cdot \mathrm{Re}^{0.8} \cdot \mathrm{Pr}^{1/3} \cdot (\mu_{bulk}/\mu_s)^{0.14} \tag{4.7}$$

where μ_{bulk} is the dynamic viscosity of the fluid evaluated at bulk temperature, while μ_s is the dynamic viscosity of the fluid evaluated at the surface temperature. This formulation takes also into account the effects of high temperature gradients and can be considered more accurate than others. On the other hand its solution is not trivial because it is an implicit function due to the fact that the viscosities change as the Nusselt number (and hence the temperatures) changes.

- **Sudarev correlation**

$$\mathrm{Nu} = 0.0319 \cdot [1 + \tan(\vartheta)]^{0.77} \cdot \mathrm{Re}^{0.8} \tag{4.8}$$

where ϑ is the inclination angle of the flow, and then $\tan(\vartheta)$ is the ratio between the tangential and the axial velocities. This correlation was proposed

by Sudarev [24] after a series of experiments with air at highly turbulent regimes in annular pipes.

4.2.2 Numerical Model

In order to develop a new Nusselt correlation, a large database of experiments or numerical simulations is required, so that the resulting interpolation is as accurate as possible.

In this thesis the numerical simulation has been chosen as instrument to investigate the problem. This is for sure cheaper than an experimental infrastructure but it is not problem-free. An accurate numerical model could require an expensive computational grid and a lot of time to be solved. For this reason great attention had to be dedicated to the set-up of the simulation.

For the purpose of the study, a completely automatic calculation infrastructure was developed, which was able to generate the geometry and the mesh, update the boundary conditions, run the simulation and perform the post-processing to obtain the desired control quantities. All the process was governed by a python script with optimization and DoE techniques implemented.

Because of the presence of the swirl, it has not been possible to exploit the axisymmetry of the problem. Then, an entire annular duct was used in the calculations; however, thanks to specific periodic boundary conditions, just 5 diameters in length were considered.

OpenFOAM was chosen as the CFD simulation software; it was described in § 2.6. The software makes it possible to set-up a parametric model able to realize a fully hexahedral mesh with the *blockMesh* utility, as shown in Fig. 4.4.

With appropriate scripts the size of the domain and also the grid refinement could be varied, depending on the boundary conditions implemented. In this way it was possible to create a low-Re mesh (see § 2.2.1) for all the analysed cases. The grid sizes were very diverse, depending on inlet velocity condition: in the extreme

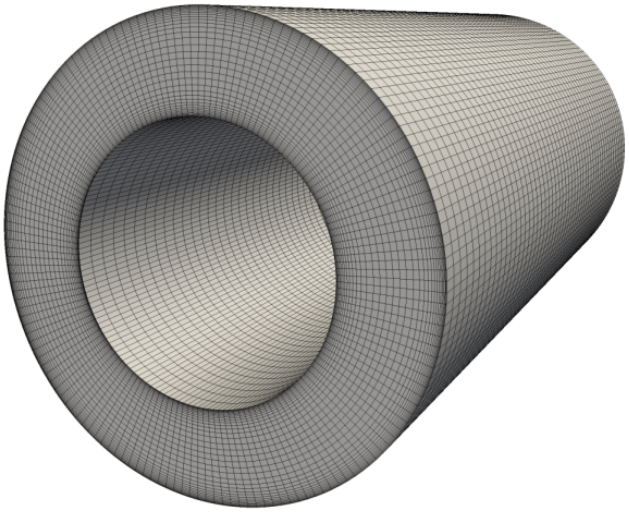

Figure 4.4: *Computational grid of the annular duct realized with blockMesh utility.*

cases, they reached 4 millions of elements, taking more than 24 hours of calculation on a normal workstation with 4 CPUs.

For what concerns the boundary conditions, they were automatically varied and imposed with dedicated scripts. The following considerations have been done:

- **Inlet & Outlet**: a series of *mapped* conditions were implemented. As the name suggests, with this particular conditions the quantities at the outlet are mapped on the inlet patch. This set-up is often used to obtain fully developed profiles (of velocity or temperature) at the inlet, allowing to model just a short portion of the entire pipe. In this case, turbulent quantities were exactly mapped from outlet to inlet, while the temperature was adjusted at the inlet in order to maintain the outlet profile scaled on a fixed specific value. Also the velocity had to be treated differently because the swirl component tended to decay along the pipe. Therefore the axial component of the outlet velocity was mapped at the inlet and an appropriate tangential component was added to obtain the desired angle.

- **Walls**: fixed temperature boundary conditions were implemented for internal and external walls.

The last step in the automatic work-flow infrastructure was the post-processing. At the end of the simulation, a series of quantities were evaluated and extracted from the model, in order to calculate the mean Nusselt number resulting from the simulation. First of all the bulk temperatures at inlet and outlet were computed as

$$T_{bulk,[in/out]} = \frac{\int_{A_{[in/out]}} \rho U_{ax} T c_p dA_{[in/out]}}{\int_{A_{[in/out]}} \rho U_{ax} c_p dA_{[in/out]}} \tag{4.9}$$

where $A_{[in/out]}$ is the surface area (of inlet or outlet) and U_{ax} the axial component of the velocity. With the bulk and the surface temperatures T_s a mean logarithmic temperature difference ΔT_{ml} was calculated as

$$\Delta T_{ml} = \frac{(T_{bulk,in} - T_s) - (T_{bulk,out} - T_s)}{\ln \frac{(T_{bulk,in} - T_s)}{(T_{bulk,out} - T_s)}} \tag{4.10}$$

and it was used to calculate the mean h coefficient with

$$h = \frac{\dot{Q}_{tot}}{(A_{tot} \cdot \Delta T_{ml})} = \frac{(\dot{Q}_{int} + \dot{Q}_{ext})}{(A_{w,int} + A_{w,ext}) \cdot \Delta T_{ml}} \tag{4.11}$$

where $\dot{Q}_{int}$ and $\dot{Q}_{ext}$ are the thermal powers across the internal, $A_{w,int}$, and the external, $A_{w,ext}$, surface of the annular duct; these quantities could be obtained directly from simulations.

The mean convective heat transfer coefficient was then used to compute the mean Nusselt number with Eq. (4.2), where the chosen characteristic length of the problem was the hydraulic diameter of the duct, obtained as the difference between external D_{ext} and internal D_{int} diameters $D_h = D_{ext} - D_{int}$. The thermal conductivity depends on temperature and was evaluated with the Chapman-Enskog formulation [25] as

$$\lambda = \mu(1.32 c_p + 0.45 R) \tag{4.12}$$

where c_p is the specific heat computed with JANAF coefficients at mean bulk temperature between inlet and outlet $\bar{T}_{bulk}$. R is the gas constant, which assumes the value of 287.05 for air, while μ is the dynamic viscosity still calculated at the mean bulk temperature with the Sutherland formulation

$$\mu = \frac{1.5072 \cdot 10^{-6}(\bar{T}_{bulk}^{1.5})}{\bar{T}_{bulk} + 123.37} \tag{4.13}$$

All these operations were performed automatically and the final results were the mean Nusselt number Nu and the mean convective heat transfer coefficient h which could be related to the input variables in order to obtain the interpolating correlation.

4.2.3 Design of Experiment

The purpose of this preliminary work was to define a new correlation for the Nusselt number which can take into account the effect of the flux swirl component. This correlation was obtained with an interpolation over a large series of results deriving from numerical simulations. Therefore, the simulation database has to be wide but also dense, in order to cover properly all the regions of the design space and obtain a reliable correlation. First of all the input parameters have been defined:

- **Reynolds number**: probably the most influential parameter, it gives information on the regime of the flow and cannot be neglected. It has been varied between 3000 and 1 million with 7 levels properly scaled in order to cover this wide range with a sufficient discretization degree (Tab. 4.1).

- **Temperature difference**: the influence of the temperatures has been taken into account, as in Sieder-Tate formulation. In particular, 4 temperature differences have been considered in case of cooling of the fluid, and 3 for the case of heating of the fluid (Tab. 4.1).

Table 4.1: *Definitive input parameters and their ranges of variability.*

Reynolds number	3000, 5000, 10000, 30000 $1 \cdot 10^5$, $3 \cdot 10^5$, $1 \cdot 10^6$
Temperature difference ($T_{bulk} - T_s$)	$\pm$10, $\pm$100, $\pm$300, 500°C
Swirl angle	15°, 30°, 45°, 60°

- **Swirl angle**: the innovative aspect of the correlation is that it embodies the swirl angle influence. The 4 levels shown in Tab. 4.1 have been chosen. It is unusual to consider slopes greater than 60 degrees in order to avoid an excessive raise in concentrated pressure losses.

- **Diameters ratio**: a preliminary analysis has been conducted to asses the influence of the diameters ratio D_e/D_i on the Nusselt number. This term does not appear in known empirical correlation (such as Dittus-Boelter or Sudarev) and also in this case, according to the results, it could be neglected.

A first set of simulations with straight air was developed to validate the numerical model. Reynolds numbers ≥ 10000 have been tested with the temperature differences for a total of $5 \times 7 = 35$ runs. Qualitative contours of temperature and velocity are shown in Fig. 4.5, the swirl effect is clearly highlighted with vector representation at the inlet of the annular duct.

The data fitting technique implemented will be explained in the next section; in this paragraph the results of the validation are shown. A correlation in the Sieder-Tate form was adopted (Re, Pr and μ_{bulk}/μ_s dependance) and the coefficients that fitted the simulation data with the minimum average error were

$$\mathrm{Nu} = 0.021 \cdot \mathrm{Re}^{0.8} \cdot \mathrm{Pr}^{1/3} \cdot (\mu_{bulk}/\mu_s)^{0.27} \tag{4.14}$$

In this case the average error was 6% and the max error 14%. If the original Sieder-Tate coefficients (see Eq. (4.7)) were implemented, the average interpolation error

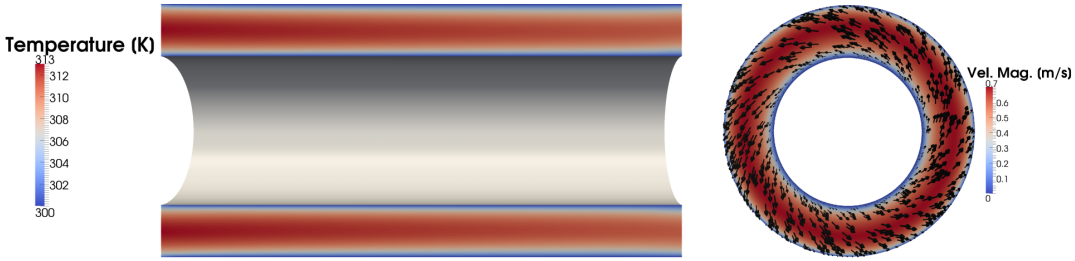

Figure 4.5: *Contours of temperature and velocity with vectors representation at inlet.*

would raise to 25% and the max error to 56%. It was then possible to state that the original Sieder-Tate coefficients tend to overestimate the Nusselt numbers obtained by the numerical simulations. However the average error was compatible with the experimental uncertainty and the highest errors coincided with the extreme cases (high Re or temperature difference), where CFD is less reliable.

After the validation, a full-factorial approach was adopted, for the simulations with the swirl effect, in order to obtain a complete set of design points uniformly distributed all over the design space. With this techniques a large number of simulations was carried out in a completely automatic way. Precisely, the total number of tests was the product of the variation levels of each parameter, resulting in $7 \times 7 \times 4 = 196$ total runs.

4.2.4 Nu-Correlation Based on Data Fitting

The DoE scheme based on full-factorial method took about two months to complete. During the operation, the monitored quantities were automatically post-processed and saved to specific files. Almost all the 196 runs converged to a solution, anyhow some simulations with high values of Reynolds number or high differences of temperature failed. Those design points were considered as outliers and were eliminated from the population to achieve a more reliable correlation.

In order to obtain the Nusselt correlation that fitted the numerical data in the best possible way, it was primarily necessary to choose its form, starting from the existing correlation presented in § 4.2.1. In this case, the Sudarev form with viscosity ratio was chosen, but with the exponent applied just to the tangent term:

$$\mathrm{Nu} = A \cdot \mathrm{Re}^B \cdot \mathrm{Pr}^C \cdot (\mu_{bulk}/\mu_s)^D \cdot [1 + \tan^E(\bar{\vartheta})] \tag{4.15}$$

where A, B, C, D and E are the coefficients that had to be calibrated to fit the Nusselt number values obtained by the CFD simulations. It is important to note that the swirl angle $\bar{\vartheta}$ was computed as the average between inlet and outlet as obtained from the CFD results $\bar{\vartheta} = 0.5 \cdot (\vartheta_{in} + \vartheta_{out})$.

The Nusselt number is often plotted as a function of the Reynolds number, due to their strong dependence. Therefore it was useful to define a modified Nusselt number $\widetilde{\mathrm{Nu}}$, based on the Reynolds number alone, $\widetilde{\mathrm{Nu}} = f(\mathrm{Nu})$

$$\widetilde{\mathrm{Nu}} = \frac{\mathrm{Nu}}{\mathrm{Pr}^C \cdot (\mu_{bulk}/\mu_s)^D \cdot [1 + \tan^E(\bar{\vartheta})]} = A \cdot \mathrm{Re}^B \tag{4.16}$$

From every set of coefficients B, C, D and E, the value of A could be computed as

$$A = \frac{\mathrm{Nu}}{\mathrm{Re}^B \cdot \mathrm{Pr}^C \cdot (\mu_{bulk}/\mu_s)^D \cdot [1 + \tan^E(\bar{\vartheta})]} \tag{4.17}$$

It was then possible to define a vector $\mathbf{A}$ whose elements are the different values of A computed from the data deriving from the numerical simulations (Nu, Re, μ_{bulk}, μ_s and $\bar{\vartheta}$). The minimum A_{min} and the maximum A_{max} of this vector represent the coefficients of the line that encased the numerical design points. In Fig. 4.6 it is shown an example of modified Nusselt number $\widetilde{\mathrm{Nu}}$ plotted as a function of Re, the red dots represent the numerical design points, while the black dashed lines are the encasing functions related to the minimum and the maximum A coefficients. The inferior line is defined as $\widetilde{\mathrm{Nu}} = A_{min}\mathrm{Re}^B$, while the superior is $\widetilde{\mathrm{Nu}} = A_{max}\mathrm{Re}^B$.

The $\mathbf{A}$ coefficient to choose lies between A_{min} and A_{max} and could be computed

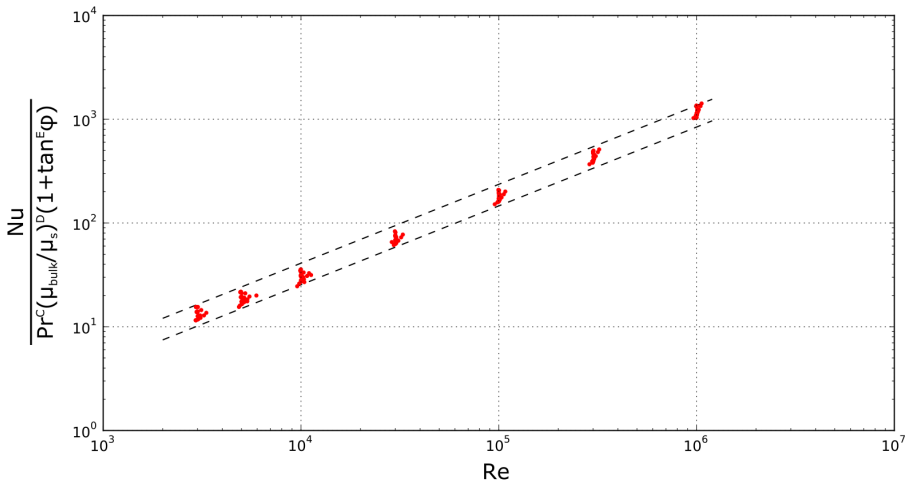

Figure 4.6: *Example of modified Nusselt number plotted as a function of Reynolds number, with superior and inferior lines that encase the numerical design points.*

knowing that

$$A_{min} = \frac{A}{(1 + err_{max})} \tag{4.18}$$

$$A_{max} = A \cdot (1 + err_{max}) \tag{4.19}$$

where err_{max} is the highest relative error. From Eq. (4.18) and (4.19) comes

$$(1 + err_{max}) = \sqrt{A_{max}/A_{min}} \tag{4.20}$$

and the coefficient A can be calculated as

$$A = A_{min}(1 + err_{max}) = A_{max}/(1 + err_{max}) \tag{4.21}$$

In order to find the best Nusselt correlation, a Python script was developed which was intended to minimize the gap between A_{max} and A_{min} (the same goes for their ratio, which is related to the maximum relative error), varying the coefficients B, C, D and E within specific ranges defined by the user. All possible coefficients combinations were tested in a full-factorial scheme and the minimum error sets were reported.

In this case only air was considered in the simulations, therefore the exponent C

Table 4.2: *Best set of coefficients.*

B	C	D	E
0.769	1/3	0.208	1.495

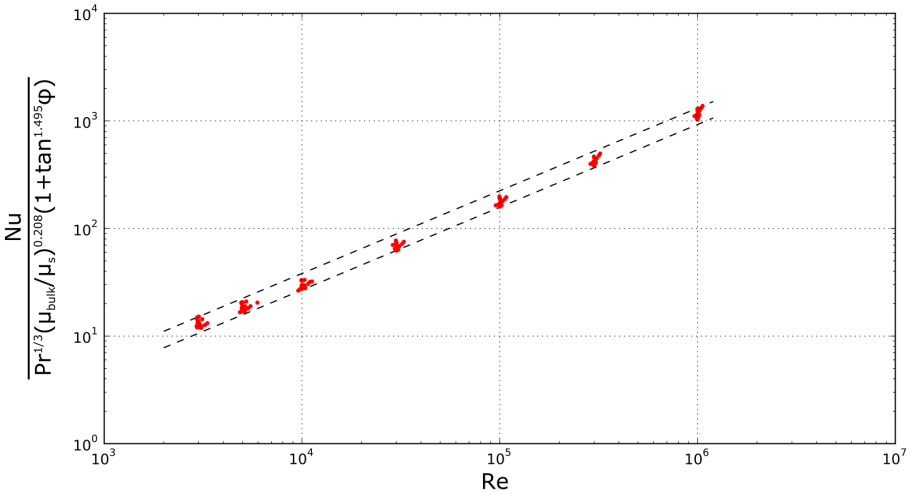

Figure 4.7: *Graphical representation of Nusselt correlation found.*

of the Prandtl number in the correlation tests was taken as a constant equal to 1/3, as in Sieder-Tate formulation.

The best set of coefficients which, according to the Python script, interpolated the numerical data with a maximum error of 19.3% and a root mean square error of 9.8%, is shown in Tab. 4.2.

The inferior and superior encasing lines, then, took the following form

$$\widetilde{\mathrm{Nu}} = 0.0225 \cdot \mathrm{Re}^{0.769} \tag{4.22}$$

$$\widetilde{\mathrm{Nu}} = 0.0321 \cdot \mathrm{Re}^{0.769} \tag{4.23}$$

A graphical representation of the design points and the encasing lines is given in Fig. 4.7. The gap between the lines was reduced as well as the highest error.

With Eq. (4.21) it was possible to obtain the average value for the A coefficient

and the final correlation for the Nusselt number in presence of swirl in annular ducts:

$$\mathrm{Nu} = 0.0269 \cdot \mathrm{Re}^{0.769} \cdot \mathrm{Pr}^{1/3} \cdot (\mu_{bulk}/\mu_s)^{0.208} \cdot [1 + \tan^{1.495}(\bar{\vartheta})] \tag{4.24}$$

4.2.5 Remarks

With this preliminary study the influence of the swirl component on the heat transfer was evaluated. In particular, a series of numerical simulations of an annular duct was carried out varying the Reynolds number, the temperature difference and, obviously, the swirl angle of the inlet flux. Finally a new correlation for the Nusselt number was proposed with a specific term to take into account the influence of the swirl. The suggested correlation was calibrated to minimize the highest and the root mean square error, compared with numerical data.

An esteem of the swirl influence could be done with the proposed correlation. In particular, a simplified model was developed on a spreadsheet with the new equation implemented for the Nusselt number calculation. This model computes the outlet temperature of an annular duct, when the wall temperature, the inlet temperature and the Reynolds number of the flow are given. Also the exchanged power $\dot{Q}$, the mean Nusselt number Nu and the heat transfer coefficient (HTC) h are calculated.

By varying the inlet swirl angle, with this simplified model it was possible to obtain the estimated trend of the heat transfer coefficient which was directly related to the thermal power exchanged. The results are shown in Fig. 4.8 and they have been obtained with an imposed temperature difference of 400 K between fluid and walls, and an L/D_h ratio of 5. The great influence of the Reynolds number is clearly highlighted by these results. Furthermore it can be stated that, for a given Reynolds number, the influence of the swirl angle has the trend of the function $[1 + \tan^E(\bar{\vartheta})]$. This additional term essentially takes into account the effects of the swirl component and can be seen as a correction to the Reynolds number, which is computed starting from the mass flow rate and, hence, from just the axial component of velocity.

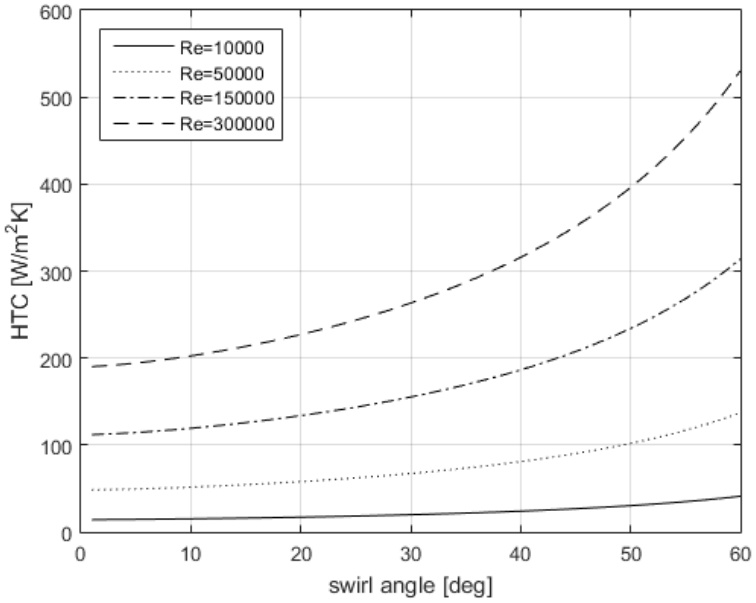

Figure 4.8: *Trend of the heat transfer coefficient varying the inlet swirl angle and the Reynolds number in the simplified model.*

4.3 Optimization of Longitudinal Fins for a Tube-in-tube Heat Exchanger

In the previous section the device responsible for the swirl motion of the secondary air has been investigated more in detail. In this section a dedicated study is presented regarding the second characteristic component of the recuperative burner: the longitudinal fins heat exchanger.

A three-dimensional numerical model of the heat exchanger has been developed, although many simplifications has been made from both a geometrical and a physical point of view. These simplifications have led to fast simulations that have been introduced in an optimization loop in order to maximize the heat transfer varying some geometrical parameters.

With this study the influence of the longitudinal fins on the performance of the system has been assessed and, at the same time, the CFD simulation has been fully

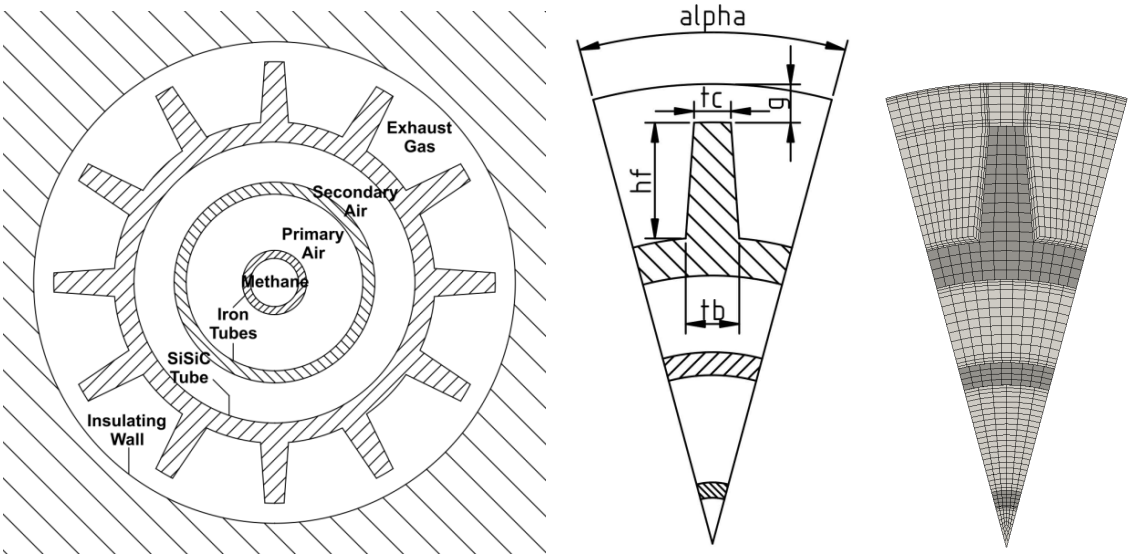

(a) *Section of the heat exchanger* (b) *Section of the domain* (c) *Section mesh*

Figure 4.9: *Heat exchanger geometry, computational domain, and mesh.*

integrated in a direct optimization process.

4.3.1 Numerical Model

The heat exchanger section of the analysed recuperative burner is made of the series of concentric tubes as shown in Fig. 4.9(a). Going from in to out, there are two inner iron tubes, the third is made of SiSiC, while the outer limit of the domain is made of a thick wall of refractory insulating material. As mentioned in § 4.1, the natural gas flows in the inner pipe, while the combustion air is split between two more passages (primary and secondary air). Exhaust gas flows counter-currently through the outer passage. The structure of this system allows for a suitable pre-heating of the secondary air, while primary air and methane will remain relatively cold.

The buoyancy effects have been neglected, because the flux is characterized by a strong forced convection, in this way it was possible to exploit the symmetry of the problem and just a portion of the domain, with one fin, was taken into account and meshed (Fig. 4.9(b) and 4.9(c)). The entire model has been developed using Open-

Table 4.3: *Boundary conditions.*

Flux	Mass Flow Rate [g/s] (12.5 kW case)	Inlet Temperature [°C]
Methane	0.251	26.5
Primary air	1.486	26.5
Secondary air	3.468	26.5
Exhaust	5.205	1300.0

FOAM. The mesh was realized by the utility *blockMesh*, and was fully-hexahedral and non-conformal at the fluid/solid interfaces. With specific scripts the grid was automatically generated varying some input geometrical parameters and contained between 60 and 150 thousand elements depending on the configuration. Furthermore, with the same dedicated scripts, the OpenFOAM case could be automatically handled in terms of pre-processing (boundary conditions and thermo-physical models) and post-processing.

In Tab. 4.3 the mass flow rates and temperatures boundary conditions are shown for each zone. The amount of natural gas is chosen so that the expected thermal power developed in the burner is equal to 12.5 or 25.0 kW , which are the configurations analysed in this preliminary study. The total mass flow rate of air is such that the combustion in the burner will occur with an air-fuel equivalence ratio $\lambda = 1.20$. The air is split in primary (30%) and secondary passage (70%) and no swirl motion is impressed to the fluxes. The inlet temperature of methane and combustion air is 26.5°C, while the exhaust gases enter the domain at 1300°C, assuming the complete combustion of the methane and the thermal losses into the kiln room. The mass flow rate of the exhaust equals the sum of methane and combustion air.

Since the different fluxes are completely separated and the only object of this study were the heat transfer capabilities, the simulations have included neither species nor combustion modelling. On the other hand, the turbulence was taken

into account with the k-ω-SST model using a low-Re model ($y^+ < 1$ always attained at the exchanger walls), while a P1 model was adopted for radiation effects. All the gas phases that come at play were treated as perfect gas; their thermophysical properties can vary with temperature following Sutherland [26] for the dynamic viscosity and using JANAF coefficients for the specific heat and enthalpy.

The external wall was considered adiabatic with an internal emissivity of 0.8, while ambient pressure conditions held at various outlets. Cyclic boundary conditions were assigned at the extremal patches of the wedge, allowing to model just a portion of the entire domain.

Obviously, the inlet mass flow rates of Tab. 4.3 have been divided by the number of fins, since just a portion of the domain was modelled. The esteemed Reynolds number never exceeded the fully turbulent limit, remaining in the laminar or transitional zone (≈ 3000). For the exhaust, due to the high temperatures and the larger sections, the Reynolds number turned out to be even lower, around 1000. However the choice of the hydraulic diameter ($D_h = 4A/P$, where A is the cross section area and P the perimeter) as reference for the Reynolds number in such an irregular geometry, is as classical as questionable. For this reason it was very difficult to state that the exhaust gas flux was fully laminar.

Finally, the solid materials considered in the simulations were: Fe360 with constant properties for the internal iron tubes and SiSiC for the heat exchanger, with the thermal conductivity and the specific heat varying with temperature (Tab. 4.4) according to the producer specification sheet.

The solver used in OpenFOAM was *buoyantSimpleFoam*, which is designed for stationary compressible cases and solves the pressure-velocity coupling with the SIMPLE segregated approach. One simulation required on average 20 minutes to reach convergence running in parallel on a 4 CPUs machine.

Table 4.4: *Solid materials properties definition.*

Material	Density [kg/m^3]	Thermal conductivity [W/(mK)]	Specific heat [J/(kgK)]	Emissivity
Fe360	7850	54	470	0.38
SiSiC	3120	$206.14 - 0.1236 \cdot T$	$459.69 - 0.4706 \cdot T$	0.90

Table 4.5: *Variables of the optimization and their ranges.*

Variable & symbol		Range		FF levels
Fins number	n_f	10	20	5
Fins height	h_f	5.0 mm	20.0 mm	4
Gap between fin crest and insul. wall	g	2.0 mm	10.0 mm	3.
Fins thickness at the base	t_b	6.0 mm	9.0 mm	3
Fins thickness ratio	r_f	0.5	0.99	3
Heat exchanger length	l_e		700.0 mm	N./A.

4.3.2 Optimization Process

For the optimization of the heat exchanger a design space has been considered, which is composed of 6 variables related to the geometry of the exhaust gas passage, and in particular of the fins located on the external surface of the SiSiC tube. The variables are resumed in Tab. 4.5 together with their range of variability.

The number of fins, despite being an integer variable, was allowed to vary with continuity for the purpose of the optimization. Following the notation in Fig. 4.9, the domain angular width was derived from the fins number as $\alpha = 2\pi/n_f$. The fins crest thickness was defined in terms of ratio over the base thickness, $t_c = r_f \cdot t_b$, with $r_f < 1$ in order to grant a shape which was easier to manufacture by fusion.

The aim of the optimization was the maximization of the heat transfer through the exchanger surface, subject to the respect of a performance, a compactness, and a cost constraint, namely:

- **Pressure drop**: of the exhaust gas across the exchanger had to be limited

below 3 mmH_2O (that is, 29.42 Pa). This is due to the fact that a positive relative pressure is maintained inside the kiln room, but it should be as small as possible in order to limit gas leakages through the kiln walls.

- **Length**: the heat exchanger length should have a value below 700 mm, simply for compactness reasons.

- **Volume**: the SiSiC duct value should be limited below 1406.1 cm^3.

In fact, according to the producer, one of the major costs in the burner realization is the silicon carbide material cost: the given volume corresponds to that of the current configuration.

The first constraint will tend to discard the solutions having a low section area for the exhaust gas passage. The latter will force the optimization process in finding the optimum material distribution according to the given parameterization of the problem.

The volume of the finned tube could be computed analytically once its geometry was defined. From simple algebraic considerations, in fact, an approximation of the finned tube volume is given by the sum of the volume of the annulus and of the fins

$$V_e \approx \left[\left(D_o^2 - D_i^2 \right) \frac{\pi}{4} + n_f h_f t_b \frac{1 + r_f}{2} \right] l_e, \tag{4.25}$$

while a more rigorous formulation, considering also the curvature of the fins base and crest, results in

$$\begin{aligned} V_e = & \left[\left(D_o^2 - D_i^2 \right) \frac{\pi}{4} + n_f h_f t_b \frac{1 + r_f}{2} - \frac{n_f D_o^2}{8} \left(\alpha_b - \sin \alpha_b \right) + \right. \\ & \left. + \frac{n_f \left(D_o + 2h_f \right)^2}{8} \left(\alpha_c - \sin \alpha_c \right) \right] l_e \end{aligned} \tag{4.26}$$

where

$$\alpha_b = 2 \arcsin \left(\frac{t_b}{D_o} \right) \quad , \quad \alpha_c = 2 \arcsin \left(\frac{t_b r_f}{D_o + 2h_f} \right), \tag{4.27}$$

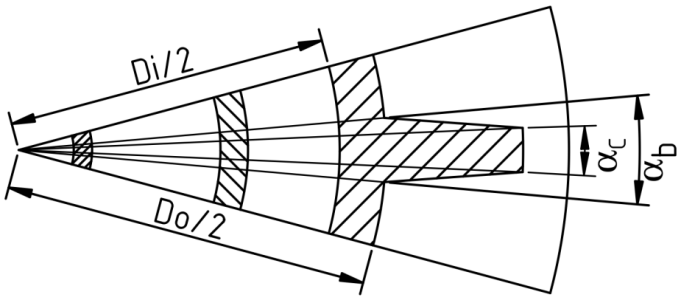

Figure 4.10: *Geometrical meaning of the symbols introduced in Eq. (4.26).*

and the symbols introduced are graphically explained in Fig. 4.10.

By solving Eq. (4.26) in l_e, for any configuration it was possible to set the proper heat exchanger length that meets the volume constraint, yet limiting its maximum value according to Tab. 4.5. This could be done since it is straightforward that the optimum exchanger configuration would necessarily use all the allowed heat exchanger pipe volume to maximize the heat transfer. Such a consideration made it possible to reduce the number of variables by one, also removing the volume and the length constraints. In this way the optimization problem was reduced to 5 variables, 1 constraint and 1 objective function.

From the algorithmic point of view, the Nelder & Mead simplex method (§ 3.3.1) was used for the optimization. The efficiency and the stability of this method in handling unconstrained optimization problems is very well known. However, when dealing with constraints the method can fail in finding a proper optimum also for very simple problems. Similar limitations are found in other *deterministic* optimization algorithms as well, and must be indirectly ascribed to the *local* nature of the algorithm.

In order to prevent misconvergence and obtain a more general insight over the design space, the optimization was preceded by a full-factorial design of experiments (FF-DoE). The optimization process was then repeated a few times, either starting from a random simplex in the design space, or from a simplex localized around the

most performing areas of the design space according to the FF analysis. The FF levels chosen for the variables are summarized in Tab. 4.5, they were equally spaced within the ranges, and resulted in a 540 samples DoE overall.

It was expected that the 25 kW operating condition would be subject to more severe misconvergence problems due to the difficulties in respecting the pressure constraint. Compared to the 12.5 kW case in fact, the mass flow rates were double and the pressure drop was expected to be up to four times higher for a given geometry configuration. This will probably lead to rather different optimum configurations overall.

4.3.3 Results

For both the 12.5 and the 25.0 kW operating conditions, several optimization processes have been carried out with different conditions. Three runs of the Nelder & Mead algorithm were performed with the initial simplex randomly initialized accordingly to the design space limits summarized in Tab. 4.5. This first set of optimizations will be named *scratch start*. Then, starting from the experience gained through the full-factorial analysis and the first set of optimizations, a restricted design space was chosen, centred around the best configuration previously found. Three new runs have been performed, which will be named *guided start*. In the final step, the best configuration was adjusted in order to get an integer value for the fins number. The fins height was then modified to respect the volume constraint, while the gap was adapted to respect the pressure constraint.

- **12.5 kW**: the current configuration gave a results of 1593.2 W in terms of heat transfer, with a pressure drop of 12.07 Pa. The FF-DoE analysis returned 349 feasible designs out of 540 total simulations performed (64.6 %). By feasible design, a configurations respecting the pressure drop constraint is intended. The results of the optimization runs are reported in Tab. 4.6. In

Table 4.6: *Optimum configurations found at each step of the optimization process, 12.5 kW case.*

Step	Heat transfer [W]	Press. drop [Pa]	Gain	Optimum configuration						
				n_f	f_h [mm]	g [mm]	t_b [mm]	r_f	l_e [mm]	V_e [cm^3]
Current	1593.2	12.07								
FF-DOE	1742.5	26.78	9.4 %	17.5	10.0	6.0	6.0	0.50	700.0	1370.9
Scratch start	1748.1	28.42	9.7 %	15.9	10.5	5.2	6.7	0.51	700.0	1405.2
Guided start	1767.9	27.65	11.0 %	16.5	11.2	4.8	6.0	0.50	700.0	1402.5
Optimum	1765.9	29.09	10.8 %	17	11.0	4.9	6.0	0.50	698.6	1406.1

the guided start optimization, the ranges of the variables were set as follows: $n_f \in [14.5, 18.0]$, $h_f \in [8.0\,\text{mm}, 13.0\,\text{mm}]$, $g \in [4.0\,\text{mm}, 6.5\,\text{mm}]$. t_b and r_f were fixed at 6.0 mm and 0.5 respectively since from the previous simulations it was evident that thinner fins were leading to a better overall exploitation of the material in view of heat transfer enhancement. In the last row of Tab. 4.6 the results with an integer value for the fins number is reported. Compared to the current configuration, the optimum heat exchanger is able to attain a 10.8 % heat transfer enhancement yet respecting the pressure and the volume constraints.

- **25.0 kW**: a heat transfer of 2155.9 W resulted from the current configuration, along with a pressure drop of 30.03 Pa, which lightly exceeded the given constraint. The FF-DoE analysis returned 179 feasible designs out of 540 total simulations (33.1 %). As expected, due to the larger mass flow rates at play, in this case it was not easy to respect the pressure constraint, and the number of feasible design points fell down. The results of the optimization process are shown in Tab. 4.7 similarly to the 12.5 kW case. In the guided start optimization, for this case, the ranges of the variables were set as follows: $n_f \in [11.0, 14.5]$, $h_f \in [13.0\,\text{mm}, 18.0\,\text{mm}]$, $g \in [4.0\,\text{mm}, 6.5\,\text{mm}]$. t_b and r_f were fixed at 6.0 mm and 0.5 respectively. Compared to the current config-

Table 4.7: *Optimum configurations found at each step of the optimization process, 25.0 kW case.*

Step	Heat transfer [W]	Press. drop [Pa]	Gain	Optimum configuration						
				n_f	f_h [mm]	g [mm]	t_b [mm]	r_f	l_e [mm]	V_e [cm^3]
Current	2155.9	30.03								
FF-DOE	2270.9	25.03	5.3 %	12.5	15.0	6.0	6.0	0.50	697.2	1406.1
Scratch start	2264.9	29.30	5.1 %	11.1	15.1	4.5	6.3	0.56	700.0	1401.3
Guided start	2296.9	29.15	6.5 %	12.6	14.7	5.3	6.0	0.50	700.0	1406.0
Optimum	2291.9	29.07	6.3 %	13	14.3	5.8	6.0	0.50	699.8	1406.1

uration, the optimum heat exchanger is able to attain a 6.3 % heat transfer enhancement yet respecting the pressure and the volume constraints.

4.3.4 Remarks

In Fig. 4.11 a comparison between the current fin shape and the optimum fin shapes found for the different operating conditions is shown. The two optimum configurations are quite different, mainly due to the pressure constraint. For the 12.5 kW case, in fact, the constraint is less critical, allowing the exhaust gas duct section area to be smaller, and, as a consequence, the fins to be shorter and more numerous. The compactness of the duct section and the larger wetted area positively affect the heat exchanger efficiency as will be shown in the following. On the contrary, for the 25 kW case, a larger exhaust gas duct section area is needed, and the fins must be longer to prevent the chance that a portion of the exhaust gases would pass through the heat exchanger keeping far from the exchanger wetted surface.

In terms of energy efficiency, this suggests that an industrial roller kiln with recuperative burners, should preferably be equipped with different kind of burners. In fact, even though the burners mainly work under steady state operating conditions, these conditions are different for each location of the kiln depending on a series of factor: first of all whether in a given area the product must be warmed up quickly

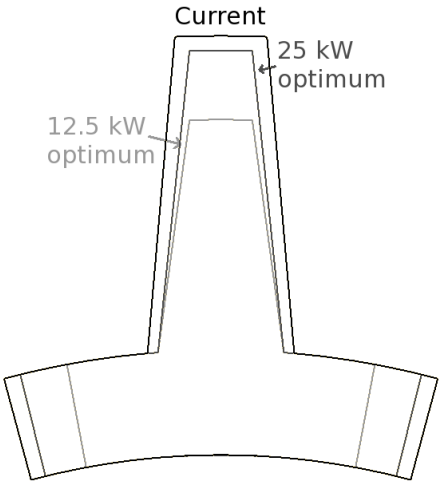

Figure 4.11: *Current versus optimum fin shapes.*

Table 4.8: *Current versus optimum configurations in terms of bulk temperature differences between the inlet and the outlet sections, heat exchanger efficiency, and heat transfer distribution between primary and secondary air.*

		Current		Optimum	
		12.5 kW	25 kW	12.5 kW	25 kW
Exhaust gas ΔT_b	[°C]	−222.0	−149.3	−241.2	−157.9
Secondary Air ΔT_b	[°C]	+421.3	+290.2	+463.5	+307.8
Primary Air ΔT_b	[°C]	+21.0	+6.8	+28.8	+9.1
Exchanger Efficiency	[%]	19.1	12.9	21.1	13.7
Primary Air Heat Fraction	[%]	2.01	0.95	2.48	1.21
Secondary Air Heat Fraction	[%]	97.99	99.05	97.52	98.79

(high thermal power at the burners needed) or be kept at a certain temperature (low thermal power at the burners needed).

Table 4.8 analyses the current and the optimum configurations in terms of temperature jump of the various flow streams across the exchanger, heat exchanger efficiency, and the distribution of the total heat transferred between the primary and the secondary air. The gas stream is not reported as it undergoes a negligible temperature jump compared to the other fluids. The heat exchanger efficiency is computed as the ratio between the heat transfer rate and the sensible enthalpy of

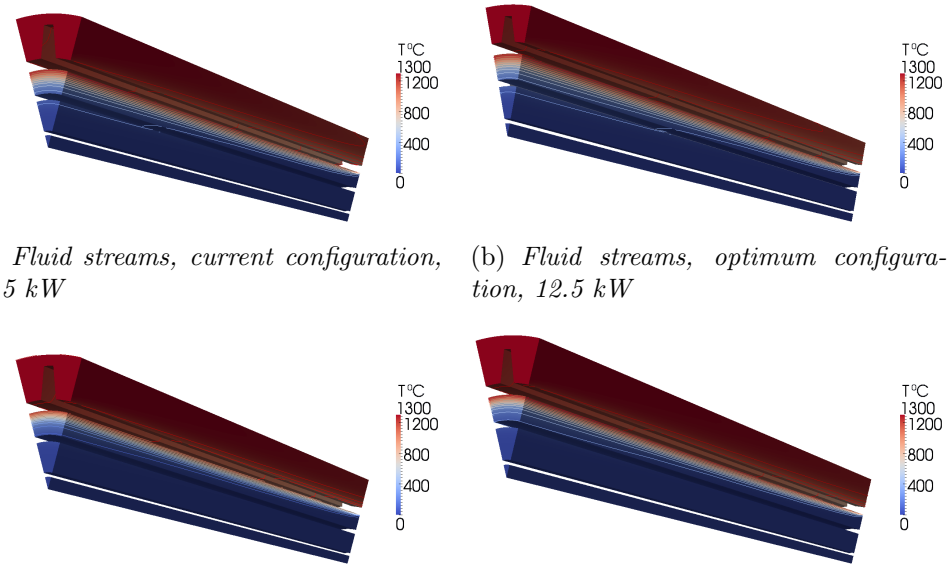

(a) *Fluid streams, current configuration, 12.5 kW*

(b) *Fluid streams, optimum configuration, 12.5 kW*

(c) *Fluid streams, current configuration, 25.0 kW*

(d) *Fluid streams, optimum configuration, 25.0 kW*

Figure 4.12: *Temperature distributions along the heat exchanger; the contour lines in the images are traced every 100 °C.*

the exhaust gas entering the heat exchanger.

It is shown how the optimum burner configurations are more efficient and they are able to induce a stronger warm up of both primary and secondary air. Yet, the primary air warm up is still moderate, and this is a positive aspect in view of limiting the burner NO_x production rate. The same warm up effect can be seen from Fig. 4.12 where the effects of the different burner configurations on the temperature distribution along the heat exchanger is shown. From the figure it is also evident the large radial temperature gradient in the secondary air region.

4.4 CFD Model of the Complete Burner

With the simplified models presented in § 4.2 and § 4.3 the distinctive features of the recuperative burner discussed in this thesis, have been deeply investigated. The information obtained from those analysis could be exploited to improve the performances of the recuperative burner in terms of recovered thermal power from exhaust gases. However, to investigate this kind of machines, the most complete and reliable solution is the simulation of the entire system, with all the features represented together with complex physical mechanisms (such as the combustion process).

For this reason a complete model of the recuperative burner has been developed and it is described in the next paragraphs. It has to be noted that some of the physical phenomena that has to be simulated are not yet implemented in OpenFOAM and thus the model has to be realized with the commercial packages provided by the ANSYS software suite. Therefore a computational infrastructure has been developed, which is able to handle the definition of the geometry, the meshing operations and the post-processing in a fully automatic way.

4.4.1 Geometry and Mesh

The numerical model has been validated with an experimental campaign (details in § 4.5) before being exploited for the optimization of the performance. For this reason, the boundary conditions and especially the computational domain had to be consistent with the experimental facility.

In Fig. 4.13 the domain modelled is shown, downstream of the burner body, instead of the kiln environment, there is a test chamber like the one used in the experiments. The effects of the surrounding walls are included in the simulation with specific boundary conditions (see § 4.4.3), but are not considered in their entirety in order to save some cells and, thus, computational time. The only solid zones which have been discretized and simulated are the ones where the heat transfer

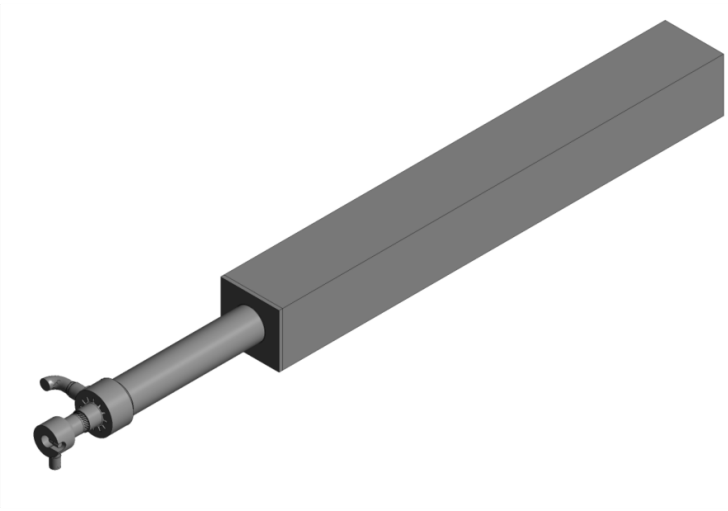

Figure 4.13: *Computational domain of the complete burner model.*

phenomenon is relevant, that is the methane tube, the tube between primary and secondary air with the burner's head and, obviously, the finned heat exchanger.

For what concerns the meshing process, a good compromise had to be made between two different meshing principles: a high quality, fully hexahedral mesh, very reliable but difficult to realize; and a mesh composed of tetrahedral elements (then collapsed into polyhedral elements) with boundary layers at walls. The advantage of the latter solution relies in the robustness of the meshing algorithm, which is one fundamental requirement in an automatic calculation infrastructure. In the computational grid adopted, the volumes that could be easily identified as bodies obtained from extrusion, such as the tubes or the rectangular test chamber, have been meshed with hexahedral elements; while, for the remaining irregular volumes, an automatic tetrahedral method has been selected with appropriate grid refinements where required by the geometry or the physics of the problem.

This criterion can be seen in Fig. 4.14, where the methane and air tubes are meshed with hexahedral cells as well as a large portion of the finned heat exchanger

(Fig. 4.14(a)). The burner's head represents a very complex zone of the domain and has been filled with tetrahedral elements (then converted to polyhedral); while the shape of the test chamber allowed for a more ordered grid (Fig. 4.14(b)). All the walls have been covered with boundary layers (Fig. 4.14(c)) properly sized to obtain a low-Re model, with an expected $y^+ < 5$. Although a correct low-Re model should adopt grid with values of y^+ below one, in these cases higher values have been accepted in order to keep the number of cells low, thus saving computational time. Furthermore, the *Enhanced Wall Treatment* implemented in Fluent combines the low-Re and the high-Re approach, reducing the error committed with intermediate meshes where the first near-wall node is placed neither in the fully turbulent region, nor in the direct vicinity of the wall [14].

The defined hybrid meshing process (hexahedral/tetrahedral) turned out to be very robust, with just few failures in all the generated models. The size of the grids was around 5 million cells before the polyhedrization process and after that it decreased to 3 million.

4.4.2 Physical and Mathematical Models

Industrial kilns are typically fueled with the gas that comes from the national network. The composition of this gas does not comprehend only methane, but it is a mixture of various elements, often unknown. The only information about the national gas that can be considered reliable is its Lower Heating Value (LHV), which, in the examined case, was assumed to be equal to 47.44 MJ/kg. With a dedicated script, many gas compositions have been tested in order to find the set of elements, which showed the better matching with the target value of LHV.

Usually in the common national gas it is possible to find, in descending order, methane, ethane, propane, butane and other hydrocarbons. In the simplified model developed, only the first two species have been considered in order to limit the number of differential equations (one for each species) that Fluent had to solve. In this

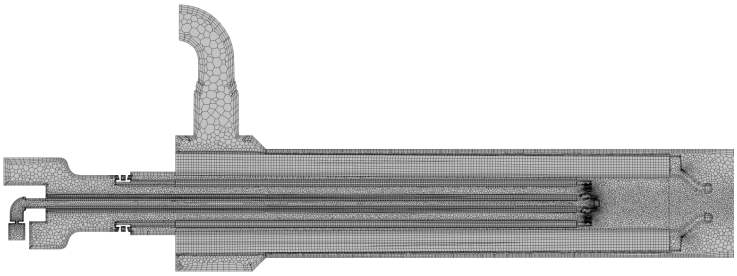

(a) *Mesh of the burner's body.*

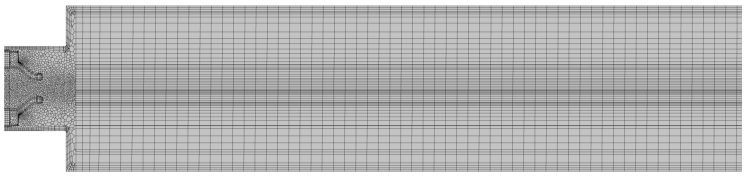

(b) *Mesh of the test chamber.*

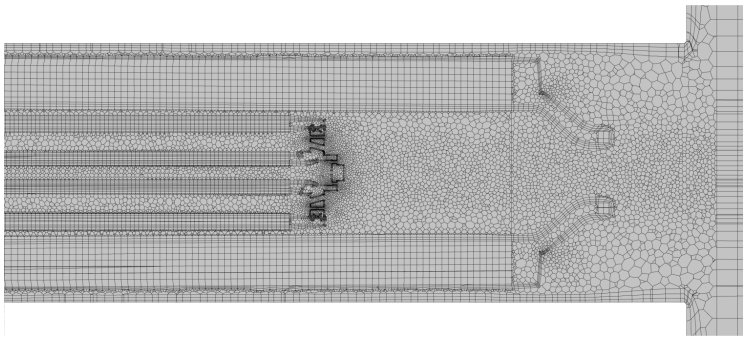

(c) *Particular of the mesh of the burner's head.*

Figure 4.14: *Computational grid of the complete burner model.*

way global reaction mechanisms were considered and some intermediate species have been completely neglected, some of which are important for the analysis of pollutant agent, in particular the carbon monoxide and the nitrogen oxides. However, this study is focused on the assessment of the performance of the burner in terms of recovered thermal power from exhaust gases and, thus, the problems related to minor pollutant agents could be neglected, in favour of a general reduction of computational time. The gas composition found is shown in Tab. 4.9, and gives the

Table 4.9: *Composition of national gas and ambient air in volume and mass fraction.*

Component	Air		Gas	
	Volume	Mass	Volume	Mass
CH_4	– %	– %	88.00 %	79.90 %
C_4H_6	– %	– %	9.20 %	15.66 %
O_2	21.02 %	23.36 %	– %	– %
H_2O	0.61 %	0.38 %	– %	– %
N_2	78.37 %	76.26 %	2.80 %	4.44 %

following thermo-physical properties:

- Thermo-dynamic mixture constant: $R_{mix} = 470.59$ J/(kg·K)
- Mean molar mass: $M_{m,mix} = 17.76$ kg/kmol
- Density: $\rho_{mix} = 0.788$ kg/Nm^3
- Stoichiometric air/fuel ratio: $(A/F)_{st} = 16.29$

where the density is computed in kg/Nm^3, which refers to the density at the reference temperature of 0°C, and the stoichiometric ratio is computed with respect to the ambient air composition reported in Tab. 4.9. The air composition has been observed with a dedicated instrument during the experimental campaign.

The *Finite Rate/Eddy Dissipation Model* presented in § 2.3.2 has been adopted for the simulations. The global oxidation reaction for methane and ethane have been activated

$$\begin{aligned} CH_4 + 2O_2 &\rightarrow CO_2 + 2H_2O \\ C_2H_6 + 3.5O_2 &\rightarrow 2CO_2 + 3H_2O \end{aligned} \tag{4.28}$$

with the default kinetic coefficients of Fluent's database for the Arrhenius rate calculation.

After the characterization of the fluid presented above, the focus was switched

on the solid materials. The company that produce the burner has provided a list of technical sheets relative to the utilized materials. They have been implemented in the solution software considering also the temperature dependence of the main properties, such as specific heat and thermal conductivity.

The radiation effects have been taken into account with the *Discrete Ordinate Model* presented in § 2.4.2. The angular space has been divided in 4×4 zones with a pixelation of 6×6, which ensure a reliable modelling of the radiation phenomena [14].

The k-ω SST model has been used for the closure of the turbulence problem. This model, explained in § 2.2.2, covers a wide range of cases due to its capability of blending between classic k-ω and k-ϵ models. The low-Re correction has been activated.

For the numerical solution, a stationary *pressure-based coupled* solver (§ 2.5.2) has been adopted with first order upwind scheme for the spatial discretization, in order to ensure the stability of the automatic process. A cold initialization was provided to the simulation, volumetric reactions and radiation modelling have been enabled after 1000 iterations from start. The solution took 10000 iterations to reach the full convergence, for a total computational time of about 24 hours per run, on a cluster equipped with 128 active cores.

4.4.3 Boundary Conditions

The mass flow rates boundary conditions have been set according to the behaviour of the experimental facility, thus there are two inlets, one for the gas and one for the combustion air, while the entire amount of exhaust gases are drawn by a single manifold and pass through the heat exchanger. This configuration does not reflect the real situation, where, depending on the pressure conditions inside the kiln room, the exhaust gases which are expelled through the heat exchanger can also reduce to 40-60% of the sum of the gas and air flow rates. However, definite values for the

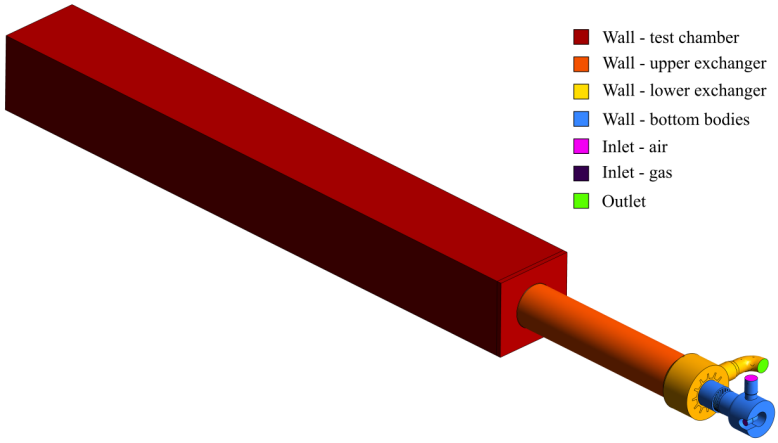

Figure 4.15: *Boundary patches of the complete model, coloured by the type of boundary condition applied to them.*

exhausts flow rates through the burners in the different zones of the kiln are not available, thus the $\dot{m}_{exhaust} = \dot{m}_{air} + \dot{m}_{gas}$ condition has been maintained also after the validation phase, for the optimization process.

As presented in § 4.3, the influence of mass flow rates on the optimum fin's geometry is not negligible; therefore, the solution found after the optimization, would not be the best for every burner in the kiln, because of the different conditions along the firing room that cause different suction percentages in the recuperative burners. Nevertheless an average increase in the performance is expected, with respect to the current configuration. In fact, the parameters considered in this complete model was not only related to the fin's geometry, but also to other elements, such as the combustion chamber or the swirl component, which are not directly dependent to the exhausts mass flow rates.

In Fig. 4.15 a schematic representation of the boundary patches of the domain is presented. Only the external patches are shown, while the internal ones, which act as interfaces between the solid and the fluid zone, have been set as *coupled* surfaces.

Table 4.10: *General boundary conditions scheme.*

	Inlets	Outlet	Walls
Mass Flow	*Fixed*	*Calculated*	*Adherence*
Pressure	*Calculated*	*Fixed*	*Adherence*
Energy	*Fixed Temp.*	*Calc. Temp.*	*Mixed*
Turbulence	*Fixed*	*Calculated*	*Wall Functions*
Species	*Fixed*	*Calculated*	*Zero Diffusive Flux*

A general scheme for the boundary conditions adopted is shown in Tab. 4.10. All the governing equations considered in the simulation are included in this scheme: the momentum and continuity equations for the pressure-velocity coupling problem, the energy equation, the turbulence closure problem and finally the chemical species transport equations.

For what concerns the mass balance, at the inlets a condition of fixed mass flow rate was imposed while the pressure is calculated accordingly by the solver. For the outlet, on the contrary, the mass flow rate is computed to respect the continuity principle, while a relative static pressure value was imposed. The mass flow rate values of combustion air and gas have been set in order to achieve the desired thermal power and air excess, as required by the producing company.

The temperatures at the inlet patches were fixed. The chemical reactions release a great amount of thermal power which is partially dispersed along the domain's walls, while the remaining portion is sucked through the outlet patch determining its temperature value. The walls in the exchanger upstream zone are considered adiabatic due to the low temperature of the fluid (the *Wall - bottom bodies* of Fig. 4.15). For the other walls, mixed boundary conditions have been implemented: the conductive thermal resistances for every patch are computed by the solver defining the layers with thickness and material; while the external convection heat transfer is calculated with user defined coefficient h_{ext} and temperature T_{ext}, as well as the

external emissivity ϵ_{ext} for the radiation dispersions. The solver iteratively solve the total wall heat flux $\dot{q}$ problem

$$\dot{q} = \lambda_f \frac{(T_f - T_{w,int})}{\Delta x} + \dot{q}_{rad,int} = \frac{(T_{w,int} - T_{w,ext})}{R_{wall}} = h_{ext}(T_{w,ext} - T_{ext}) + \dot{q}_{rad,ext} \quad (4.29)$$

where,

λ_f = thermal conductivity of the fluid

T_f = temperature of the fluid in the near-wall cells

$T_{w,int}$ = internal temperature of the wall

Δx = distance between wall and near-wall cells centroids

$\dot{q}_{rad,int}$ = internal radiative heat flux

$T_{w,ext}$ = external temperature of the wall

R_{wall} = conductive thermal resistance of the wall $(s_1/\lambda_1 + s_2/\lambda_2 + \ldots)$

h_{ext} = external HTC, defined by user

T_{ext} = external temperature of the fluid, defined by user

$q_{rad,ext}$ = external radiative heat flux $\epsilon_{ext}\sigma(T^4_{w,ext} - T^4_{ext})$

The wall compositions implemented in Fluent reflect the real compositions used in the experimental campaign, which will be presented in § 4.5.1. For the h_{ext} a mean value of 12 W/m^{2}K has been chosen, while the measured temperature of the surrounding ambient air was about 26.5°C. In Tab. 4.11 the surface emissivities used in the model are reported. In particular the emissivities of the surface that have a direct exposition to the flame were higher because they would be tarnished.

To complete the list of boundary conditions of Tab. 4.10, the turbulence quantities at the inlets have been calculated from the turbulence intensity and the hydraulic diameter of the duct, while the species mass fractions were set following the compositions reported in Tab. 4.9. For the outlet patch both turbulent quantities and species mass fractions are calculated by the solver solving the relative governing equations.

Table 4.11: *Surface emissivity values.*

Surface conditions	Emissivity
Iron	0.38
Iron (flame exposed)	0.61
SiSiC	0.83
SiSiC (flame exposed)	0.90
Brick (internal)	0.90
Brick (external)	0.75
Aluminium	0.05

4.5 Experimental Validation

Three of experimental campaigns were carried out at the burners manufacturing company in order to validate the numerical model. A single recuperative burner was tested in a small test chamber. The entire amount of exhaust gases was drawn through the heat exchanger and expelled to the atmosphere. Both the burner and the test chamber were equipped with measuring instruments to monitor the principal quantities of the system such as, mass flow rates, pressures and temperatures. Several preliminary tests were performed to achieve the adequate measurement's quality. With the experimental data obtained, the CFD model was calibrated and validated.

4.5.1 Experimental Facilities

The burner was mounted on a test stand and, downstream of it, a small chamber was built with internal dimensions of 1786 × 235 × 215 mm (Fig. 4.16). The chamber's walls were made of different layers, which were modelled as conductive resistances within the Fluent environment:

- **Ceiling wall**
  - refractory bricks (76 mm)

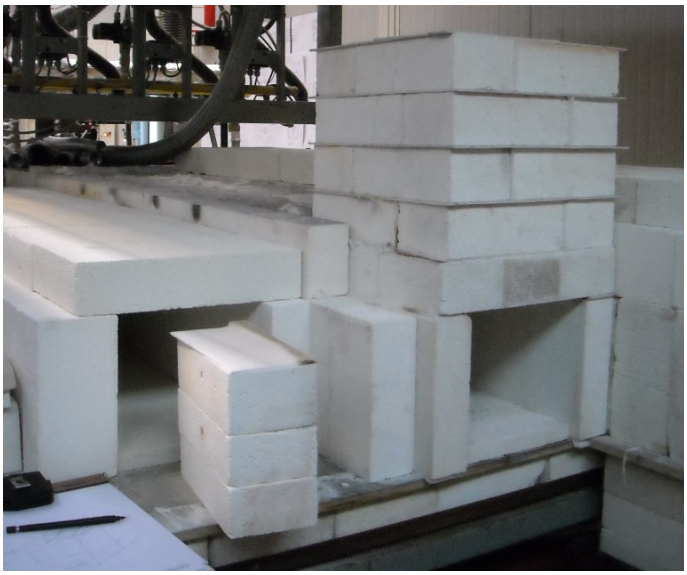

Figure 4.16: *The realization of the test chamber.*

  - insulating fibre (25 mm)

- **Floor wall**
  - refractory bricks (25 mm)
  - cordierite (12 mm)
  - refractory bricks (64 mm)
  - insulating refractory felt (15 mm)
  - iron sheet (2 mm)

- **Lateral walls**
  - refractory bricks (64 mm)
  - insulating fibre (3 mm)
  - refractory bricks (76 mm)

- **Near wall**: where the burner is located

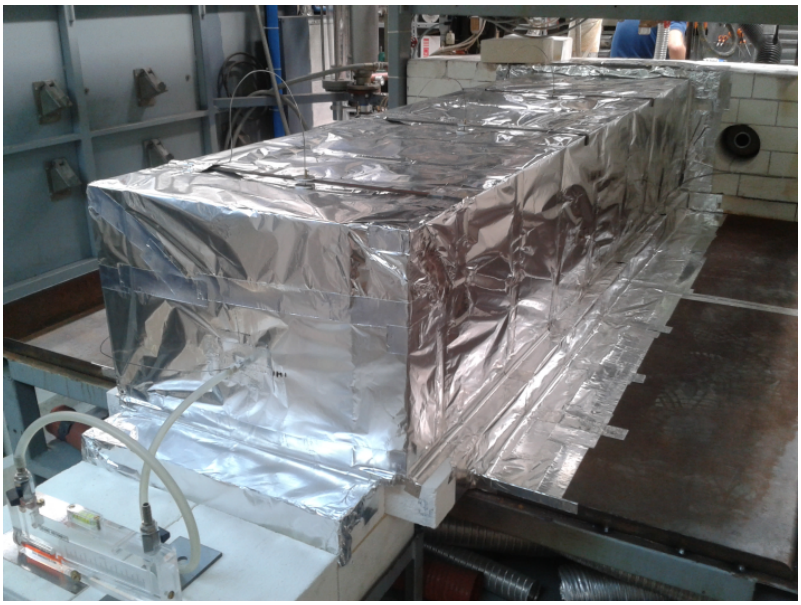

Figure 4.17: *Final test chamber configuration with the aluminium coat.*

  - refractory bricks (385 mm)
  - iron sheet (15 mm)

- **Far wall**
  - refractory bricks (115 mm)

The bricks were just leaned one on another without a coat of mortar to seal them together. Therefore a lot of air leakages were expected due to the high pressures and temperatures occurring in the test chamber. The presence of the leakages had to be avoided, or at least minimized, because it introduces uncertainties in the validation process, since in the CFD model the walls are assumed to be perfectly sealed. The entire chamber was wrapped with two thin sheets of aluminium in order to limit the losses through the walls, as shown in Fig. 4.17. A secondary effect of this addition was the reduction of the thermal losses due to radiation, which resulted in a better working environment around the test stand.

The entire amount of exhaust gases was extracted by a suction line located

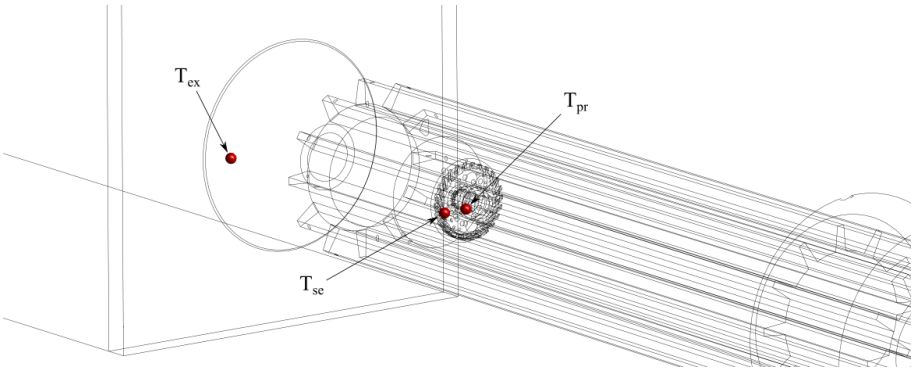

(a) *Thermocouples positions in the burner zone*

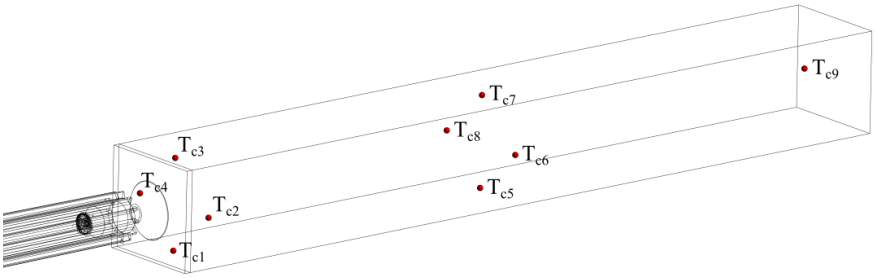

(b) *Thermocouples positions in the test chamber*

Figure 4.18: *Position of thermocouples in the experimental campaign.*

downstream of the heat exchanger. A fan controlled by an inverter made it possible to generate a negative pressure in the extraction duct, thus reducing the maximum pressure inside the test chamber. The test stand was equipped with a series of instruments that allowed to execute the following measurements:

- **Temperature measurement**: 13 thermocouples of K type, linked to a data-logger, have surveyed the temperature every 10 seconds for the whole duration of experimental campaign. The positions and the symbols for every thermocouple are summarized below and shown in Fig. 4.18.
  - T_{pr}: measured the temperature of the primary air and it was located near the burner's head.
  - T_{se}: measured the temperature of the secondary air and it was located

near the burner's head.

- T_{ex}: measured the temperature of the exhaust gases and it was located just before the finned heat exchanger zone.
- T_{out}: measured the temperature of the exhaust gases at the end of the heat exchanger, before the extraction duct
- T_{c1}: located in the portion of test chamber near the burner in proximity of the floor.
- T_{c2}: located in the portion of test chamber near the burner in proximity of the right wall.
- T_{c3}: located in the portion of test chamber near the burner in proximity of the ceiling.
- T_{c4}: located in the portion of test chamber near the burner in proximity of the left wall.
- T_{c5}: located in the middle length of test chamber in proximity of the floor.
- T_{c6}: located in the middle length of test chamber in proximity of the right wall.
- T_{c7}: located in the middle length of test chamber in proximity of the ceiling.
- T_{c8}: located in the middle length of test chamber in proximity of the left wall.
- T_{c9}: located in the bottom of test chamber.

- **Pressure measurement**: the static pressure was surveyed in 9 different locations and the data was saved continuously for the whole duration of the experiment in order to obtain average values for the post-processing. The position and the purpose of the measurements are reported below.

  - p_{a1} and p_{a2}: related to the orifice plate located in the combustion air feeding line. In order to calculate the flow rate, the upstream and downstream static pressures were needed. The conditions reported in ISO 5167 (which ensure the reliability of the measure taken with orifice plates) were not fully respected (in particular the minimum diameter of the duct) and for this reason the computed flow rate could be affected by error.
  - p_{g1} and p_{g2}: related to the orifice plate located in the natural gas feeding line. Also in this case, the conditions reported in ISO 5167 were not fully respected (in particular the minimum diameter of the duct, the minimum diameter of the orifice throat and the minimum Reynolds number).
  - p_{e1} and p_{e2}: related to the orifice plate located in the extraction duct. Also in this case, the conditions reported in ISO 5167 were not fully respected (in particular the minimum Reynolds number).
  - p_{bot}: measured the static pressure at the test chamber bottom.
  - p_{brn}: measured the static pressure in the test chamber near the burner's mouth where the minimum value of pressure was expected due to the high velocities at play.
  - p_{exh}: measured the static pressure at the end of the heat exchanger, before the exhaust gases flow in the duct for the definitive extraction.

- **Exhausts composition measurement**: the composition of the exhausts was constantly monitored with a flue gas analyser located in the extraction duct before the orifice plate. In particular the volume fraction of O_2 and CO_2 were collected.

- **Flow rate measurement**: a cone flow-meter was also positioned on each feeding line, upstream the orifices. This allowed a cross check of the measured values. Although not complying with some of the operating conditions listed

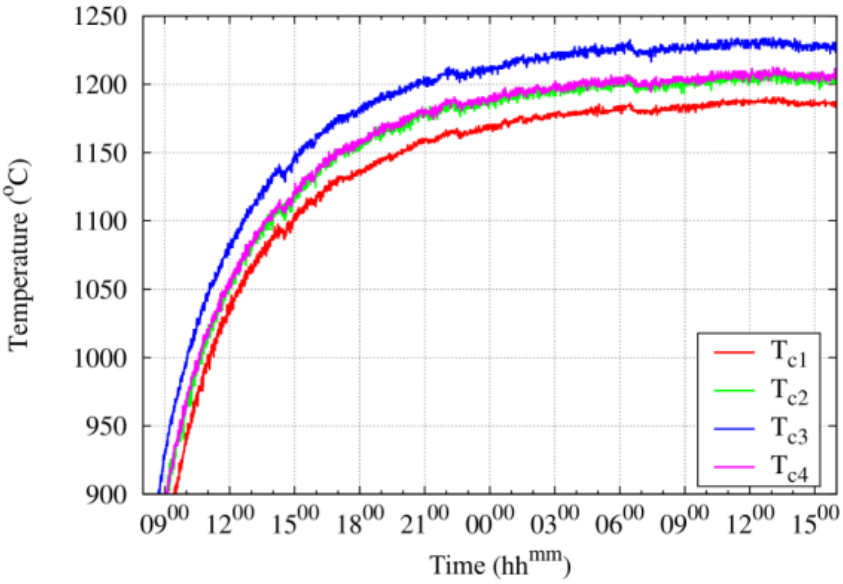

Figure 4.19: *Temperature trend in the pre-heating phase of experimental campaign.*

in ISO 5167, the orifice plates turned out to be more reliable than the cone flow-meter and were used in the validation process.

4.5.2 Measurements Campaigns

Three different measurement sessions were performed during the project. However, just the final session is reported in this thesis because the first two tries were judged to be affected by unacceptable uncertainties. Working on the critical issues emerged in the first sessions, the results of the final measurement campaign were considered acceptable. Three crucial aspects are reported below.

- **Thermal stability** of the system: the duration of the pre-heating phase in the first sessions was around 8 hours, which turned out not to be sufficient to achieve a reasonably stable steady-state condition. Therefore in the final measurement session the pre-heating phase was extended to 32 hours in order to achieve the full thermal stability (see Fig. 4.19).

- **Leakages** through the chamber's walls: in the first measurement session some

leakages were detected through the walls. In particular, in the zone of the chamber far from the burner, where the pressure was higher, flue gas was leaving out the test room; while near to the burner, where the static pressure was at its minimum, due to the high velocity of the flame jet, an unknown amount of ambient air was entering the test room. This was supposed after observing the thin aluminium sheet around the chamber, which was either pushed away from the walls or stitched to them. Since an additional uncontrolled cold mass flow rate would have a strong impact on the thermal balance, the pressure value inside the chamber was tuned in order to increase the global amount of leakages but ensuring that they were all flowing outwards. The speed of the fan located in the extraction duct was adjusted in order to maintain a positive relative pressure in both pressure takings p_{bot} and p_{brn}.

- **Flow rate** measurements: the last critical aspect of the experimental campaign was represented by uncertainties over the flow rate measurements. In fact, the cone flow-meters were not easy to read due to the fluctuations of the floating body and, moreover, the one mounted in the fuel feeding line was not calibrated for the natural gas composition. The orifice plates, which represent a more reliable measurement tool, were not mounted in compliance with the ISO 5167 and for this reason the computed flow rates are not free from errors.

In Fig. 4.19 it is possible to see the trend of the temperatures monitored in the test chamber by 4 thermocouples. The system took about 24 hours to reach an acceptable thermal stability. Measurements were started after 32 hours. The measured quantities are reported in Tab. 4.12 and 4.13.

4.5.3 Numerical Comparison and Remarks

The measurements taken during the experimental campaign were used to set up a comparative numerical simulation with the model described in § 4.4. In particular

Table 4.12: *Experimental results of temperature and pressure.*

Pressure	Air upstream orifice plate (p_{a1})	254.1	mmH_2O	2491	Pa
	Air downstream orifice plate (p_{a2})	206.0	mmH_2O	2020	Pa
	Gas upstream orifice plate (p_{g1})	119.1	mmH_2O	1168	Pa
	Gas downstream orifice plate (p_{g2})	105.8	mmH_2O	1037	Pa
	Exhaust upstream orifice plate (p_{e1})	-5.27	mmH_2O	-51.7	Pa
	Exhaust downstream orifice plate (p_{e2})	-9.77	mmH_2O	-95.8	Pa
	Test chamber bottom (p_{bot})	1.45	mmH_2O	14.2	Pa
	Test chamber near burner (p_{brn})	0.42	mmH_2O	4.1	Pa
	Downstream of heat exchanger (p_{exh})	-7.50	mmH_2O	-73.6	Pa
Temperature	Air at orifice plate	26.5	°C		
	Gas at orifice plate	24.0	°C		
	Exhaust at orifice plate	563.0	°C		
	Heat exchanger upstream T_{ex}	1170.4	°C		
	Heat exchanger downstream T_{out}	750.9	°C		
	Primary air near burner's head T_{pr}	370.6	°C		
	Secondary air near burner's head T_{se}	849.0	°C		
	Thermocouple T_{c1}	1185.9	°C		
	Thermocouple T_{c2}	1203.6	°C		
	Thermocouple T_{c3}	1227.8	°C		
	Thermocouple T_{c4}	1206.0	°C		
	Thermocouple T_{c5}	1041.0	°C		
	Thermocouple T_{c6}	1042.7	°C		
	Thermocouple T_{c7}	1042.1	°C		
	Thermocouple T_{c8}	1046.1	°C		
	Thermocouple T_{c9}	962.5	°C		

the mass flow rates and the temperatures of Tab. 4.12 were exploited. Also the expected compositions for ambient air and natural gas were implemented together with the right sequence of walls layers. The leakages were neglected and thus a general increase of temperatures was expected.

The simulation took 10000 iterations to reach an acceptable level of convergence in about 24 hours. With specific probes, the numerical temperatures have been captured in the same positions occupied by the thermocouples in the experimental infrastructure. As a proof of convergence, in the last 100 calculation steps, the

Table 4.13: *Experimental results of flow rates.*

Flow rates	Air (cone flow-meter)	21.90	Nm^3/h	7.84	g/s
	Air (orifice plate)	22.25	Nm^3/h	7.97	g/s
	Air relative error	-1.6	%		
	Gas (cone flow-meter)	1.233	Nm^3/h	0.265	g/s
	Gas (orifice plate)	1.166	Nm^3/h	0.251	g/s
	Gas relative error	5.5	%		
	Exhaust (orifice plate)	22.00	Nm^3/h	7.71	g/s
	Leakages esteem	6.2	%	0.51	g/s

variation of the monitored temperatures was below 1°C and the related error in thermal balance below 1%. Qualitative results of temperature, velocity and methane mass fraction are shown in Fig. 4.20.

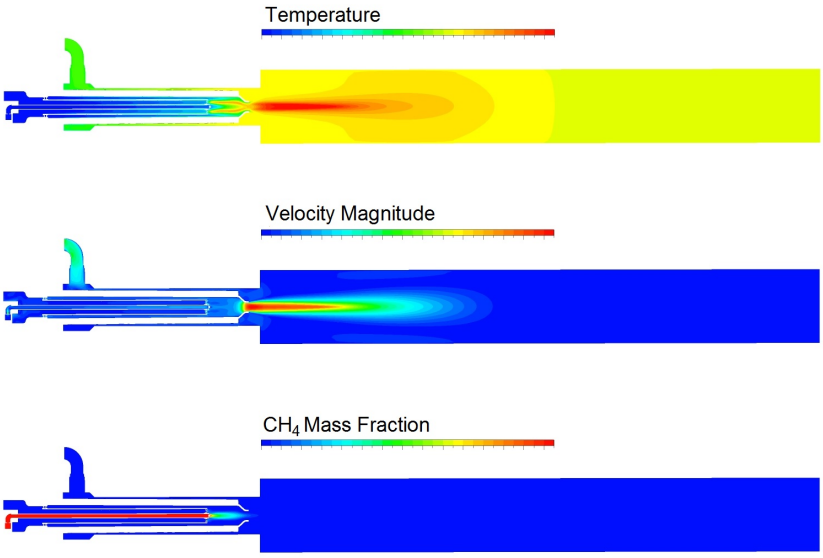

Figure 4.20: *Qualitative contours of temperature, velocity and methane mass fraction in the numerical simulation related to the experimental campaign.*

The comparison between numerical probes and thermocouples temperatures is reported in Tab. 4.14. For what concerns the thermocouples in the room ($T_{c1\div9}$) there was a quite good agreement between simulation and reality with a mean

Table 4.14: *Comparison between experimental and numerical results.*

Thermocouple	Exp.	Num.
Heat exchanger upstream T_{ex}	1170.4°C	1180.2°C
Heat exchanger downstream T_{out}	750.9°C	928.1°C
Primary air near burner's head T_{pr}	370.6°C	146.4°C
Secondary air near burner's head T_{se}	849.0°C	273.8°C
Thermocouple T_{c1}	1185.9°C	1178.2°C
Thermocouple T_{c2}	1203.6°C	1172.0°C
Thermocouple T_{c3}	1227.8°C	1173.3°C
Thermocouple T_{c4}	1206.0°C	1168.4°C
Thermocouple T_{c5}	1041.0°C	1113.9°C
Thermocouple T_{c6}	1042.7°C	1115.4°C
Thermocouple T_{c7}	1042.1°C	1120.9°C
Thermocouple T_{c8}	1046.1°C	1115.5°C
Thermocouple T_{c9}	962.5°C	1015.0°C

discrepancy of about 50°C that can be imputed to the leakages or the walls layers simplifications. Also the overestimation of the mean temperature at the end of the heat exchanger (T_{out}) can be ascribed to the above mentioned approximations. At the entrance of the heat exchanger (T_{ex}) the temperature has been well captured by the numerical model, while for the primary and secondary air ducts (T_{pr} and T_{se}) the errors were quite large.

The reason of this large discrepancy is to be imputed to the huge radial gradient that occurs in the burner's ducts. As shown in Fig. 4.21(b) the temperature trend is very steep because the walls are very hot, due to the high thermal conductivity of iron, while the air is still cold and its velocity is considerably high. For this reasons, the smallest uncertainty in positioning those thermocouples, could bring to large differences in the measured quantities. Thus, T_{pr} and T_{se} were excluded from the comparison.

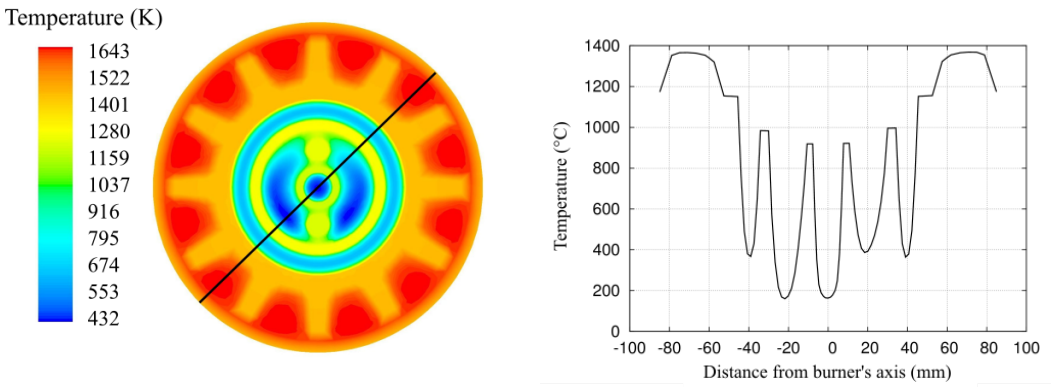

(a) *Contours of temperature.* (b) *Temperature trend on highlighted line.*

Figure 4.21: *Temperatures in a slice plane located upstream of burner's head, where the thermocouples for primary and secondary air are located.*

4.6 Design of Experiment and Burner's Best Configuration

After the validation, the numerical model was used to test in a relatively fast way new geometric configurations of the recuperative burner. Eleven parameters were chosen as input variables for the optimization process aimed at maximizing the recovered thermal power from exhaust gases. Unfortunately, as mentioned before, a direct optimization was considered infeasible due to the large computational time of the single run. A first approach with a *star-point* design of experiment scheme has been carried out, then all the modifications, which presented a positive influence over the recovered heat, were applied simultaneously. As it will be explained in the next paragraphs, a quasi-linear superposition of effects was found. This is probably due to the fact that most of the geometric parameters considered were related to different components of the system and thus did not show a mutual influence.

In the study of the best burner's configuration, the conditions of the experimental campaign were not reproduced, but typical operating conditions of a recuperative burner were implemented. The compositions of Tab. 4.9 were used, with the mass

Table 4.15: *Inlet and outlet boundary conditions for the simulations.*

Air inlet mass flow rate	[g/s]	5.304
Gas inlet mass flow rate	[g/s]	0.274
Air inlet temperature	[°C]	26.5
Gas inlet temperature	[°C]	26.5
Outlet gauge pressure	[Pa]	− 73.6

flow rates reported in Tab. 4.15, in order to generate a thermal power of 13 kW with an air excess of 20 %.

4.6.1 Parameters

As requested by the manufacturing Company, 11 geometric parameters were investigated. Also the range of variability of each parameter was defined in agreement with the Company, in order to respect several constraints related to the manufacturability of the components, the size of the system and its cost of production. The chosen parameters are reported below.

1. **Position of burner's mouth** with respect to the kiln room walls: its influence should concern not only the performance of the systems in terms of recovered heat, but also in terms of temperature profile on the ceramic tiles plane. The burner can not protrude from the walls towards the center of the kiln room, in order to avoid obstructions in the continuous firing process.

2. **Length of the combustion chamber**: affects the percentages of internal and external combustion, thus influencing also the production of thermal power inside and outside the burner.

3. **Length of the heat exchanger**: this parameter should be as high as possible with respect to limits on the size of the system.

4. **Chamfer dimension** of the hole realised in the kiln's wall for housing the burner: it should invite the exhaust gases to flow through the heat exchanger.

5. **Length of the *swirler*** component: not a strong impact on performances is expected by this parameter.

6. **Angle of swirl** impressed to secondary air: it has been widely investigated in § 4.2, its influence on recovered thermal power has to be studied also in the complete model. However, the inclination of the flux should not be too high not to increase the concentrated pressure losses.

7. **Dimension and number of passages** through the swirl component: this will affect the division between primary and secondary air, and can have a sensible impact on the flame geometry and, thus, on the percentage of internal/external combustion.

8. **Number of fins** of the heat exchanger: one of the main parameters related to the fins of the heat exchanger, already investigated in § 4.3. The maximum number has been limited due to problems related to the manufacturability of the SiSiC component.

9. **Width of the fins**: a minimum width has been imposed from the company which produces the heat exchanger.

10. **Height of the fins**: a minimum height has been imposed from the company which produces the heat exchanger.

11. **Gap** between the fins head and the burner housing hole: this is the last parameter related to the fins geometry, it directly influences the section area and thus the velocity of the exhaust gases.

Every simulation has been accurately post-processed, and the heat exchanger efficiency computed. An estimate is also given of the fuel consumption reduction

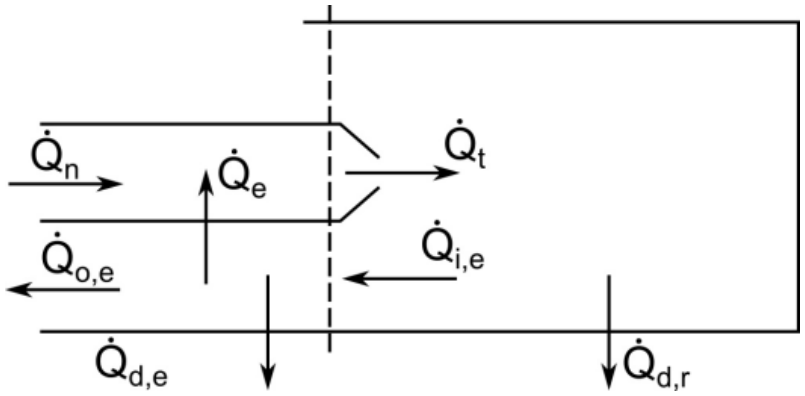

Figure 4.22: *Thermal powers scheme for the recuperative burner.*

achievable, with respect to the basic configuration, under the same operating conditions, this is referred to simply with the term *gain* in the following. The heat exchanger efficiency η and the gain G are defined as follows.

In Fig. 4.22 a scheme of the thermal powers at play is shown. The nominal power $\dot{Q}_n$, generated by the combustion of the natural gas, summed to the power recovered by the heat exchanger $\dot{Q}_e$, forms the total power $\dot{Q}_t$ supplied by the burner into the chamber. Part of the total power is dissipated through room walls $\dot{Q}_{d,r}$, while the remaining amount $\dot{Q}_{i,e}$ enters the heat exchanger. Of the latter, part is recovered $\dot{Q}_e$, part is dissipated through the burner walls $\dot{Q}_{d,e}$, and part exits the system with the exhaust gases $\dot{Q}_{o,e}$ and is sent to the global heat exchange system for further recovery.

All the thermal powers are obtained from the post-processing of the simulations in terms of fluxes through the domain patches. The efficiency of the heat exchanger is computed as the ratio between the power recovered along the heat exchanger $\dot{Q}_e$, and the thermal power available to the fluid at the exchanger inlet section $\dot{Q}_{i,e}$:

$$\eta = \frac{\dot{Q}_e}{\dot{Q}_{i,e}} \tag{4.30}$$

The gain is defined as the difference between the recovered thermal power of a given configuration $\dot{Q}_{e,k}$ and the recovered thermal power of the *basic* configuration

$\dot{Q}_{e,basic}$, divided by the nominal power $\dot{Q}_n$. For the generic configuration k, the gain G_k is:

$$G_k = \frac{\dot{Q}_{e,k} - \dot{Q}_{e,basic}}{\dot{Q}_n} \tag{4.31}$$

Thus, G is an indicator of the rise in the total power available for a given nominal power of fuel. It can also be considered an indicator of the potential fuel saving obtained under a given operating condition. In fact, in order to keep $\dot{Q}_t = \dot{Q}_n + \dot{Q}_e$ constant, if the recovery term rises, the combustible flow rate is lowered along with the nominal power.

4.6.2 Design of Experiment

The sensitivity analysis of the 11 input parameters was carried out following a star-points scheme (see § 3.1.1). A total number of 24 simulations were performed.

- One with the geometric parameters set at their current values (*current* configuration).
- One with the geometric parameters set at their mean values between the minimum and the maximum level chosen (*basic* configuration)
- 22 simulations following the star-point algorithm, where the input parameters are switched individually from the minimum to the maximum level, keeping the remaining variables to the *basic* configuration values.

For the sensitivity analysis purpose the design points were compared with the *basic* configuration, instead of the *current* one, in order to obtain information on the influence of the single parameters. The *basic* configuration showed a significant improvement in the recuperative burner's performance, confirming that the design of the system can operate in a more efficient way.

In Tab. 4.16 and 4.17 the results of the design of experiments are reported respectively in terms of heat exchanger efficiency, as defined in Eq. (4.30), and gain,

Table 4.16: *Heat exchanger efficiency percentage variation with respect to the* basic *configuration.*

		Configurations			
		current	*minimum*	*basic*	*maximum*
Parameters	1		+0.24		−0.44
	2		+2.83		−3.61
	3		−2.94		+2.60
	4		−0.03		−0.37
	5		−0.30		−0.20
	6	−4.45	+0.94	−−	−0.94
	7		+0.27		0.00
	8		−1.15		+1.05
	9		+0.07		0.00
	10		−0.91		+0.84
	11		+0.57		−0.51

as defined in Eq. (4.31). The results are presented with percentage values instead of absolute in order to highlight immediately the positive or negative influence of the design points on the monitored quantity.

As mentioned above, just with the *basic* configuration, which is characterized by the input parameters at their mean values, it was possible to obtain an improvement of almost 5 % in the heat exchanger efficiency and of more than 1 % for what concerns the gain value.

With the modification of the single parameters from the minimum to the maximum admissible values it is possible to achieve further improvement. Due to the nature of the problem and the small ranges of variability, for almost each parameter between the trend of variation for the monitored quantities was monotone. This means that the parameter optimum value did not lie in the middle of the range, but was located in one of the extremes. The monotone trend could be observed for almost all input parameters and when it was not present, the entity of percentage variation was very small; for example, the swirler length for the heat exchanger efficiency (parameter 5 in Tab. 4.16) or the chamfer dimension for the gain G (pa-

Table 4.17: *Gain G percentage variation with respect to the basic configuration.*

		Configurations			
		current	*minimum*	*basic*	*maximum*
Parameters	1		+0.24		−0.07
	2		+1.08		−1.25
	3		−0.80		+0.86
	4		+0.01		+0.10
	5		−0.08		+0.07
	6	−1.02	+0.39	−−	−0.33
	7		+0.06		0.00
	8		−0.15		+0.13
	9		+0.22		0.00
	10		−0.15		+0.28
	11		+0.21		−0.03

rameter 4 in Tab. 4.17). During the operations, some geometric inconsistencies emerged for the swirler gap (parameter 7) and the fins width (parameter 9), thus the simulations of the design points set at their maximum values, were not carried out and a null percentage variation is reported in the results.

The input parameters were divided in *high influence* parameters, *medium influence* parameters and *low influence* parameters. The latter have been neglected in the following analysis, while the former have been investigated in a second phase of the project and in some cases the ranges of variability were expanded in order to increase the recovered thermal power from exhaust gases.

- **High** influence parameters: the combustion chamber length (parameter 2) turned out to be one of the most influencing parameters, it has to be kept as short as possible or it can warm up the exhaust gases in the first portion of the heat exchanger, which is the opposite of the desired effect. As expected, the heat exchanger length (parameter 3) plays a fundamental role and has to be as long as possible. At last, the angle of swirl (parameter 6), as described

in § 4.2, strongly influences the performance of the system.

- **Medium** influence parameters: the parameters related to the fins (parameters $8-11$) have been added to the list of parameters with a medium influence on the performance. This is due to the fact that they are not independent one from another, but there is a strong interconnection between them. Therefore combining their modifications it is possible to obtain a conspicuous improvement of performance (as shown in § 4.3), but the individual contribution of each variable is not so evident. The position of the burner with respect to the kiln's walls (parameter 1) influences the temperature profile in the chamber more than the performance of the recuperative burner. In order to avoid, or at least limit, the backward heat flux from the mixture to the exhaust gases, it is necessary to keep the burner's mouth aligned with the kiln's walls.

- **Low** influence parameters: the realization of the chamfer (parameter 4) is a very expensive operation, while the effect it has on recovery is unremarkable. The same holds for the length of the swirl component (parameter 5), and for the number and the dimensions of its passages (parameter 7).

4.6.3 Best Configuration

After the sensitivity analysis, the second phase of the project took place. A new simulation was performed where all the positive changes had been merged together in order to investigate, at least marginally, the combined effect of the parameters. A quasi-linear superposition of the effects was found. A direct optimization was deemed infeasible due to size of CFD model, and the computational time required. Yet, in the light of the results of this last simulation, a direct optimization would also have been of little interest for this specific case, due to the weak interactions between the parameters found. At this stage only the parameters having a *high* or *medium* influence on the results were included, al the others being left as in the

basic configuration, in order to reduce the complexity and the cost of the burner. As previously mentioned, the range of variation of the swirl angle was expanded in order to further increase the heat recovery. The constraint on the maximum admissible feeding pressure has been used as superior limit for the swirler inclination.

For the new configuration (referred to as "Mod 1"), the *current* one was taken into account in the calculation of the gain, following the equation

$$G_{Mod_k} = \frac{\dot{Q}_{e,Mod_k} - \dot{Q}_{e,current}}{\dot{Q}_n} \tag{4.32}$$

In these conditions G_{Mod_1} grew up to 5%, while the improvement of exchanged heat $\dot{Q}_e$ almost reached 20%, as shown in Tab. 4.18. The optimum configuration was then checked in terms of temperature profile along the chamber floor (see Fig. 4.23). In fact, it is of the utmost importance that this temperature is as uniform as possible in that it is the primary marker of the product firing uniformity and quality. To increase temperature uniformity, in a real kiln operation, two staggered rows of burners are placed on the lateral walls of the kiln, facing each other. In this simplified case, thus, it would be erroneous to consider a uniformity measure of the max-to-min temperature difference kind, since in a real kiln the colder portion in Fig. 4.23 would actually be warmed up by the facing burners. Then, to better focus on the left portion of the plot, the temperature difference ΔT_f between the maximum and the temperature by the burner nozzle on the room floor (coordinate zero in Fig. 4.23) has been chosen as a performance measure.

The difference between the "Mod 1" and the basic configurations is clear. For a quantitative comparison, in Tab. 4.18 the ΔT_f are reported, while for a qualitative visualization, the temperature distribution on the floor are shown in Fig. 4.24. The improvements applied to the burner configuration, heavily affects the heat recovery, but also the geometry of the flame. In particular, the nozzle position with respect to the room walls (parameter 1), has a great influence on the floor temperature profile in the firing room.

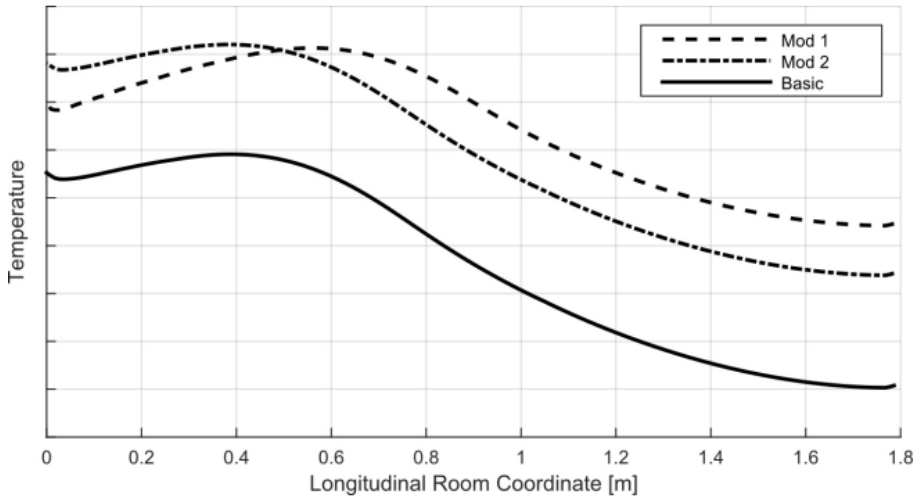

Figure 4.23: *Temperature's profile along chamber floor in three analysed configurations.*

Table 4.18: *Results of the fine tuning configurations.*

Configuration	G [%]	$\dot{Q}_e$ [%]	ΔT_f [K]
Basic	$--$	$--$	10.4
Mod 1	+5.00	+19.52	25.9
Mod 2	+4.72	+18.41	10.6

Therefore, a new configuration (referred to as "Mod 2") was modelled and tested, where the nozzle position is unchanged from the basic configuration. The results show a modest reduction in the gain with respect to "Mod 1" (Tab. 4.18). On the other hand, the same temperature uniformity as in the basic configuration is achieved.

4.6.4 Remarks

The influence of eleven geometric parameters over the heat flux from the exhaust gas to the combustion air was investigated with a design of experiments approach based on the star-points method. Two solutions were proposed, improving the amount of

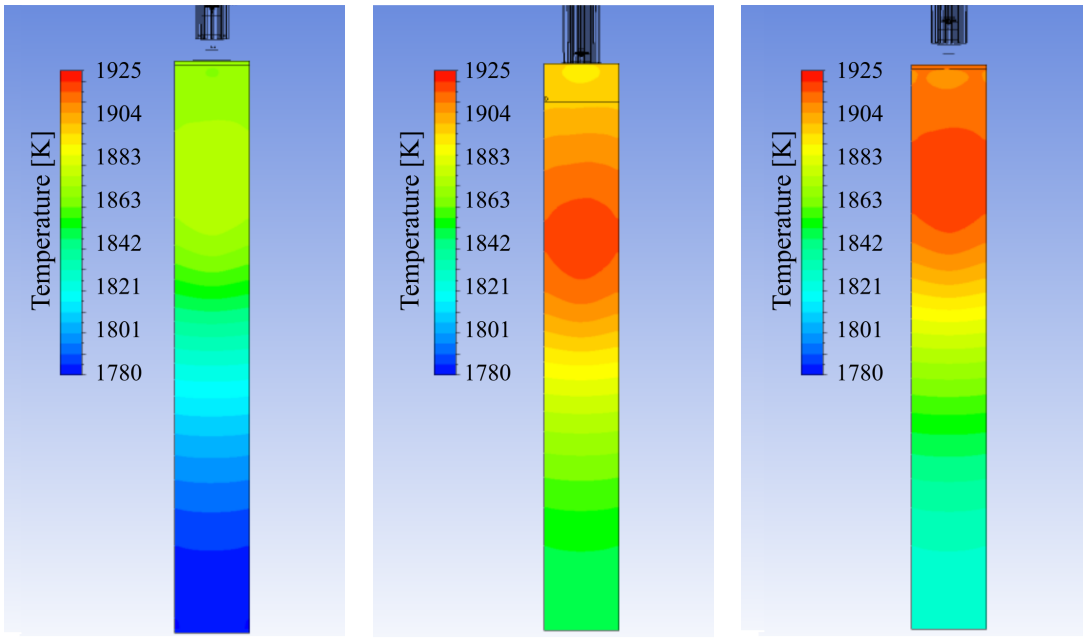

(a) *Current* (b) *Mod 1* (c) *Mod 2*

Figure 4.24: *Temperature distribution on the chamber's floor.*

thermal power recovered by the heat exchanger. The performance of these solutions was compared to those of the *current* burner configuration in terms of potential fuel savings due to better heat recoveries (gain), and temperature uniformity of the chamber floor as a marker of the product firing quality.

The first solution maximizes the heat flux through the exchanger surface, with a 5% gain, but significant lack of temperature uniformity. The second, on the contrary, is able to address the temperature uniformity issue properly. Both cases guarantee a reasonable heat transfer efficiency improvement, with the adjustment of just a few geometrical parameters, mainly related to the double pipe heat exchanger shape.

Of course, the proposed solutions would be able to attain such performances under the assumption that the burner is operated at 13 kW of thermal power. For different operating conditions, also the working point of the heat exchanger and its efficiency would be affected. This implies the need of adopting different burner set-ups for the different burner operating conditions found in an actual kiln.

Table 4.19: *Inlet boundary conditions for the simulation of the 50 kW burner.*

Air inlet mass flow rate	[g/s]	19.520
Gas inlet mass flow rate	[g/s]	1.052
Air inlet temperature	[°C]	26.5
Gas inlet temperature	[°C]	26.5

4.7 Burner Scaling

A similar approach for the definition of an optimum configuration can be adopted for a recuperative burner which belongs to the same family of the one analysed in the previous section. The same computational domain was adopted and the test chamber with the same walls compositions was modelled. This burner is designed to generate 50 kW of thermal power and for that reason some of the dimensions are modified in order to fit the higher mass flow rates. The air and fuel compositions remained the same reported in Tab. 4.9, while the new mass flow inlet boundary conditions are shown in Tab. 4.19 and were chosen to achieve 50 kW of thermal power with an air excess of 15%.

With the higher mass flow rates that came into play, the conditions of full extraction through heat exchanger became excessively unrealistic. Therefore, with specific boundary conditions, the 60% of the total mass was forced to leave the domain through the patch located at the far end of the test chamber, while the remaining 40% was able to wet the heat exchanger before exiting from the usual patch. The mentioned percentage values were decided in accordance with the producing Company and are based on experimental measurements which had been carried out in the past on working kilns.

Thanks to the analysis carried out on the 13 kW burner, in this case it was possible to investigate a lower number of geometric parameters. The *low* influence parameters, such as the dimension of the chamfer or the length of the swirl com-

ponent, were completely neglected. Other parameters were fixed to the extremes of their range of variability due to their evident behaviour in terms of recovered heat from exhaust gases. Therefore the heat exchanger length was maximized and the burner's mouth was aligned with the kiln's walls. The geometric parameters investigated are summarized below.

- **Fins related** parameters
    1. Number of fins
    2. Base width of the fins
    3. Height of the fins
    4. Diameter of the burner housing hole
- **Swirl related** parameter
    5. Angle of swirl
- **Combustion chamber** parameter
    6. Length of the combustion chamber

For each simulation the heat exchanger efficiency was computed. In accordance with the method used for the 13 kW burner, also for this case the achievable reduction of fuel consumption has been esteemed with the calculation of the gain G value with respect to the current configuration. For the simulation k the gain was then computed as

$$G_k = \frac{\dot{Q}_{e,k} - \dot{Q}_{e,current}}{\dot{Q}_n} \tag{4.33}$$

Thanks to the separated outlets, a new power dissipation $\dot{Q}_{d,bot}$ could be individuated in the scheme of Fig. 4.22, related to the percentage of mass which leave the domain through the chamber's bottom patch. Therefore, the thermal power available at

the heat exchanger inlet $\dot{Q}_{i,e} = \dot{Q}_t - \dot{Q}_{d,r} - \dot{Q}_{d,bot}$ has not the same specific weight which used to have in the 13 kW burner simulations. The same was true for the exchanged heat rate $\dot{Q}_e$ and from the thermal power extracted from the exchanger outlet $\dot{Q}_{o,e}$. Thus, compared to the previous burner's case, the average efficiency value, defined as $\dot{Q}_e/\dot{Q}_{i,e}$, practically remained the same, since both the members of the ratio were subjected to the a similar decrease. On the other hand, the gain value, was computed with reference to the increased nominal power, hence lower global values were obtained.

Since the three families of input parameters did not show a strong reciprocal interaction, they have been tested independently in three different phases of the project in order to find the configuration which maximized the recovered heat from exhaust gases. In the first phase the 4 parameters related to the fins shape (or more generally related to the exchanger cross section area) were investigated with a full-factorial design of experiment approach on 2 levels (maximum and minimum in the range of variability). After these first 16 simulations, the best values have been assigned to the respective parameters and in the second phase another full-factorial design of experiment scheme has been performed between the swirl angle (3 levels) and the combustion chamber length (2 levels), for a total number of 6 runs.

The results of the modified configuration are reported in Tab. 4.20 in terms of percentage variation of exchanged heat $\dot{Q}_e$ and gain G with respect to the current configuration. As shown in § 4.3, with higher nominal powers and, thus, mass flow rates, the improvement's margins are smaller and so the gain did not reach 1%, while the heat exchanged was increased by less than 6%. The behaviour of the parameters reflected the one shown by the 13 kW case, with a short combustion chamber, high values of swirl angle and fins number, characterized by a high and thin shape.

The backward heat flux from the combustion chamber to the exhaust duct was observed also in this case. Therefore, a new solution was tested where the fins had

Table 4.20: *Obtained results for 50 kW burner case in terms of gain and percentage variation in recovered thermal power from exhaust gases with respect to the current configuration.*

Configuration	G [%]	$\dot{Q}_e$ [%]
Current	−−	−−
Best w/o fins cut	+0.80	+5.56
Best with fins cut	+1.01	+7.03

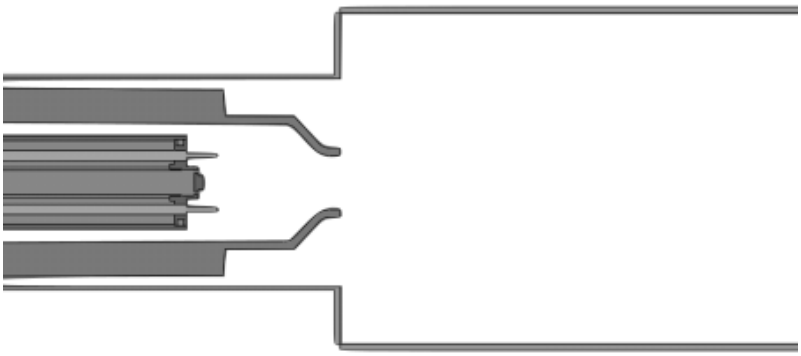

Figure 4.25: *New configuration with fins interrupted in proximity of combustion chamber.*

been removed from the exchanger surface in contact with the combustion chamber (see Fig. 4.25). In this way the heat transfer enhancement was avoided in a portion of the exchanger where it tended to occur in the backward direction.

The results are presented in Tab. 4.20 and showed a little improvement on the heat exchanger performance. In Fig. 4.26 a qualitative comparison is shown in terms of wall heat flux between the configuration without the interruption of the fins (Fig. 4.26(a)) and the one with the fins curtailment (Fig. 4.26(b)). The color scale is limited to 0 as minimum value, so all the blue zones represent a negative (backward) heat flux, from the combustion chamber to the exhaust duct.

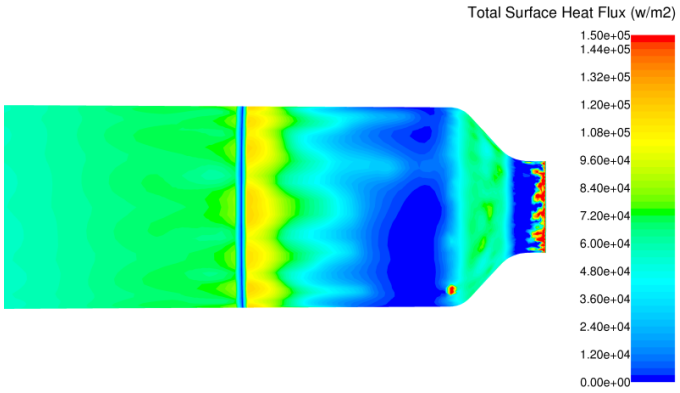

(a) *Without fins cut*

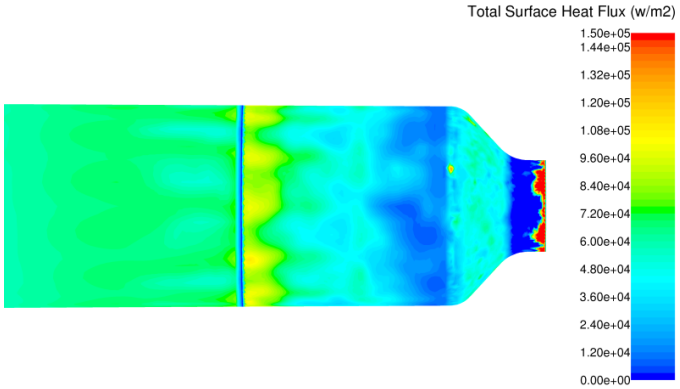

(b) *With fins cut*

Figure 4.26: *Contours of wall heat flux in the configurations without and with the interruption of the fins.*

4.8 Remarks

In this chapter an investigation method for recuperative burners has been presented which includes CFD simulations and design of experiments techniques. The working principle of the recuperative burner investigated was explained and its key features identified as: the heat exchanger characterized by longitudinal fins and the component which impress a swirl motion to the combustion air.

Before approaching the simulation of the complete burner, two simplified studies were conducted in order to better assess the margins of improvement of the system.

The influence on the amount of heat transferred of the swirl component of a generic flux in an annular duct was evaluated. A correlation for the Nusselt number was developed by interpolation of a series of specific numerical simulations. It confirmed the remarkable influence of the swirl angle on the heat exchange, which turned out to be function of the tangent of the average inclination of the flux.

A second simplified study has been carried out on the optimization of a tube-in-tube heat exchanger with longitudinal fins, similar to the one used in the analysed burner. With a dedicated script governing the open source CFD code *OpenFOAM* a direct optimization was performed with the Nelder & Mead simplex algorithm.

Finally, the simulation of the complete system was defined. An experimental campaign was conducted in order to validate the virtual model. With a star-point method, 11 geometric parameters were tested and their influence on the recovered thermal power was assessed. An optimum configuration was found which improved the performance of the recuperative burner with an esteemed fuel saving of 5%. With a similar approach the optimum configuration for a bigger size recuperative burner was predicted.

Chapter 5

An Exhaust Gas Recirculation Burner: Preliminary Analysis

The most critical drawback of recuperative burners is the increase in NO_x production due to the higher flame temperature that may occur in the combustion chamber. This phenomenon can be mitigated by decreasing the amount of natural gas introduced in the system, thus reducing the flame temperature's peak. However, this practice would require a fast and reliable control system in order to avoid an undesired temperature drop, flame's quenching or other malfunctions that can negatively impact the firing process. For this reasons the kilns' users tend to keep higher mixture temperatures in order to preserve the productivity of their companies.

In the recuperative burner studied, the combustion process is of the *staged* kind. The natural gas is firstly mixed with the primary air forming a rich mixture. The secondary air, also thanks to its swirl motion, is kept away from the central core of the flame and, just in proximity of the burner's nozzle, encounters the main flux forming a lean mixture. Both rich and lean mixtures prevent NO_x formation [16].

Nevertheless, the most effective way to contrast the production of pollutant agents is the flue gas recirculation technique. As mentioned in § 1, in this systems a small amount of exhaust gas is directed to the combustion chamber to be burnt again. The temperature of the process then decreases due to the presence of an

additional relatively cold mass. The only widespread application of flue gas recirculation in the ceramic industry is represented by the radiant burner already presented in § 1 (see Fig. 1.4).

In this chapter, a burner's prototype with flue gas recirculation is discussed. It exploits the principle of the radiant burners (a sort of *jet-pump* effect) but in this case the hot gases are expelled directly into the kiln room. The key features of this machine were studied with CFD simulations and optimization processes based on response surfaces were carried out to assess the capability and the drawbacks of the system.

5.1 Working Principle of the System

The mandatory requirements of the new system were individuated to be configuration compactness and operative robustness. In fact, the burner with gas recirculation should occupy the housing hole built for the standard ones in order to avoid expensive modifications on the existing kiln walls. Furthermore, it has to be appropriate for a continuous functioning, which means that unwanted events, like flame quenching, have to be avoided and the performance in terms of flame temperature and penetration inside the kiln room must be sufficient for the firing process.

The main goal of the project is, of course, the reduction of the pollutant emissions, but with specific previsions, other benefits may be obtained from this technology. As mentioned before, a general decrease of temperature's peak is expected with gas recirculation; on the other hand, by increasing the mass flow rate at play, a higher value of the efflux velocity is expected from the burner's mouth. For this reason, the penetration capability of the hot jet into the kiln room will be increased, thus enhancing the mixing and the temperature's uniformity within the kiln. From this point of view, in order to restore the efflux velocity values of a standard system, it should be possible to slightly decrease the fuel mass flow rate, thus reducing the

burner's nominal power and the temperature of the process, which directly affects the velocities. The drawback of such a solution could be an excessive abatement of the temperature, which also has a strong impact on the firing quality along with uniformity, and thus should be kept above a minimum threshold.

Another solution concerns the housing of these particular burners in the cooling zone of the kiln, where fresh air jets are introduced in the domain and there are large concentrations of O_2 in the flue gas. The recirculation of this O_2-rich mixture should allow a reduction of the combustion air supplied to the burner and a global decrease of the mass to be heated inside the kiln. This will also reduce the longitudinal velocity of exhaust gas with a direct impact on temperature uniformity and firing quality. However, this solution could be difficult to control because, as it will be explained in next sections, the amount of recirculated gas strongly depends on the combustion air flow rate and, thus, the robustness of the system could be compromised.

5.1.1 Jet Pump

The recirculation of exhaust gas from the kiln's room inside the burner was achieved exploiting the working principles of *jet pumps*. The functioning of these system is shown in Fig. 5.1. The motive fluid at high pressure is injected into the system through a nozzle. The pressure energy is converted into kinetic energy, thus creating a low pressure zone where the second fluid is entrained. The mixture then is pushed inside a Venturi tube where the pressure is kept at low values in the convergent portion and then increases again in the final diverging section. In essence, the pressure energy of the inlet motive fluid is converted to kinetic energy in the form of velocity head at the throat of the Venturi.

The reliable physical principles on which this technology is based may be challenged by the presence of the combustion process which causes a sudden increase in pressure and temperature. This phenomenon is opposed to the local pressure

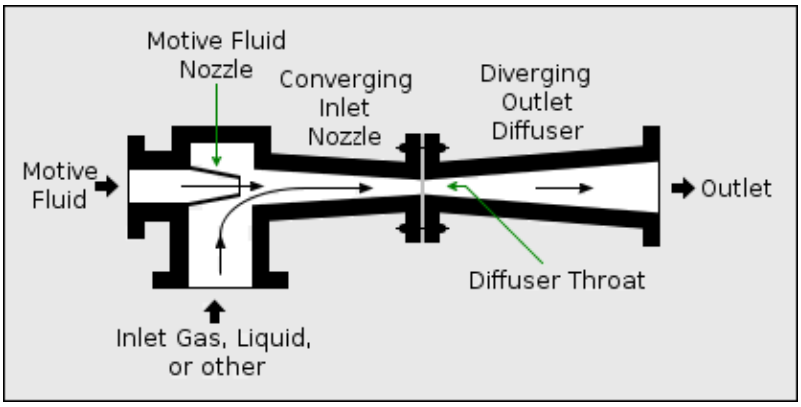

Figure 5.1: *Jet pumps working principle*

abatement, responsible for the entrainment effect of the fluid. Therefore, the classic configuration of the *jet pumps* has to be tested numerically in such critical conditions before proceeding with the development of a prototype.

5.1.2 The Venturi Burner

The chosen layout for the burner with exhaust gas recirculation is schematically represented in Fig. 5.2. The geometry is shown exploiting the axisymmetry of the problem, which will also be one of the strong simplifications in the numerical model, as it will explained in next sections. The fundamental characteristic of the *jet pumps* were maintained:

- The combustion air (dark blue line in Fig. 5.2) is injected in the system through an annular nozzle to generate the entrainment effect.
- The first portion of the SiSiC body of the burner is shaped as a Venturi, with a convergent-divergent section in order to keep the pressure at low levels in this zone, separating it from the combustion chamber, where high pressure will occur. The recirculated amount of exhaust gas is represented with a yellow line in Fig. 5.2.

Anyway, the main features of a classic burner are also implemented in the config-

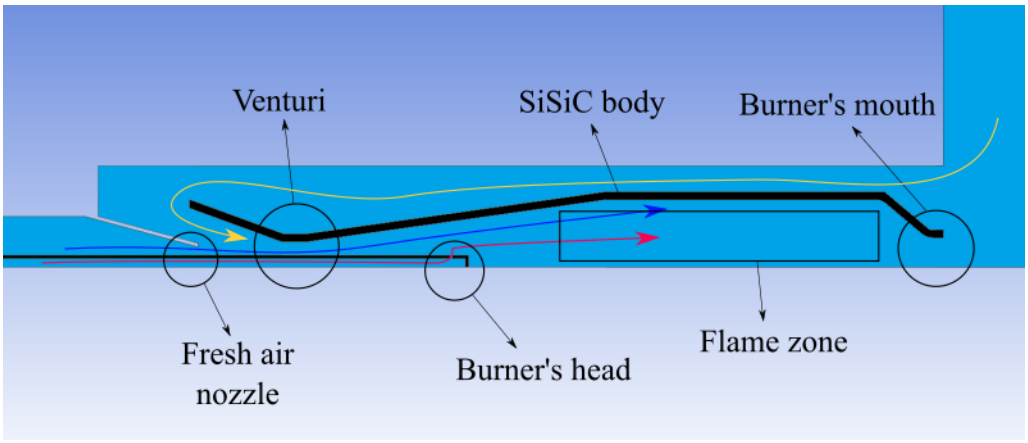

Figure 5.2: *Schematic representation of the burner with exhaust gas recirculation.*

uration studied and, as mentioned before, some of them can affect the *jet pump* principle. In particular:

- The natural gas (red line in Fig. 5.2) duct is inserted inside the combustion air nozzle and passes also through the Venturi shaped portion of the burner. In this preliminary phase of the project the fuel is mixed with combustion air with simple radial holes, avoiding the presence of a complex burner's head.

- In order to impress an acceptable discharge velocity to the hot jet, thus increasing its penetration capability inside the kiln longitudinal flux, the final portion of the SiSiC burner's body, presents a convergent mouth. This represents an unwanted concentrated pressure loss.

- An additional, even more relevant, pressure loss is due to the combustion process that occurs in the volume between the burner's head, where the gas flows in, and the burner's mouth, where the mixture leaves the domain. In this volume, which can be referred as the combustion chamber, temperature and pressure undergo a fast raising, opposing the low pressure that occurs in the throat of the Venturi.

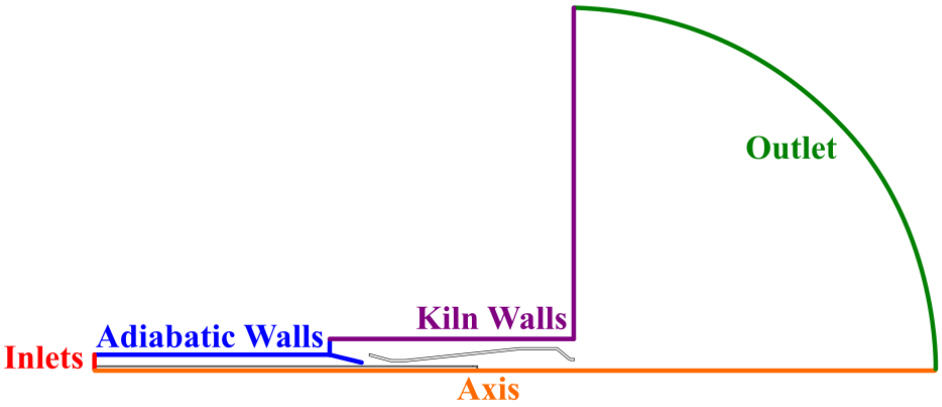

Figure 5.3: *The modelled domain with boundary patches specifications.*

5.2 CFD Model

In this section the CFD model developed is described. Since this work took place in the first stages of the project, a lot of tests had to be done in a short period, in order to obtain a first reliable configuration of the prototype. Therefore, the numerical simulations were simplified as much as possible in terms of both grid dimension and physical models.

5.2.1 Geometry and Mesh

The first decision, in order to save computational time, concerned the dimension of the numerical simulations. An axisymmetric bi-dimensional model was developed and required some simplifications from both a geometric and a physical point of view.

Just a spherical portion of the kiln environment was considered downstream to the burner (Fig. 5.3). The body of the burner, made by silicon infiltrated silicon carbide was discretized as well as the iron tube for the natural gas feeding, while the combustion air duct, with the convergent nozzle was excluded from the simulation.

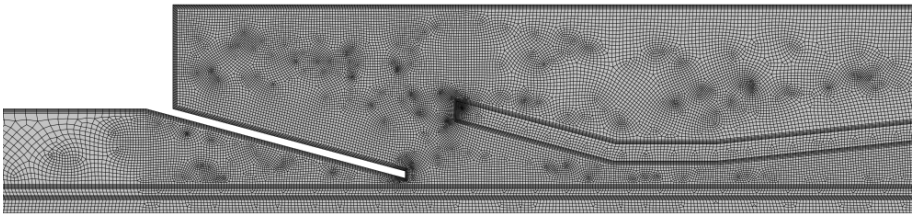

Figure 5.4: *Computational grid of the exhaust gas recirculation burner.*

The only geometric approximation, due to the axisymmetric simplification, concerns the radial holes of the natural gas feeding duct, which were modelled as a continuous cylindrical gap in place of a discrete numbers of holes. However, the useful information about natural gas inlet is related to its velocity (from which depends the mixing with combustion air) and it can be easily investigated in two dimensions. In the three dimensions passage, with specific cross section areas it will be possible to reproduce the same velocity.

On the other hand, from a physical point of view, the influence of gravity has been neglected as well as the presence of swirl effects.

The computational grid is shown in Fig. 5.4. It is characterized by structured boundary layers at the walls with a quadrilateral pave in the remaining zones. The total number of elements was below 200000 for all the generated models. Also in this case the meshing process was fully automatic and robust.

5.2.2 Thermo-physical Models

As mentioned before, due to the axisymmetry simplification, the buoyancy effects were neglected in these simulations. The radiation was taken into account with the Discrete Ordinates model and the turbulence with the k-ω SST model with Low-Re correction.

Regarding the combustion, in this case pure methane was used as fuel, while the

Table 5.1: *Composition of gas and air used in the simulations in volume and mass fraction.*

Component	Air		Gas	
	Volume	Mass	Volume	Mass
CH_4	– %	– %	100.00 %	100.00 %
O_2	21.00 %	23.29 %	– %	– %
N_2	79.00 %	76.71 %	– %	– %

classic composition for ambient air was implemented as reported in Tab. 5.1. The thermophysical properties dependence on temperature has been taken into account in Fluent.

The reaction rates were computed with Eddy Dissipation model, while no NO_x formation model was activated in order to save computational time. In this first stage of the project, the performances of the burner were assessed mainly in terms of penetration capability inside the kiln's flow regime and amount of recirculated exhaust gases. Thus the pollutant formation was neglected.

The solid materials were implemented with the same characteristics described in § 4.4.2.

5.2.3 Boundary Conditions

The schematic representation of the boundary conditions is reported in Fig. 5.3. A fixed mass flow rate condition was imposed at the separated inlets for air and methane. The values are such that 25 kW of thermal power would be generated from the complete combustion of the fuel with an air excess of 20% (see Tab. 5.2). At the outlet the gauge pressure was fixed at 0 Pa (ambient pressure), while specific conditions were imposed for the backward flux that may occur due to the recirculation effect. In particular, for what concern the temperature, a value of 1200°C, typical of the kiln's room, was set. The gas composition resulting from the complete combustion of methane was implemented for the closure of the species equations.

Table 5.2: *Inlet and outlet boundary conditions for the simulations.*

Air inlet mass flow rate	[g/s]	0.50
Gas inlet mass flow rate	[g/s]	10.24
Air inlet temperature	[°C]	25.0
Gas inlet temperature	[°C]	25.0
Outlet backward temperature	[°C]	1200
Outlet gauge pressure	[Pa]	0

The walls were divided into adiabatic and non-adiabatic. The former comprehend all the relatively cold zones near the fresh combustion air inlet (see Fig. 5.3), while for the latter, the dispersions were calculated as in the recuperative burner model by implementing the different layers in the model with a fixed external temperature of 25°C and HTC of 12 W/m^{2}K.

A *pressure based coupled* algorithm was used with a first order schemes for the spatial discretization of the equation to improve stability. During the last part of the simulation second order schemes were adopted for what concerns energy, species and radiation equations. One run took about 5000 iterations to reach the full convergence and lasted 2 hours on a cluster with 128 cores.

5.3 Design of Experiment and Optimization

With the same procedure adopted for the recuperative burner, also in this case some geometric parameters were individuated and varied in the simulations. A series of runs were performed by exploiting different algorithms for design of experiments. With the design points obtained a response surface was defined. Then, with specific optimization algorithms, the configurations that maximized the recirculation entity and the momentum of the mixture at burner's mouth, were predicted. The results of this response surface optimization were then tested with dedicated simulations.

5.3.1 Parameters

In this study, after some physical and technological considerations, 5 input geometric parameters have been chosen. By varying those parameters, the performances of the system were tested in order to discard some clearly defective solutions. The chosen parameters are summarized below:

- **Venturi throat diameter** $[D_t]$: the minimum diameter of the burner's body, it is responsible for the separation between the low pressure zone where the exhaust gases are entrained and the combustion chamber where temperature and pressure undergo a fast increment.

- **Nozzle diameter** $[D_n]$: the external diameter of the annular inlet section of fresh combustion air. It will be one of the most influencing parameters in the analysis: the higher the velocity, the more significant will be the entrainment phenomenon. The superior limit to inlet velocity is represented by the maximum admissible delivery pressure in the air feeding line.

- **Burner's mouth diameter** $[D_b]$: the final diameter of the burner's body. As already mentioned, it has to be as small as possible to increase the discharge

velocity of the mixture flow and, thus, the penetration inside the kiln environment. On the other hand, it represents a concentrated pressure loss opposed to the *jet pump* effect.

- **Combustion chamber length** [L_{cc}]: axial distance between the natural gas radial holes (where the flame starts) and the burner's mouth. It represents the volume where the combustion phenomena take place. Both the momentum of discharge mixture and the amount of recirculated exhaust gas will be strongly affected by this parameter.

- **Position of air nozzle** [P_n]: axial distance between the combustion air nozzle and the burner's body inlet.

The ranges of variability for these parameters were chosen exploiting the experience acquired with the previous studies, trying to respect both operational and technological constraints. For a definitive engineering of the burner, the producing Company will be involved.

The performance of the system was evaluated from the observation of the following output parameters, which were used as objectives or constraints for the optimization process.

- **Amount of recirculated exhaust gas** [R_{ex}]: the mass flow rate of recirculated exhaust gas expressed as percentage of the total incoming mass flow rate (air and methane). The flame temperature is directly influenced by this parameters as well as the NO_x formation, which decrease for high amounts of recirculated exhaust gases.

- **Discharge momentum** [M_{dis}]: momentum of the hot mixture that leaves the burner's body and enters in the kiln environment. It was computed as the product of the mean axial velocity and the mass flow rate at burner's mouth, then it is dimensionally equivalent to a force [N]. This parameter is related

to the penetration capabilities of the burner and, thus, to the uniformity of temperature inside the kiln environment.

- **Delivery pressure of fresh air** [p_{del}]: this parameter was implemented to check the feasibility of the solution and will be used as a constraint for the optimization. It is directly influenced by the efflux velocity through the fresh air nozzle, which is responsible for the entrainment effect of exhaust gas.

5.3.2 Design of Experiments

In order to investigate the influence of each parameter, a sensitivity analysis, based on the star-point (§ 3.1.1) algorithm, was carried out. A *basic* configuration, with all the parameters at their mean values, was tested and then each variable was individually varied between its minimum and its maximum for a total number of $1 + 5 \cdot 2 = 11$ simulations.

The results are reported in Tab. 5.3. Both recirculated amount of exhaust gas R_{ex} and discharge momentum M_{dis} are computed as percentage variation with respect to the basic configuration, while the delivery pressure p_{del} is expressed in terms of relative pressure [Pa]. The most influencing parameter on both R_{ex} and M_{dis} was the diameter of the fresh air nozzle D_n, directly related to its velocity. It should be kept as small as possible to increase the performance of the system, compatibly with the delivery pressure limit of the feeding line. In the subsequent analysis this parameter has been still varied in order to obtain different solution for different feeding line capabilities.

Also the diameter of the burner's mouth D_b turned out to have a great influence on the results, with large diameters the concentrated pressure losses decrease and the efficiency of the entrainment effect is maximized. However the velocity of the discharge mixture dramatically decrease due to the cross section area growth. For this reasons in the successive analysis this parameter was fixed to its *basic* value in

Table 5.3: *Results of sensitivity analysis with star-point algorithm.*

	D_t	D_n	D_b	L_{cc}	P_n	
R_{ex} [%]	−16.83	+71.63	−62.50	+ 2.40	−12.02	min
			0.00			*basic*
	−17.79	−53.85	+16.83	−25.96	−10.10	max
M_{dis} [%]	− 5.33	+37.33	−10.67	−17.33	− 2.67	min
			0.00			*basic*
	− 8.00	−26.67	− 8.00	+ 2.67	−10.67	max
p_{del} [Pa]	2178	6082	2188	2197	2178	min
			2188			*basic*
	2188	1109	2197	2188	2207	max

order not to counteract the entrainment effect without renouncing to decent values of efflux velocity, and thus momentum, at the burner's mouth.

The combustion chamber length L_{cc} had a fair influence on monitored variables and was included in the successive simulations. With long combustion chamber the temperature and the pressure of the mixture increase, thus resulting in an increment of discharge momentum. On the other hand the higher pressure field penalizes the entrainment effect and the exhaust gas recirculation.

The remaining input parameters did not show a sensible influence on the results. The diameter of the throat of the Venturi D_t was neglected in the prosecution of the study and it was also fixed at a value higher than the one of the burner's mouth D_b in order not to compromise the *jet pump* effect. The position of fresh air nozzle P_n was investigated in the subsequent simulations to better test its interaction with other parameters.

In the second phase of the project, the diameters of Venturi throat and burner's mouth have been fixed to specific values while the remaining were varied following a design of experiments scheme based on a full-factorial algorithm. Just two levels were implemented, the maximum (+) and the minimum (−) values for each variables, for

Table 5.4: *Results of full-factorial analysis.*

D_n	L_{cc}	P_n	R_{ex} [%]	M_{dis} [%]	p_{del} [Pa]
+	+	+	− 87.02	−30.67	1099
+	+	−	− 75.00	−21.33	1109
+	−	+	− 34.13	−37.33	1109
+	−	−	− 39.42	−33.33	1109
−	+	+	+ 50.48	+42.67	6072
−	+	−	+ 46.63	+46.67	6063
−	−	+	+102.88	+20.00	6072
−	−	−	+ 72.12	+12.00	6053

a total number of $2 \times 2 \times 2 = 8$ simulations.

The results of this second stage are summarized in Tab. 5.4. Like in the previous analysis, they are expressed in terms of percentage variation with respect to the *basic* configuration for what concerns the recirculation R_{ex} and the momentum M_{dis}, while the p_{del} is reported in Pascal.

As expected, the delivery pressure was influenced only by the diameter of the fresh air nozzle and, in order to realize an efficient gas recirculation system the feeding line must ensure a pressure jump of at least 2000 Pa above atmospheric value. With smaller diameters and higher pressure values it is possible to easily double the amount of recirculated gas and, thus, the total momentum at discharge section.

The fresh air nozzle should not be positioned close to the burner's body intake section in order to maximize the entrainment effect. While the influence of the combustion chamber length was remarked by this second series of simulations. With long combustion chamber the momentum could be maximized due to high pressure and temperature of the mixture, but the amount of recirculated exhaust gas tended to be reduced. With short combustion chamber the entrainment effect was not prevented by the downstream high pressures, but the penetration capabilities of the

system could not reach their optimum.

5.3.3 Response Surface Optimization

The last stage of the study of this burner with exhaust gas recirculation involved the direct optimization on a response surface (§ 3.2). In order to obtain a more reliable and detailed analysis, another series of simulations was carried out, where a latin-hypercube scheme (§ 3.1.3) was exploited, varying all 5 input parameters. In this way the design space was covered with 20 additional design points.

The interpolating function of the response surface (RS) was obtained exploiting the Kriging method [27] on the 39 available design points (11 from star-point scheme, 8 from full-factorial and 20 from latin-hypercube). The operations were carried out with the ANSYS software suite, which implements this techniques. In particular, three RSs were defined, each located in a 6-dimensional space with the 5 input parameters as independent variables and one of the output parameter (R_{ex}, M_{dis} and p_{del}) as dependent variable.

A series of 6 optimization processes on the RS was carried out inside ANSYS environment exploiting the implemented genetic algorithm. First the recirculation R_{ex} and then the momentum M_{dis} were maximized. This operation was repeated with three different delivery pressure p_{del} constraints in order to assess the performances for different feeding line layouts.

The values of Venturi throat and burner's mouth diameter, D_t and D_b, were fixed for the reasons mentioned in previous sections. In this case also the position of fresh air nozzle P_n was imposed at its mean value due to its low influence on the results. In this way, just the nozzle diameter D_n and the combustion chamber length L_{cc} were varied.

The computational time spent for these optimization processes was really short (around 1 minute) because each member of the population (each set of input parameters) was tested with the RS and not with a complete CFD simulation. The

Table 5.5: *Results of optimization process. For the input parameters, 0 means that they assumed the minimum value in chosen range and 1 the maximum.*

Constraint	Objective	R_{ex} [%]	M_{dis} [%]	D_n [fraction]	L_{cc} [fraction]
$p_{del} \leq 2000$ Pa	max R_{ex}	-27.40	$-\ 2.80$	0.46	0.03
	max M_{dis}	-34.62	$-\ 2.40$	0.44	0.03
$p_{del} \leq 4000$ Pa	max R_{ex}	$+37.50$	$+10.93$	0.78	0.65
	max M_{dis}	$+\ 5.77$	$+19.73$	0.78	0.04
$p_{del} \leq 6000$ Pa	max R_{ex}	$+97.60$	$+22.80$	0.99	0.94
	max M_{dis}	$+59.62$	$+47.33$	0.99	0.03

results are summarized in Tab. 5.5. As usual R_{ex} and M_{dis} are expressed in terms of percentage variation with respect to the *basic* configuration. The outcome of an optimization process consists in the optimum set of input parameters. Therefore in Tab. 5.5 the values of D_n and L_{cc} are reported as a fraction of the available variability ranges. Therefore, 0 means that the input parameters assumed its minimum value and 1 means that the maximum has been chosen.

Also this analysis confirmed the fundamental role of the fresh air inlet velocity for the entrainment effect and, more in general, for the performance of the whole system. When the constraint on pressure is particularly restrictive ($p_{del} < 2000$ Pa) the configurations of maximum recirculation and maximum momentum are practically the same. In these conditions, the influence of secondary parameters, such as the combustion chamber length L_{cc}, were negligible, due to the absence of the motive force of the system. It has to be noted that the results are reported in terms of percentage variation with respect to the *basic* case, however in absolute terms, all the configurations of Tab. 5.5 showed an active recirculation always above 10% of the total input mass flow rate. The velocity vectors of a generic case are shown in Fig 5.5 in normalized form, the recirculation of exhaust gas can be clearly seen.

If higher delivery pressures are available in fresh air feeding line, then the differ-

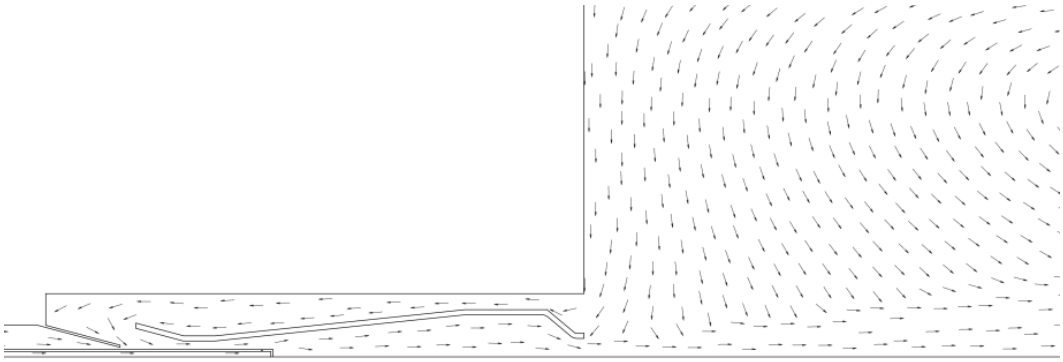

Figure 5.5: *Velocity vectors that highlight the recirculation effect.*

ences between *max* R_{ex} and *max* M_{dis} configurations become more evident. With $p_{del} < 4000$ Pa and $p_{del} < 6000$ Pa the influence of combustion chamber length on the performances of the system was confirmed once again. The recirculation of exhaust gas reached its maximum with short combustion chamber, due to the lower pressure developed downstream the Venturi throat. In this case the combustion process was half completed outside the burner's body. With long combustion chamber the opposite effects occurred, and the momentum of hot mixture at burner's mouth reached its maximum value.

In Fig. 5.6 a qualitative comparison is shown between the static pressure fields in maximum R_{ex} and maximum M_{dis} configurations with the $p_{del} < 6000$ Pa active constraint. The lower pressure can be clearly observed in the former image (Fig. 5.6(b)), where the entrainment effect was enhanced. Also a quantitative evaluation of the pressure field was performed for the two cases considered and it is represented in Fig. 5.7, where the pressure abatement in Venturi's throat is more evident for the maximum recirculation configuration (green line).

The temperature contours are shown in Fig. 5.8. In agreement to the previous observations, with long combustion chambers the combustion process was almost fully developed inside the burner, where the mixture's temperature raised. However, a general decrease in the peak flame temperature can be observed due to the

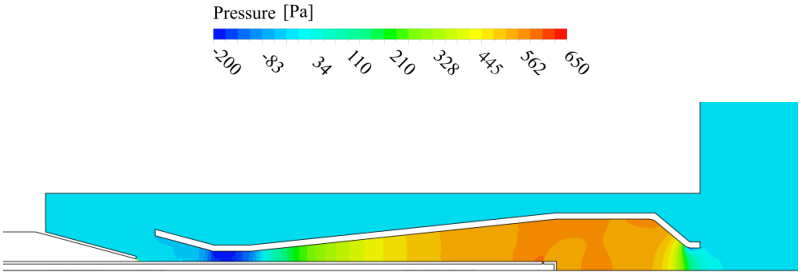

(b) *Configuration for maximum recirculation of exhaust gas*

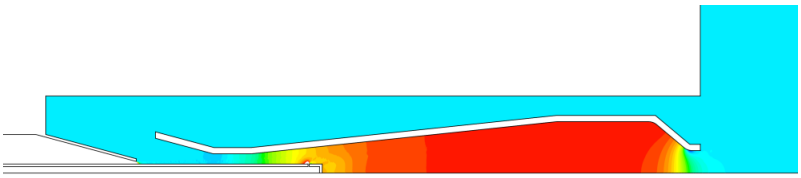

(c) *Configuration for maximum momentum at burner's mouth*

Figure 5.6: *Static pressure contours for the optimization processes carried out with* $p_{del} < 6000$ *Pa constraint.*

amount of exhaust gas recirculated. Thus, a consistent abatement in NO_x production is expected.

Also the velocity field showed a net increase in the configurations with long combustion chamber and the momentum of the mixture at burner's mouth reached its maximum, as it represented in Fig. 5.9.

5.4 Remarks

The design of an innovative burner for exhaust gas recirculation was proposed and discussed in this chapter. The main characteristic of the burner are compactness and interchangeability with other machines installed on existing kilns for ceramic industry. The flue gas are entrained in the burner's combustion chamber exploiting the low pressure zones created by a high velocity jet of fresh air, as it occurs in *jet pumps* systems.

A simplified 2D CFD model was developed, the axisymmetry of the problem was

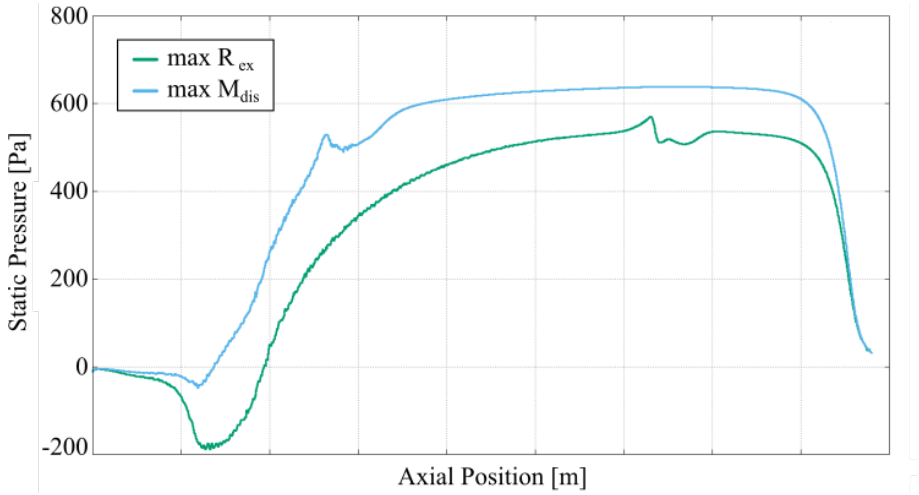

Figure 5.7: *Static pressure plot along the axial coordinate in the combustion chamber zone for the optimization processes with* $p_{del} < 6000$ *Pa constraint.*

exploited and the buoyancy and swirling effects neglected, in order to obtain a fair compromise between accuracy and calculation speed. 5 geometric parameters were varied with a series of design of experiment schemes, and their influence on system's performance was assessed. Finally 6 direct optimization processes were carried out with the genetic algorithm implemented in ANSYS software suite. The objectives of these optimizations were the maximization of recirculated amount of flue gas and the maximization of mixture's momentum at the burner's mouth, each one tested with three different constraints on delivery pressure for combustion air feeding line.

The velocity of the fresh air jet turned out to be the most important parameter for the performance of the system, while the combustion chamber's length can be varied in order to maximize the entity of recirculation (short chamber) or the discharge momentum (long chamber). A general decrease in flame temperatures could be observed in the virtual models developed, but a detailed analysis on the pollutant formation was not carried out.

These data were provided to the Company which produces the burners and will be used to build a first physical prototype.

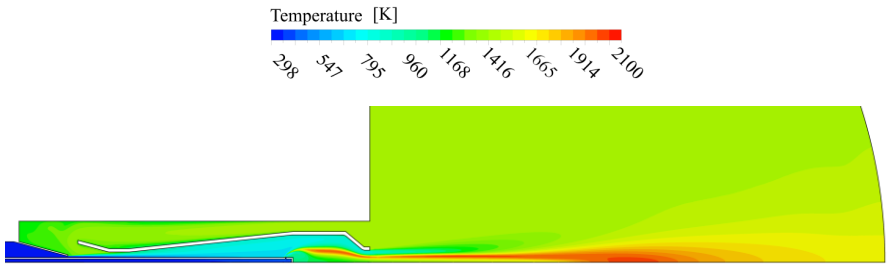

(b) *Configuration for maximum recirculation of exhaust gas*

(c) *Configuration for maximum momentum at burner's mouth*

Figure 5.8: *Temperature contours for the optimization processes carried out with* $p_{del} < 6000$ *Pa constraint.*

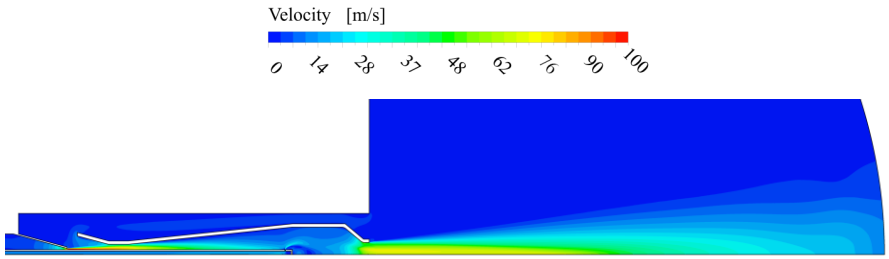

(b) *Configuration for maximum recirculation of exhaust gas*

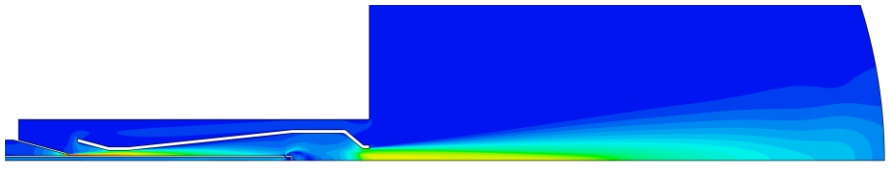

(c) *Configuration for maximum momentum at burner's mouth*

Figure 5.9: *Velocity magnitude contours for the optimization processes carried out with* $p_{del} < 6000$ *Pa constraint.*

Chapter 6

Conclusions

The analysis of several problems related to burners for industrial ceramic kilns has been presented in this thesis. Complex systems were investigated *via* Computational Fluid Dynamics (CFD) tools along with Design of Experiment (DoE) and optimization techniques. This kind of approach, widely diffused in other engineering fields, such as automotive or naval architecture, was introduced and systematically used in the ceramic industry sector.

In particular, two innovative devices were studied: a recuperative burner, able to exploit waste thermal power to preheat combustion air, and a burner with exhaust gas recirculation to limit pollutants' emissions. Both these solutions exploit the hot gases that flow in the kiln environment and are responsible for the firing of ceramic tiles. During this process, about half of the heat introduced is wasted because the flue gases reach the thermal equilibrium with the product and have to be extracted.

6.1 The Recuperative Burner

With recuperative burners the energy contained in flue gas is exploited to preheat combustion air, thus increasing the flame adiabatic temperature. In order to maintain the mixture temperature on standard values, it is possible to reduce the amount of fuel provided to the system, thus saving on operating costs.

The geometry of an existing burner was optimized first, in order to maximize the thermal power recovered from exhaust gas. The burner investigated differs from others due to two particular features: the swirl motion impressed to the combustion air that flows close to the heat exchanger and the shape of the exchanger itself, which is characterized by longitudinal fins. These features and their physical principles were isolated and studied with simplified models, in order to reach the simulation of the entire system with a deeper cognizance of the problem.

The open source CFD software *OpenFOAM* was used to investigate the helical flow in an annular duct, and in particular its effect on the heat transfer enhancement. A huge number of simulations was carried out in a completely automatized way, varying geometric and operative parameters in a full-factorial based DoE scheme. Then, interpolating on numerical results, a new correlation for the Nusselt number was defined. It assumed the form of the well known correlations present in literature, with an additional term for taking into account the effect of the swirl motion.

Together with the assessment of the swirl influence, also the impact of the longitudinal fins on the recovered thermal power was investigated with a simplified approach. A portion of a generic tube-in-tube heat exchanger with longitudinal fins was modelled in *OpenFOAM* and a direct optimization with Nelder & Mead simplex algorithm was performed varying some geometric parameters. The configurations that maximized the heat transfer was found for two operating conditions of the system and they turned out to be consistently different.

The complete model of the recuperative burner was made up within the ANSYS software environment, to include also combustion and radiation processes. It was validated with a dedicated experimental campaign. About 24 hours were required to complete one simulation with an acceptable level of convergence. Therefore a direct optimization was considered infeasible for the purpose of the study and a sensitivity analysis was carried out varying 11 geometric parameters. A quasi-linear

superposition of effects was found when combining all the modifications that enhanced the thermal power recovered from the exhaust gases. The reduction in fuel consumption was esteemed to be around 5%, while the performance of the system in terms of firing quality remained unchanged.

6.2 The Exhaust Gas Recirculation Burner

The exhaust gases can also be exploited to reduce the flame peak temperature by mixing them with combustion air before the reaction occurs. It is a widespread practice in the automotive sector and also in particular applications of manufacturing industry, such as radiative burners. With the reduction of flame temperature it is possible to massively decrease the formation of NO_x, thus respecting the environment or, at least, the pollution laws.

An innovative design of a burner with exhaust gas recirculation for ceramic continuous roller kilns has been investigated. It takes advantage of the entrainment effect exerted by a high velocity fluid, as occurs in *jet pumps*. Therefore the fresh combustion air is injected in the system through a nozzle and drags the exhaust gas into the burner's body, which is shaped as a Venturi tube with a convergent-divergent section. Then the fuel enters the system for the combustion process.

A 2D model was created enforcing the axisymmetry of the problem. The most significant geometric parameters were varied and a sensitivity analysis was performed. The output quantities that were chosen to asses the influence of each variable on the performance of the system were the amount of recirculated gas and the momentum of the mixture at the burner's mouth. The latter was taken as an indicator of the penetration capability of the jet into the kiln's environment and, thus, of the mixing level inside the firing zone, from which temperature uniformity depends.

The most influential parameters were identified and further investigated. A re-

sponse surface was generated interpolating the computed design points and several direct optimization processes were carried out. In particular, with the optimizations, the recirculated amount of exhaust gas and the mixture momentum at burner's mouth were maximized with three different constraint levels on the delivery pressure of the combustion air feeding line.

As expected, the size of the fresh air nozzle (and thus its inlet velocity) strongly affects the entrainment capability of the burner. In order to maximize the momentum of the hot mixture at burner's mouth, the combustion chamber had to be kept as long as possible, allowing the temperature to rise and the burner discharge velocity to increase. On the other hand, this phenomenon created a high pressure area downstream the Venturi's throat, which interferes with the entrainment effect.

The results were provided to the burner manufacturing Company and will help in the development of a first prototype.

Acknowledgements

Tre anni sono volati, il tempo passa in fretta quando ti diverti.
E la cosa più bella è che se mi guardo indietro, nonostante tutto, mi rendo conto di quanto io sia cresciuto dal punto di vista umano e professionale. Certo, mi considero sempre un novizio della CFD o meglio, come direbbe qualcuno, un contadino della turbolenza, ma quello che ho imparato dalle persone con cui ho lavorato in questi anni va oltre le più complesse equazioni di governo della fisica.
E per questo non posso che essere grato.
Ringrazio Marco, fin da subito un amico oltre che un valido collega, ed il professor Corticelli, che mi ha sempre rispettato ed incoraggiato in ogni mia decisione. Non posso poi non ricordare i membri (ufficiali ed onorari) del gruppo di ricerca: Diego, Levo, Betta, Orsola, Enrico ed il professor Barozzi. Tutti sparpagliati per il Dipartimento, per l'Ateneo e addirittura per l'Emilia Romagna, ma sempre disponibili per un consiglio, un aiuto o anche semplicemente un caffè.
Si dice che *"chi ad altri insegna, sè stesso ammaestra"* ed io non so quanto ho insegnato ai tesisti con cui ho avuto a che fare (Martella, Umberto, Gianluca, Caffagni, Giulio, Gian e Pietro), ma sicuramente da ognuno di loro ho ricevuto qualcosa di importante.
Tra i banconi del laboratorio LIFT è passata parecchia gente, proveniente dalla Lombardia, dalla Sicilia e persino dalla Nigeria. Alcuni sono rimasti solo un numero di matricola, altri buoni amici ed altri ancora anche qualcosa di più.
Grazie di tutto. A presto.

Appendices

Appendix A

Paper published on *Applied Thermal Engineering*, Volume 84, pages 110-117, June 2015

Applied Thermal Engineering 84 (2015) 110–117

Contents lists available at ScienceDirect

Applied Thermal Engineering

journal homepage: www.elsevier.com/locate/apthermeng

Research paper

Optimization of a finned concentric pipes heat exchanger for industrial recuperative burners

Marco Cavazzuti*, Elia Agnani, Mauro A. Corticelli

Dipartimento di Ingegneria "Enzo Ferrari", Università degli Studi di Modena e Reggio Emilia, via P. Vivarelli 10, 41125, Modena, Italy

HIGHLIGHTS

- A systematic method for the optimization of a double pipe heat exchanger is proposed.
- The method adopts CFD and a constrained version of the simplex optimization algorithm.
- The exchanger efficiency is optimized under different operating conditions.
- A resistance network analysis is included to address possible further improvements.
- The economic impact of the optimized solution in industrial kilns is estimated.

ARTICLE INFO

Article history:
Received 2 December 2014
Accepted 7 March 2015
Available online 1 April 2015

Keywords:
Heat exchanger efficiency
Industrial recuperative burner
CFD
OpenFOAM
Simplex optimization

ABSTRACT

A numerical application is presented in which a finned concentric pipes heat exchanger is simulated by means of CFD, and optimized by the Nelder and Mead simplex downhill optimization algorithm. The heat exchanger parameterization takes into consideration the main geometrical aspects of the exchanger under different operating conditions. The work originates from an industrial problem related to heat recovery issues in recuperative burners, in which air is pre-heated by the exhaust gas before entering the combustion chamber. Such a device allows for an *in situ* and more efficient heat recovery from exhaust gases, also reducing both the sizing of the heat recovery system downstream to the furnace, and the burner fuel consumption. It is found that the fine tuning of just a few geometrical parameters can result in a sensible enhancement of the exchanger efficiency.

1. Introduction

Heat exchangers are commonly found in industry for transferring heat between two media, and represent a widely investigated research topic. An important application is given by heat recovery in high temperature industrial systems, where the thermal powers at play are large, and so are the margins for energy efficiency improvement.

This is true when dealing with burners for industrial furnaces, and with heat recovery from high temperature exhaust gases. More in general, energy recovery and its better exploitation in high temperature industrial processes have received much attention in literature over the last few years in view of the pressing environmental issues. We thus find works addressing the recovery of pre-heated air from the cooling processes into industrial kilns [1], the exploitment of the heat loss from the mantle of a rotary kiln to pre-heat the combustion air [2], the use of low LHV syngas in adapted industrial burners [3], and kilns [4].

In traditional continuous roller kilns, such as those used for firing ceramic tiles, the burners expel the exhausts directly into the kiln room, where it is sucked by a unique intake manifold upstream by the kiln entrance, and sent to a global heat recovery system.

To better exploit the enthalpy of the exhausts, the heat recovery function can be decentralised and appointed, at least in part, to local recuperative burners. Basically, a heat exchanger is coupled to the burner and used for pre-heating the combustion air with the exhaust gas. Downstream to the burner the exhaust gas is then sent to a global heat exchanger system for further recovery. The simpler and most cost effective heat recovery system that can be thought for the recuperative burner is given by a double pipe exchanger where the exhaust gas flows in a coaxial tube external to the burner itself.

* Corresponding author. Tel.: +39 059 2056347.
E-mail address: marco.cavazzuti@unimore.it (M. Cavazzuti).

http://dx.doi.org/10.1016/j.applthermaleng.2015.03.027
1359-4311/

Nomenclature

A	section area (mm^2)
D_h	hydraulic diameter (mm)
D_i	exchanger pipe inner diameter (mm)
D_o	exchanger pipe outer diameter (mm)
g	fin crest to insulating wall gap (mm)
h_f	fins height (mm)
l_e	exchanger length (mm)
n_f	fins number (−)
p_w	wetted perimeter (mm)
$\dot{Q}$	rate of heat transfer (kW)
R	thermal resistance (°C/kW)
r_f	fins thickness ratio (−)
T	temperature (°C)
t_b	fin base thickness (mm)
t_c	fin crest thickness (mm)
V_e	heat exchanger pipe volume (mm^3)

Greek Symbols

α	domain angular width (rad)
α_b	angle subtended at the fin base thickness (rad)
α_c	angle subtended at the fin crest thickness (rad)
ΔT_b	bulk temperature difference across the heat exchanger (°C)
ΔT_m	log mean temperature difference (K)
λ	equivalence ratio (−)

Subscripts

e	relative to the heat exchanger wall
in	relative to the inlet section
out	relative to the outlet section
s	relative to the secondary air flow
t	total
x	relative to the exhaust gas flow

Such a solution is not particularly efficient due to the low residence time of the gas in the exchanger and the relatively low wetted area. Nonetheless, considering the industrial constraints of low pay-back time, easy manufacturability, need for low maintenance, resistance to high temperatures and chemically aggressive environments, more complex and thermally efficient solutions would be quickly discarded.

The focus is thus on finned concentric pipes heat exchangers made of silicon-infiltrated silicon carbide (SiSiC). The choice for the material is due to its resistance to high temperature and its good thermal conductivity. The simple geometry offers limited margins for optimization, yet a fine tuning of the geometrical parameters could lead to an optimum balance between the extended wetted areas and the allowable pressure drop across the heat exchanger, usually limited due to technological reasons.

The idea of a recuperative burner is not new and was already widely discussed in review papers in the early eighties [5]. The main concern about these systems is their being prone to larger NO_x formation rates due to the higher flame temperatures that are occurring by pre-heating the combustive agent. In such cases, the enhancement of turbulence or the adoption of staged combustion can help in mitigating NO_x production as discussed in Ref. [6].

More recently, research devoted to burners has focused on flameless combustion, also known as Moderate or Intense Low-oxygen Dilution (MILD) combustion. Flameless combustion essentially consists in the recirculation of a given amount of exhaust gases into the combustion chamber. In this way, by smoothing temperature peaks out, a drastic reduction in NO_x formation is obtained [7]. From an industrial point of view other advantages are a more uniform temperature distribution [8], a better flame stability under certain operating conditions [9], and of course a better heat recovery from exhaust gases. Despite this, MILD combustion has not yet spread in industrial applications due to the additional complexity in the burner design given by the need of an exhaust gas recirculation system.

The literature concerning double pipe heat exchangers is very large, and over the years the focus has been on evaluating the effectiveness of several different means for improving the heat transfer going from, to cite a few, the use of fins of various kinds and shapes [10], swirled flows [11], porous structures [12], and so on. A wide review on the use of extended surfaces, such as fins or pins, in heat exchangers is also given in Ref. [13].

The use of optimization methods in heat exchangers design is also a rather discussed topic in literature. Yet, to the authors knowledge, no optimization application is found relative to double pipe finned heat exchangers. Maybe because of their simplicity and relatively low efficiency that limit their use in practical industrial applications. Among the most recurrently optimized types we find plate-fin heat exchangers [14], shell-and-tube heat exchangers [15], and microchannels heat exchangers [16].

Concerning the optimization problem setup, the works either rely on analytical models of the heat exchangers, or on Computational Fluid Dynamics (CFD) simulations. The variables of course are always given by a set of geometry-related parameters, while the constraints, if any, usually regard the admissible pressure drop. Both single and multi-objective optimizations are found, while the use of genetic optimization algorithms is predominant. The most typical objectives relate to thermal and fluid dynamic aspects of the exchangers: maximization of the heat transfer, the temperature jump, or the Nusselt number, and minimization of the pressure drop, or the friction factor as in Ref. [17] and in Ref. [18]. A few studies also involve objective functions generating from economic considerations, such as operative, maintenance, or material costs [19]. Volume minimization is usually addressed in compact heat exchangers applications [20]. A few works also approach the problem in terms of the second law of thermodynamic, thus focussing on the minimization of the entropy production, or of a modified entropy generation number [21].

Only recently, the first works in which the open source CFD code OpenFOAM has been applied to heat exchangers design problems have appeared in literature, as in Ref. [22] where a typical HVAC application heat exchanger is addressed, even though without including optimization methods. One of the latest extended reviews on the use of CFD in heat exchangers design [23], in fact, shows no trace of that code yet.

In the present paper, we address finned concentric pipes heat exchangers. The heat exchange rate is predicted by means of the open source CFD code OpenFOAM, and maximized using the Nelder and Mead simplex optimization algorithm [24] under pressure drop, compactness, and cost-related constraints. The variables of the optimization include several geometrical parameters, mainly related to the shape of the finned surface. The work, even though originating from an industrial problem of heat recovery in recuperative burners for ceramic kilns, follows a general approach having general validity.

2. Problem description

2.1. Geometry

The heat exchanger section of the recuperative burner from which the present study takes hint is made of a series of concentric tubes (Fig. 1(a)). Going from in to out, the two inner tubes are made of iron, the third of SiSiC, while the outer limit of the domain is made of a thick wall of refractory insulating material. Through the inner tube flows the fuel (methane gas), while the combustive agent (air) is split between two more passages (primary and secondary air). Through the outer passage the exhaust gas flows counter-currently to the other flows. The outer surface of the silicon carbide tube is finned for heat exchange enhancement. This allows for a suitable pre-heating of the secondary air, while primary air and methane will remain relatively cold. The subvidision between primary and secondary air allows for a sort of staged combustion where pre-heated air comes into play later, thus reducing NO_x production.

2.2. Simulation

The domain for the simulations of the heat exchanger is chosen exploiting the symmetry of the problem, thus we focus around a single fin as shown in Fig. 1(b). The open source CFD code OpenFOAM 2.3.0 is used for the simulations: in particular the mesh is created with the *blockMesh* application, and the problem is solved using the conjugate heat transfer solver *chtMultiRegionSimpleFoam* with second order discretizations.

The mesh (Fig. 1(c)) is non-conformal, fully hexahedral, and contains between 60,000 and 150,000 elements, depending on the number of fins, and thus on the width of the angular portion of the domain and the exchanger length. The simulations require on average 20 min time to reach convergence running in parallel on a 4 CPUs machine.

k-ω SST turbulence model is adopted, together with the P-1 radiation model. For the given operating conditions, $y^+ < 1$ is always attained at the heat exchanger walls.

The gas phases are treated as perfect gases. Regarding their thermophysical properties, the Sutherland law is used for computing the dynamic viscosities, while JANAF coefficients are used for the specific heats and enthalpies.

Pure methane flows in the inner tube with a mass flow rate chosen so that the expected thermal power developed in the burner would equal 12.5 kW or 25 kW, for these are the two burner operating conditions optimized in this work. The mass flow rate of the air is such that the combustion in the burner would occur with an air-fuel equivalence ratio $\lambda = 1.20$, and is split between primary and secondary air, with the latter accounting for 70 % of the total air flow. 1 % air absolute humidity is assumed. The mass flow rate of the exhaust gas equals the sum of the air and methane flows, and its properties are computed under the assumption of complete combustion of the methane. Since the flows are separated from each other and the study is limited to the heat exchanger area, the simulations include neither species nor combustion modelling. A resume of the characterization of the flows is given in Table 1. Considering the given exhaust gas inlet temperature, it is assumed that the gas enters the heat exchanger with two-third of the sensible enthalpy generated from the combustion, the remaining part being dissipated otherwise within the kiln room. Of course, since only a portion of the exchanger is modelled, the flow boundary conditions are set as the reported mass flow rates divided by the number of fins. Reynolds numbers for the methane and the air passages range between 1900 and 2,700, meaning the flow is either laminar or transitional. For the exhaust passage the Reynolds number is generally lower due to the relatively larger sections, and the high temperatures that translates into low velocity and high kinematic viscosity. Depending on the exhaust passage geometry, which is variable as described in the following, Reynolds number is in the range between 500 and 1,000, where the Reynolds number is based on the hydraulic diameter of the duct. This may not necessarily mean the flow is laminar due to the complex exhaust section shape that makes the choice of the hydraulic diameter ($D_h = 4A/p_w$) as the characteristic length questionable.

Turbulent intensity at the inlet boundaries are set between 6 % and 8 % as computed on the basis of the flow inlet conditions. The insulating wall is modelled adiabatic and with emissivity 0.8, while ambient pressure condition holds at the various outlets.

Concerning the solid walls in the domain, the two inner tubes are made of iron Fe360 and are modelled with constant

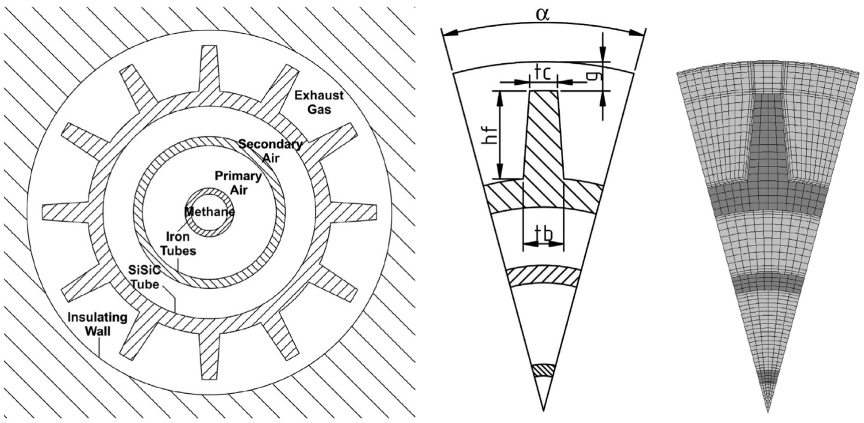

(a) Section of the heat exchanger (b) Section of the domain (c) Section mesh.

Fig. 1. Heat exchanger geometry, computational domain, and mesh.

Table 1
Gas properties and flow conditions.

Gas flow	Molar mass	Mass flow rate (g/s), 12.5 kW case	Inlet temperature (°C)
Methane	16.04	0.251	26.5
Primary air	28.79	1.486	26.5
Secondary air	28.79	3.468	26.5
Exhaust	27.72	5.205	1,300.0

Table 2
Solid properties.

Material	Density ($\frac{kg}{m^3}$)	Thermal conductivity ($\frac{W}{m\,K}$)	Specific heat ($\frac{J}{kg\,K}$)	Emissivity
Fe360	7,850	54	470	0.38
SiSiC	3,120	$206.14-0.1236\cdot T$	$459.69-0.4706\cdot T$	0.90

thermophysical properties. On the contrary, due to the high temperatures of the exhaust gas, the properties of the SiSiC heat exchanger are modelled as linearly dependent upon temperature as in Table 2, where the temperature is expressed in K.

2.3. Optimization

For the optimization of the heat exchanger we consider a design space composed of 6 variables related to the geometry of the exhaust gas passage, and in particular of the fins located on the external surface of the SiSiC tube. The variables are resumed in Table 3 together with their range of variability.

The fins number, despite being an integer variable, is allowed to vary with continuity for the purpose of optimization, and, following the notation in Fig. 1(b), the domain angular width is derived from the fins number as $\alpha = 2\pi/n_f$. The fins crest thickness is defined in terms of ratio over the base thickness, $t_c = r_f t_b$, with $r_f < 1$ in order to grant a shape which is easier to manufacture by fusion.

The objective of the optimization is the maximization of the heat transfer through the exchanger surface, subject to the respect of a performance, a compactness, and a cost constraint, namely:

- limit the pressure drop of the exhaust gas across the exchanger below 3 mmH_2O (that is, 29.42 Pa),
- limit the heat exchanger length below 700 mm,
- limit the volume of the SiSiC duct below 1,406.1 cm^3.

The reason behind the first constraint is due to the fact that a positive relative pressure is sought inside the kiln room, even though this pressure should be small enough, of the order of a few mmH_2O, so to limit the gas leakages through the kiln walls, since the room is not watertight. The second constraint simply limits the heat exchanger length for compactness reasons, while the latter is added in consideration of the fact that, according to the producer, one of the major costs in the burner production is the silicon carbide material cost: the given volume corresponds to that of the current heat exchanger configuration.

The first constraint will tend to discard the solutions having a low section area for the exhaust gas passage. The latter will force the optimization process in finding the optimum material distribution according to the given parameterization of the problem.

It can be noted that the volume of the finned tube can be computed analytically once its geometry is defined. From simple algebraic considerations, in fact, an approximation of the finned tube volume is given by the sum of the volume of the annulus and of the fins

$$V_e \approx \left[\left(D_o^2 - D_i^2\right)\frac{\pi}{4} + n_f h_f t_b \frac{1+r_f}{2}\right] l_e, \tag{1}$$

while a more rigorous formulation, considering also the curvature of the fins base and crest, results in

$$V_e = \left[\left(D_o^2 - D_i^2\right)\frac{\pi}{4} + n_f h_f t_b \frac{1+r_f}{2} - \frac{n_f D_o^2}{8}(\alpha_b - \sin\alpha_b) + \frac{n_f\left(D_o + 2h_f\right)^2}{8}(\alpha_c - \sin\alpha_c)\right] l_e, \tag{2}$$

where

$$\alpha_b = 2\arcsin\left(\frac{t_b}{D_o}\right) \quad , \quad \alpha_c = 2\arcsin\left(\frac{t_b r_f}{D_o + 2h_f}\right), \tag{3}$$

and the symbols introduced are graphically explained in Fig. 2. By solving Eq. (2) in l_e, for any configuration it is possible to set the proper heat exchanger length that meets the volume constraint, yet limiting its maximum value according to Table 3. This can be done since it is straightforward that the optimum exchanger configuration would necessarily use all the allowed heat exchanger pipe volume to maximize the heat transfer. Such a consideration makes it possible to reduce the number of variables by one, also removing

Table 3
Variables of the optimization and their ranges.

Variable & symbol		Range		FF levels
Fins number	n_f	10	20	5
Fins height	h_f	5.0 mm	20.0 mm	4
Gap between fin crest and insulating wall	g	2.0 mm	10.0 mm	3.
Fins thickness at the base	t_b	6.0 mm	9.0 mm	3
Fins thickness ratio	r_f	0.5	0.99	3
Heat exchanger length	l_e		700.0 mm	N./A.

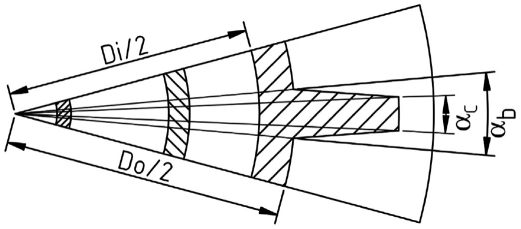

Fig. 2. Geometrical meaning of the symbols introduced in Eq. (2).

the volume and the length constraints. In this way we reduce to a 5 variables, 1 constraint, 1 objective function optimization problem.

From the algorithmic point of view, the Nelder & Mead simplex method [24] is used for the optimization. The efficiency and the stability of this method in handling unconstrained optimization problems is very well known. However, when dealing with constraints the method can fail in finding a proper optimum also for very simple problems. Similar limitations are found in other *deterministic* optimization algorithms as well, and must be indirectly ascribed to the *local* nature of the algorithm.

In order to prevent misconvergence and obtain a more general insight over the design space, the optimization is preceded by a Full Factorial Design of Experiments (FF-DOE). The optimization process is then repeated a few times, either starting from a random simplex in the design space, or from a simplex localized around the most performing areas of the design space according to the FF analysis. The FF levels chosen for the variables are summarized in Table 3, they are equally spaced within the ranges, and result in a 540 samples DOE overall.

It is expected that the 25 kW operating condition will be subject to more severe misconvergence problems due to the difficulties in respecting the pressure constraint. Compared to the 12.5 kW case in fact, the mass flow rates are double and the pressure drop is expected to be up to four times higher for a given geometry configuration. This will probably lead to rather different optimum configurations overall.

3. Results

The current configuration of the industrial heat exchanger investigated returns a heat transfer of 1,593.2 W against a pressure drop of 12.07 Pa when the burner is operated at 12.5 kW of thermal power. At 25 kW, the heat transfer grows to 2,155.9 W while the pressure drop reaches 30.03 Pa, thus slightly violating the given pressure drop constraint.

3.1. 12.5 kW case

When the burner is operated at 12.5 kW of thermal power the FF-DOE analysis returns 349 feasible designs out of 540 simulations performed (64.6%). By feasible design a configuration respecting the pressure drop constraint is intended. Following the FF, three runs of the Nelder & Mead simplex optimization algorithm are performed; in these optimizations the initial simplex is randomly initialized accordingly to the design space limits summarized in Table 3. We refer to these optimizations with the term "scratch start". Finally, three more simplex optimizations are performed on a restricted design space, chosen from the experience gained from the first two steps of the optimization, and centred around the best configurations previously found. We refer to these optimizations with the term "guided start". The optimum configurations found at each step of the optimization process are summarized in Table 4, only the best simplex optimization out of each set is reported.

In the guided start optimization, for the 12.5 kW case, the ranges of the variables were set as follows: $n_f \in [14.5, 18.0]$, $h_f \in [8.0\text{ mm}, 13.0\text{ mm}]$, $g \in [4.0\text{ mm}, 6.5\text{ mm}]$. t_b and r_f were fixed at 6.0 mm and 0.5 respectively since from the previous simulations it was evident that thinner fins were leading to a better overall exploitation of the material in view of heat transfer enhancement.

Finally, the guided start optimum configuration had to be adjusted in order to get an integer fins number. Solutions with $\lfloor n_f \rfloor$ and $\lceil n_f \rceil$ fins were tested by changing the fins height so to meet the volume constraint, and adapting the gap to meet the pressure constraint. The result of this process is reported in the last row of Table 4. Compared to the current configuration, the optimum heat exchanger is able to attain a 10.8% heat transfer enhancement yet respecting the pressure and the volume constraints when operated at 12.5 kW of thermal power.

3.2. 25 kW case

When the burner is operated at 25 kW of thermal power the FF-DOE analysis returns 179 feasible designs out of 540 simulations performed (33.1%). As expected the number of feasible configurations found is much lower, meaning that with this operating condition it is more difficult to respect the pressure drop constraint due to the larger mass flow rates. The optimization procedure followed in this case is the same used for the 12.5 kW case and previously described. The results are reported in Table 5.

In the guided start optimization, for the 25 kW case, the ranges of the variables were set as follows: $n_f \in [11.0, 14.5]$, $h_f \in [13.0\text{ mm}, 18.0\text{ mm}]$, $g \in [4.0\text{ mm}, 6.5\text{ mm}]$. t_b and r_f were fixed at 6.0 mm and 0.5 respectively.

Compared to the current configuration, the optimum heat exchanger is able to attain a 6.3% heat transfer enhancement yet respecting the pressure and the volume constraints when operated at 25 kW of thermal power.

3.3. Comments

It is noted how the optimum configurations always meet the maximum length constraint of 700 mm; this suggests that, if the heat exchanger compactness would not be of interest, the optimum material distribution would require the fins to be removed at all and the ducts to be made longer.

Fig. 3 compares the current fin shape to the optimum fin shape found for the different operating conditions investigated. The two optimum configurations are quite different from each other, this is mainly due to the pressure constraint. For the 12.5 kW case, in fact, the constraint is less critical, allowing the exhaust gas duct section area to be smaller, and, as a consequence, the fins to be shorter and more numerous. The compactness of the duct section and the larger wetted area positively affect the heat exchanger efficiency as will be showned in the following. On the contrary, for the 25 kW case, a larger exhaust gas duct section area is needed, and the fins must be longer to prevent the chance that a portion of the exhaust gases would pass through the heat exchanger keeping far from the exchanger wetted surface.

In terms of energy efficiency, this suggests that an industrial roller kiln with recuperative burners, should preferably be equipped with different kind of burners. In fact, even though the burners mainly work under steady state operating conditions, these conditions are different for each location of the kiln depending on a series of factor: first of all whether in a given area the product must be warmed up quickly (high thermal power at the burners needed)

Table 4
Optimum configurations found at each step of the optimization process, 12.5 kW case.

Step	Heat transfer [W]	Pressure drop [Pa]	Gain	Optimum configuration						
				n_f	f_h [mm]	g [mm]	t_b [mm]	t_r	l_e [mm]	V_e [cm^3]
Current	1593.2	12.07								
FF-DOE	1742.5	26.78	9.4%	17.5	10.0	6.0	6.0	0.50	700.0	1370.9
Scratch start	1748.1	28.42	9.7%	15.9	10.5	5.2	6.7	0.51	700.0	1405.2
Guided start	1767.9	27.65	11.0%	16.5	11.2	4.8	6.0	0.50	700.0	1402.5
Optimum	1765.9	29.09	10.8%	17	11.0	4.9	6.0	0.50	698.6	1406.1

Table 5
Optimum configurations found at each step of the optimization process, 25 kW case.

Step	Heat transfer [W]	Pressure drop [Pa]	Gain	Optimum configuration						
				n_f	f_h [mm]	g [mm]	t_b [mm]	t_r	l_e [mm]	V_e [cm^3]
Current	2155.9	30.03								
FF-DOE	2270.9	25.03	5.3%	12.5	15.0	6.0	6.0	0.50	697.2	1406.1
Scratch start	2264.9	29.30	5.1%	11.1	15.1	4.5	6.3	0.56	700.0	1401.3
Guided start	2296.9	29.15	6.5%	12.6	14.7	5.3	6.0	0.50	700.0	1406.0
Optimum	2291.9	29.07	6.3%	13	14.3	5.8	6.0	0.50	699.8	1406.1

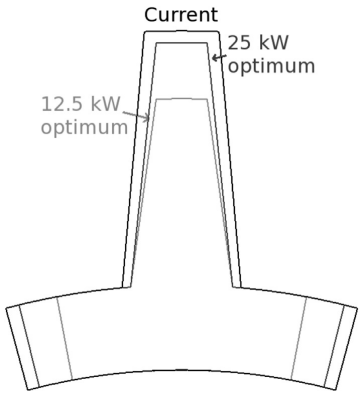

Fig. 3. Current versus optimum fin shapes.

or be kept at a certain temperature (low thermal power at the burners needed).

Table 6 analyses the current and the optimum configurations in terms of temperature jump of the various flow streams across the exchanger, heat exchanger efficiency, and the distribution of the total heat transferred between the primary and the secondary air. The gas stream is not reported as it undergoes a negligible temperature jump compared to the other fluids. The heat exchanger efficiency is computed as the ratio between the heat transfer rate and the sensible enthalpy of the exhaust gas entering the heat exchanger.

Table 6
Current versus optimum configurations in terms of bulk temperature differences between the inlet and the outlet sections, heat exchanger efficiency, and heat transfer distribution between primary and secondary air.

		Current		Optimum	
		12.5 kW	25 kW	12.5 kW	25 kW
Exhaust gas ΔT_b	[°C]	−222.0	−149.3	−241.2	−157.9
Secondary air ΔT_b	[°C]	+421.3	+290.2	+463.5	+307.8
Primary air ΔT_b	[°C]	+21.0	+6.8	+28.8	+9.1
Exchanger efficiency	[%]	19.1	12.9	21.1	13.7
Primary air heat fraction	[%]	2.01	0.95	2.48	1.21
Secondary air heat fraction	[%]	97.99	99.05	97.52	98.79

It is shown how the optimum burner configurations are more efficient and they are able to induce a stronger warm up of both primary and secondary air. Yet, the primary air warm up is still moderate, and this is a positive aspect in view of limiting the burner NO_x production rate. The same warm up effect can be seen from Fig. 4 where the effects of the different burner configurations on the temperature distribution along the heat exchanger is shown. From the figure it is also evident the large radial temperature gradient in the secondary air region.

To conclude, the thermal resistance network analysis [25] of the current and the optimum configurations is presented. The system at hand can be seen as a sequence of three series thermal resistances: the convective resistance between the exhausts and the exchanger wall (R_x), the conductive resistance through the exchanger wall (R_e), and the convective resistance between the secondary air and the exchanger wall (R_s). It is not of interest, for the problem at hand, to continue the analysis further, down to the methane passage. Considering the heat exchanger between the exhaust gas and the secondary air we can write that the overall rate of heat transfer ($\dot{Q}$) equals the log mean temperature difference between the two fluids (ΔT_m), divided by the total thermal resistance ($R_t = R_x + R_e + R_s$)

$$\dot{Q} = \frac{\Delta T_m}{R_t} \tag{4}$$

where

$$\begin{aligned} \Delta T_m &= \frac{(T_{x,1} - T_{s,1}) - (T_{x,2} - T_{s,2})}{\ln\left(\frac{T_{x,1} - T_{s,1}}{T_{x,2} - T_{s,2}}\right)} \\ &= \frac{(T_{x,in} - T_{s,out}) - (T_{x,out} - T_{s,in})}{\ln\left(\frac{T_{x,in} - T_{s,out}}{T_{x,out} - T_{s,in}}\right)} \end{aligned} \tag{5}$$

and the subscripts 1 and 2 refer to the extremity sections of the heat exchanger. Rewriting Eqs. (4) and (5) for the three thermal resistance separately the contribution of each part to the total thermal

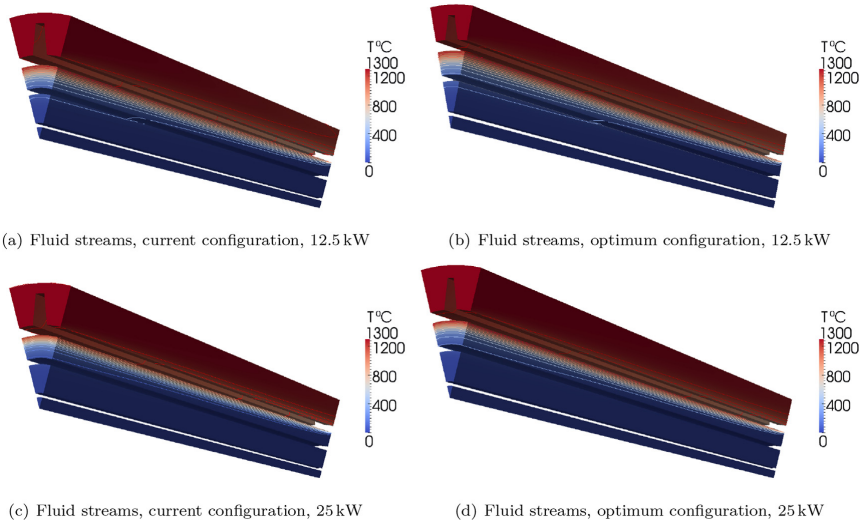

(a) Fluid streams, current configuration, 12.5 kW (b) Fluid streams, optimum configuration, 12.5 kW

(c) Fluid streams, current configuration, 25 kW (d) Fluid streams, optimum configuration, 25 kW

Fig. 4. Temperature distributions along the heat exchanger; the contour lines in the images are traced every 100° C.

Table 7
Thermal resistance network analysis results.

		Current		Optimum	
		12.5 kW	25 kW	12.5 kW	25 kW
R_x	[K/kW]	110.5	85.8	79.2	80.4
R_e	[K/kW]	6.7	6.9	5.5	6.6
R_s	[K/kW]	477.9	395.0	434.4	366.0
R_t	[K/kW]	595.2	487.7	519.0	453.0
R_x	[%]	18.57	17.59	15.26	17.75
R_e	[%]	1.13	1.42	1.06	1.46
R_s	[%]	80.30	80.99	83.69	80.80

resistance can be investigated. The results of this analysis are summarized in Table 7.

It can be seen that improving the heat transfer on one side of the exchanger always impacts positively on all the three resistance terms. In fact, the log mean temperature difference is always reduced, while the heat trasfer rate augmented. Yet the entity of the reduction is different for the three terms. Of course the largest impact (above 80 %) on the total thermal resistance is given by the convective term on the secondary air side. From one side this means that the fins on the exhausts side are indeed effective, on the other side it means that at this stage working on the external fins geometry only allows for marginal improvements of the heat transfer rate. Addressing the secondary air passage would lead to a better exploitment of the heat exchanger, and considering the narrowness of the passage this could better be addressed by swirling the flow more than by adopting extended surfaces.

4. Conclusions

The heat recovery capacity of a recuperative burner for applications in industrial continuous kiln is investigated by means of CFD. The heat exchanger layout is optimized under different operating condition by means of a suitable optimization procedure. The goal of the optimization is the maximization of the heat transfer of the recuperative heat exchanger under cost, compactness, and pressure drop constraints.

The optimum configurations found, according to the simulations, are able to enhance the heat transfer capacity of the recuperative heat exchanger by 10.8 % when the burner of operated under low thermal power conditions (namely 12.5 kW), and by 6.3 % when the burner is operated under high thermal power conditions (namely 25 kW). This heat transfer enhancement may translate into a reduced burner fuel consumption of 1.4 % and 0.5 % for the two operating conditions respectively. Despite being an apparently modest improvement, considering the typical fuel consumption of an industrial kiln for tiles production, this may translate into a reduced operating cost of approximately 17,000 euros per year, and a reduced carbon footprint of 170 tons of carbon dioxide per year for a single kiln with no additional production costs.

Due to the rather different optimum layouts found for the heat exchanger under the different burner operating conditions, for a better exploitment of the advantages of an optimized heat recovery device, it is suggested to adopt different heat exchangers configurations for the different portions of the kiln.

References

[1] A. Mezquita, J. Boix, E. Monfort, G. Mallol, Energy saving in ceramic tile kilns: cooling gas heat recovery, Appl. Therm. Eng. 65 (2014) 102–110.
[2] V. Karamarković, M. Marašević, R. Karamarković, M. Karamarković, Recuperator for waste heat recovery from rotary kilns, Appl. Therm. Eng. 54 (2013) 470–480.
[3] M. Cavazzuti, M.A. Corticelli, A. Nuccio, B. Zauli, CFD analysis of a syngas-fired burner for ceramic industrial roller kiln, P I Mech. Eng. C J Mech. 227 (2013) 2600–2609.
[4] M. Cavazzuti, M.A. Corticelli, G. Masina, R. Saponelli, CFD analysis of a syngas fired industrial tiles kiln module, Eng. Appl. Comp. Fluid 7 (2013) 533–543.
[5] D.A. Reay, A review of gas-gas heat recovery systems, Heat. Recov Syst. 1 (1980) 3–41.
[6] C.-H. Hwang, S. Lee, C.-E. Lee, The effect of turbulence intensity of ambient air flow on NO_x emissions in H_2/air nonpremixed jet flames, Int. J. Hydrogen Energy 33 (2008) 832–841.

[7] J.A. Wunning, J.G. Wunning, Flameless oxidation to reduce thermal NO-formation, Prog. Energy Combust. 23 (1997) 81–94.
[8] C. Galletti, A. Parente, L. Tognotti, Numerical and experimental investigation of a MILD combustion burner, Combust. Flame 151 (2007) 649–664.
[9] T.N. Demayo, V.G. McDonell, G.S. Samuelsen, Robust active control of combustion stability and emissions performance in a fuel-staged natural-gas-fired industrial burner, P Combust. Inst. 29 (2002) 131–138.
[10] B. Yu, J.H. Nie, Q.W. Wang, W.Q. Tao, Experimental study on the pressure drop and heat transfer characteristics of tubes with internal wave-like longitudinal fins, Heat. Mass Transf. 35 (1999) 65–73.
[11] C. Yildiz, Y. Biçer, D. Pehlìvan, Influence of fluid rotation on the heat transfer and pressure drop in double-pipe heat exchangers, Appl. Energ. 54 (1996) 49–56.
[12] H. Kahalerras, N. Targui, Numerical analysis of heat transfer enhancement in a double pipe heat exchanger with porous fins, Int. J. Numer. Method H. 18 (2008) 593–617.
[13] N. Nagarani, K. Mayilsamy, A. Murugesan, G.S. Kumar, Review of utilization of extended surfaces in heat transfer problems, Renew. Sust. Energ. Rev. 29 (2014) 604–613.
[14] R.V. Rao, V.K. Patel, Thermodynamic optimization of cross flow plate-fin heat exchanger using a particle swarm optimization algorithm, Int. J. Therm. Sci. 49 (2010) 1712–1721.
[15] R. Selbaş, Ö. Kızılkan, M. Reppich, A new design approach for shell-and-tube heat exchangers using genetic algorithms from economic point of view, Chem. Eng. Process 45 (2006) 268–275.
[16] S.H. Chong, K.T. Ooi, T.N. Wong, Optimisation of single and double layer counter flow microchannel heat sinks, Appl. Therm. Eng. 22 (2002) 1569–1585.
[17] K. Foli, T. Okabe, M. Olhofer, Y. Jin, B. Sendhoff, Optimization of micro heat exchanger: CFD, analytical approach and multi-objective evolutionary algorithms, Int. J. Heat. Mass Tran 49 (2006) 1090–1099.
[18] R. Hilbert, G. Janiga, R. Baron, D. Thévenin, Multi-objective shape optimization of a heat exchanger using parallel genetic algorithms, Int. J. Heat. Mass Tran 49 (2006) 2567–2577.
[19] A.K. Gholap, J.A. Khan, Design and multi-objective optimization of heat exchangers for refrigerators, Appl. Energy 84 (2007) 1226–1239.
[20] G.N. Xie, B. Sunden, Q.W. Wang, Optimization of compact heat exchangers by a genetic algorithm, Appl. Therm. Eng. 28 (2008) 895–906.
[21] J. Guo, L. Cheng, M. Xu, Multi-objective optimization of heat exchanger design by entropy generation minimization, J. Heat. Trans T ASME 132 (2010) 081801.
[22] B. Selma, M. Désilets, P. Proulx, Optimization of an industrial heat exchanger using an open-source CFD code, Appl. Therm. Eng. 69 (2014) 241–250.
[23] M.M.A. Bhutta, N. Hayat, M.H. Bashir, A.R. Khan, K.N. Ahmad, S. Khan, CFD applications in various heat exchangers design: a review, Appl. Therm. Eng. 32 (2012) 1–12.
[24] J.A. Nelder, R. Mead, A simplex method for function minimization, Comput J. 7 (1965) 308–313.
[25] Y.A. Çengel, J.M. Cimbala, R.H. Turner, Fundamentals of Thermal-Fluid Sciences, McGraw-Hill, 2012.

Appendix B

Paper presented at the *ASME-ATI-UIT 2015 Conference on Thermal Energy Systems: Production, Storage, Utilization and the Environment*, held in Naples (Italy) on May 17-20, 2015

ASME-ATI-UIT 2015 Conference on Thermal Energy Systems: Production, Storage, Utilization and the Environment
17 - 20 May, 2015, Napoli, Italy

OPTIMIZATION OF RECUPERATIVE BURNERS FOR INDUSTRIAL KILNS THROUGH CFD SIMULATION

Elia Agnani*, Marco Cavazzuti, Mauro A. Corticelli

Università degli Studi di Modena e Reggio Emilia – Dipartimento di Ingegneria "Enzo Ferrari",
via Pietro Vivarelli 10, 41125, Modena

ABSTRACT

An optimization of the shape of a recuperative burner for industrial furnaces for tiles production is presented. The aim of the study is the maximization of the energy recovery from exhaust gas across a heat exchanger in order to pre-heat the combustion air. The study is carried out by means of CFD simulations. Eleven geometric parameters have been chosen and varied individually in an introductory sensitivity analysis. Useful information on the parameters influence have been thus obtained. Due to the large grid size and computing times, a direct optimization has been deemed unfeasible for our purpose. In its place, a fine tuning of the solution has been achieved by investigating the parameters interactions and finding a rather linear superposition of the effects. A reduction of the burner fuel consumption of almost 5% has been attained without affecting the markers of the product firing quality, such as the temperature profile on the tiles floor along the kiln room.

Keywords: *Recuperative burner, CFD, Optimization*

INTRODUCTION

Continuous roller kilns, such as those widely used in the ceramic tiles industry, can reach a few hundred meters in length. The product is fired by several hundred burners placed along the lateral surrounding walls. The burners expel hot gases at high temperature directly into the kiln room generating a large amount of thermal power, which is not easy to exploit in its entirety. According to [1], the firing process, where the burners comes into play, was identified as the most critical process in the tiles life cycle in terms of pollution and energy consumption. Part of the thermal power is absorbed by the product, while another part is dispersed across the furnace walls. A single intake manifold, located at the tiles entrance section, draws the hot exhaust gases, with their residual enthalpy, and sends them to a global heat recovery system. With recuperative burners it is possible to decentralise the heat recovery, appointing it to the local burners themselves. The most common layout for this kind of system consists in a double pipe heat exchanger where the exhaust gas flows in an external coaxial tube placed around the burner body [2]. The high enthalpy exhaust gas, pre-heating the combustion air, can thus be better exploited before being sent to a global heat exchanger system for further recovery.

In recent years Computational Fluid Dynamics (CFD) has proved to be reliable and efficient, and can be considered a viable alternative to experimental analyses in many industrial applications. For instance, CFD analyses have been carried out on cracking furnaces, with [3] and [4] mainly focusing on flow patterns and heat transfer in the firing zone, rather than on the burners. On the other hand, to the author's knowledge, a paltry number of studies on continuous roller kilns in ceramic industry is available in literature. In [5] the temperature and velocity distributions on a module of an industrial kiln are investigated in terms of temperature uniformity on the tiles floor for different synthesis fuel gases used in place of methane. A general overview of a whole industrial furnace for ceramic tiles is given in [6], with regard to the evolution of temperature, pressure and oxygen content along the firing zone. The study gives also an esteem of the energy savings achievable by using the hot air from the cooling zone as combustive agent in the firing process. Non-recuperative industrial burners have been modelled by means of CFD in [7] to assess the behaviour of the system in terms of temperature, oxygen mass fraction and velocity distributions using different synthesis gases as fuel; in [8] EDC combustion model is implemented and tested with an open source CFD toolbox on a simple burner geometry using several RANS models. On the contrary, the available literature on recuperative burners is still scanty, [9] and [10] modelled reheating furnaces used in steel industry and equipped with recuperative burners, showing the capability of CFD to provide information on these systems; however the double pipe heat exchanger is not simulated in its entirety and the focus is mainly on the furnace environment.

The main concern about self-recuperative burners is represented by the larger NO_x formation rates induced by the higher flame temperatures occurring by pre-heating the combustion air. In such cases, the enhancement of turbulence or the adoption of staged combustion can help in mitigating NO_x production [11]. In recent years, flameless combustion received increasing attention from researchers interested in burners [12]. This technique consists in the recirculation of a given amount of exhaust gases into the combustion chamber, so to smooth out the flame temperature peaks and reduce NO_x formation drastically [13]. Despite this, flameless combustion has not yet spread in industrial applications due to the additional complexity in the burner design given by the need of an exhaust gas recirculation system.

In the present paper, we address a self-recuperative burner for industrial kilns employed in ceramic tiles manufacture. Because of the modest extension of the wetted area and the low residence time, the double pipe heat exchanger solution may not be the most efficient, and Ortona *et al.* [14] already tried

*Corresponding author: elia.agnani@unimore.it

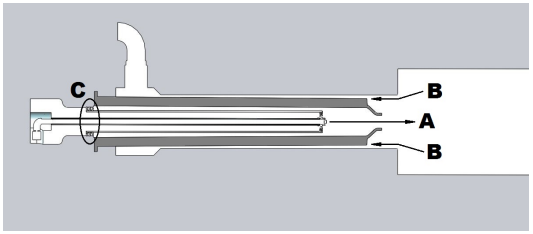

Figure 1. Burner configuration.

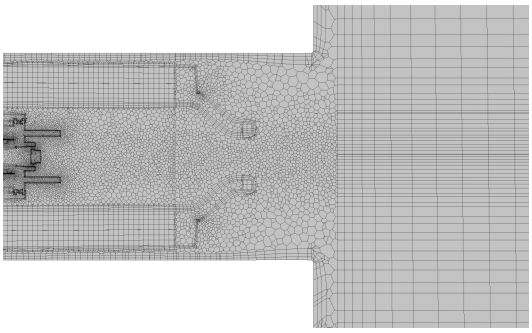

Figure 2. Detail of the computational grid.

to enhance the efficiency of such a heat exchanger for similar applications. Despite this limit, the optimization of this simple geometry is a valuable work, since more complex and thermal efficient strategies may not comply with industrial constraints such as easy manufacturability, resistance to high temperature, need for low maintenance, low pay-back time, and so on. The investigation is carried out by means of CFD simulations. A sensitivity analysis involving eleven geometric parameters has been performed in order to maximize the amount of energy recovered from the exhaust gas across the heat exchanger walls. The parameters interactions have also been addressed.

PROBLEM DEFINITION

Numerical Domain and Mesh

The system studied in the present paper consists in a recuperative burner heating a small chamber, as shown in Fig. 1. In order to limit the simulations domain, for computational reasons, the burner expels the exhaust gas in a small chamber (section A) in place of the much larger kiln environment, and the fluids are entirely sucked through the heat exchanger (section B). This configuration is different from the real kiln operating condition, yet it has been deemed to be the most suitable layout for carrying out a series of preliminary experimental investigations used to validate the CFD model and test the burner operation. In zone C (Fig. 1) the combustion air coming from upstream is split in primary air, going straight to the burner's head, and secondary air, passing through a swirling component and then put in direct contact with the internal wall of the heat exchanger.

The numerical model, including the mesh generation and the simulations, has been arranged using the ANSYS suite. A series of parameters related to the shape of the heat exchanger and the fluid flow on both of its sides have been identified and tested in the context of a parametric study. The workflow automatically changes the geometry according to the parameters chosen, generates a new computational grid for the domain, and finally solves and post-processes the fluid dynamic problem.

The particular meshing process of this complex geometry requires simple and robust meshing criteria in order to avoid the crashing of the grid generation infrastructure. Therefore, except for some "sweepable" bodies, meshed with hexahedra, the fluid part is characterized by boundary layers on the walls, and a fully tetrahedral grid, then converted into polyhedral (Fig. 2). Thus, interruptions of the global workflow are prevented. The grid is large but not so expensive from the computational point of view (the mean size is around 3 million cells), and the accuracy of the solution is expected to be reasonable [15] for the comparative purpose of the analysis.

Experimental Facilities

An experimental campaign has been carried out in order to validate the CFD model, as previously mentioned. A single burner has been tested while working in a particular configuration, with the exhaust gas expelled into a small closed room instead of the wider kiln environment. The internal dimensions of the room are reported in Fig. 3, the walls are made of consecutive layers of bricks and insulating material, and the whole structure is enveloped in a sheet of aluminium in order to minimize the leakages of the combustion products through the wall, and the external radiation. The exhaust gas was then sucked through the heat exchanger with the aid of an electric fan to depressurize the extraction duct.

The system has been equipped with a series of thermocouples and pressure probes. Orifice plates have been placed in the air and the fuel ducts, as well as in the extraction duct in order to measure the flow rates. In particular, temperatures measured by the thermocouples A (at heat exchanger inlet) and B (at the bottom of the room), as shown in Fig. 3, have been compared to the ones predicted by the CFD simulation.

The experimental infrastructure took about 36 hours to reach stability due to the large thermal inertia of the walls. The measurements of temperatures, pressures, and flow rates have been used to set the boundary conditions of the simulation, so to model the same system configuration.

Simulation Models

The simulations are performed with ANSYS Fluent. A steady-state pressure-based implicit solver is adopted, with pressure and velocity fully coupled and pseudo-transient method to implicitly under-relax the problem. The first order upwind discretisation has been adopted for all the variables to guarantee more stability to the computation.

The combustion process has been modelled with the Finite-Rate/Eddy-Dissipation model that combines the Eddy-Dissipation model, where the reaction rates are controlled only by turbulence [16], and the Finite-Rate approach where the reaction rates are assessed with more computationally expensive Arrhenius formulas. With this combined model both the reaction rates are computed, and the minimum taken. Thus the combustion is prevented by Arrhenius rate in certain zones, while, where the ignition has occurred, the eddy-dissipation rate, which is generally smaller, actually governs the reaction

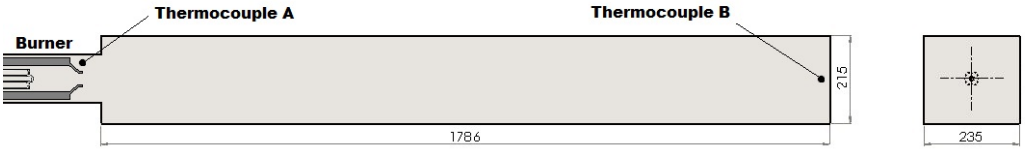

Figure 3. Dimensions (in mm) of the experimental room with the positioning of the benchmark thermocouples.

Table 1. Air and fuel compositions in terms of mass (M.F.) and volume fractions (V.F.).

Components	Air		Fuel	
	V.F.	M.F.	V.F.	M.F.
CH_4	– %	– %	88.00 %	79.90 %
C_2H_6	– %	– %	9.20 %	15.66 %
O_2	21.02 %	23.36 %	– %	– %
H_2O	0.61 %	0.38 %	– %	– %
N_2	78.37 %	76.26 %	2.80 %	4.44 %

process. In non-premixed flames, where the fuel burns quickly in the reaction zones, like the one presented here, complex chemical kinetic rates can be neglected without affecting the solution. This is acceptable unless more than two-step reaction mechanisms are taken into account. Multi-step mechanisms in fact are based on Arrhenius rates that are different for each reaction, while the eddy-dissipation model adopts the same turbulent rate for every reaction. In this study, two one-step mechanisms are employed. The compositions of the air and the fuel are reported in Tab. 1. The latter is a simplified composition of that of the methane gas commonly distributed in the italian national gas network, and is equivalent in terms of lower heating value (LHV=47.44 MJ/kg) and average molecular mass. Both methane and ethane participates in the combustion process with the following reactions:

$$CH_4 + 2O_2 \rightarrow CO_2 + 2H_2O \quad (1)$$

$$C_2H_6 + 3.5O_2 \rightarrow 2CO_2 + 3H_2O \quad (2)$$

No NO_x or soot formation model is included at this stage of the simulations.

For turbulence modelling a k-ω SST model has been adopted with low-Reynolds correction. Radiation effects have a great influence on the results and thus can not be neglected: they are modelled with the discrete ordinate method.

The air/fuel mixture, the specific heat, and the thermal conductivity are computed according to the mixing law, while the dynamic viscosity follows the Sutherland law.

Boundary Conditions

Data from the experimental campaign have been used to set the CFD model. Fixed mass flow rates of fuel and oxidizer have been imposed at the inlet sections and are reported in Tab. 2.

Table 2. Inlet and outlet boundary conditions.

Air mass flow rate	[g/s]	5.304
Fuel mass flow rate	[g/s]	0.274
Air inlet temperature	[°C]	26.5
Fuel inlet temperature	[°C]	26.5
Outlet Gauge Pressure	[Pa]	−73.6

According to the given fuel composition (see Tab. 1), under this operating conditions, the burner generates about 13 kW of thermal power, without considering the amount recovered from the exhausts. The stoichiometric air-fuel ratio $(A/F)_{st}$ for this case is 16.14, while the actual ratio adopted here is 19.37, because under typical working conditions the burners are operated with a 20 % excess of air. The ambient temperature is 26.5 °C, while the pressure measured at the outlet section is 73.6 Pa below the ambient value.

The walls are modelled through mixed boundary conditions. From the technical specifications of the materials of the experimental chamber wall, equivalent materials in terms of thermal resistance have been defined in the simulation code. Also the convective external resistance and the external radiative effects are modelled.

Sensitivity Analysis Set-up

Due to the grid size and the large number of equations taken into account, the computing time for a single run (about 24 hours on a 128 CPUs cluster) is large enough to make direct optimization inapplicable for our purpose. Therefore, a sensitivity analysis has been carried out varying eleven geometric parameters. Starting from a basic configuration, every parameter is individually switched to a minimum and to a maximum value as shown in Fig. 4. Thus, the overall number of simulations required for completing the sensitivity analysis is 23.

The range of variability of each parameter has been chosen in order to guarantee the manufacturability and the reliability of the burner during operation. Since this work is based on a real industrial case, for privacy reasons the values of the parameters can not be disclosed. Below is the list of parameters:

1. Position of the burner nozzle with respect to the room walls;
2. Length of the combustion chamber;
3. Length of the heat exchanger;
4. Dimension of the chamfer on the hole realised in the wall for housing the burner;
5. Length of the component that splits the air flow rate and

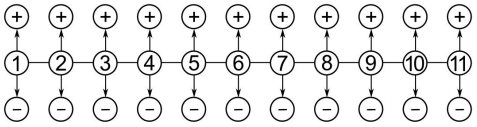

Figure 4. Schematic of starpoints DOE used for the sensitivity analysis.

Table 3. Comparison between experimental and numerical temperatures at the thermocouples.

Thermocouple	Experimental [°C]	Numerical [°C]
A	1171	1205
B	955	1051

impresses the swirl motion;
6. Angle of swirl impressed to the air;
7. Dimension and number of passages through the swirling component;
8. Number of fins of the heat exchanger;
9. Width of the fins;
10. Height of the fins;
11. Gap between the fins head and the burner housing hole.

RESULTS

Experimental Validation

The basic configuration of the sensitivity analysis, reproduces the layout of the experimental campaign. In the ANSYS Fluent model two probes have been virtually positioned at the same locations as the thermocouples A and B (see Fig. 3) in order to monitor the temperature trend during the simulation. The calculation lasted for about 24 hours and has been stopped after 10000 iterations, when the numeric residuals were steadily below 10^{-4}, and the temperatures at the probes stable.

Qualitative contours of temperature, velocity magnitude, and mass fraction of CH_4 (the main specie in fuel composition) along a slice of the computational domain are shown in Fig. 5. The numeric values in the legends are not reported due to privacy issues.

In Tab. 3 the results of the validation are reported. The numerical simulation overestimates the experimental results. At thermocouple A the matching is very good, while at thermocouple B the discrepancy is more evident, as the experiments report a more pronounced temperature drop along the chamber. This can be imputed to the gas leakages through the chamber wall (estimated to sum up to the 6 % of the total mass flow rate) registered during the experimental measures, but not modelled in the simulations.

Sensitivity Analysis

The 23 simulations of the sensitivity analysis have been examined in terms of numerical convergence and temperature stability. Every simulation has been accurately post-processed, and the heat exchanger efficiency computed. An estimate is also

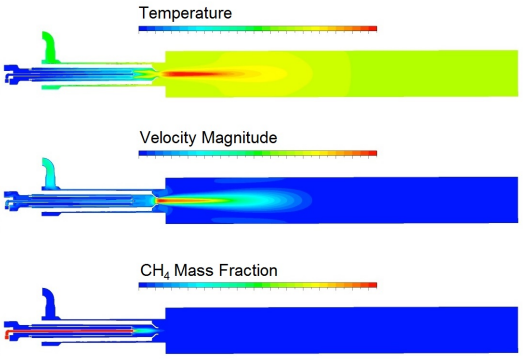

Figure 5. Trends of temperature, velocity magnitude, and CH_4 mass fraction along a longitudinal section of the domain.

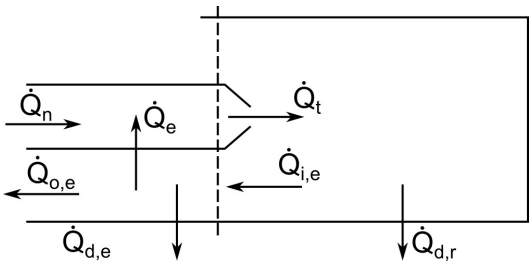

Figure 6. Thermal powers scheme for the investigated burner.

given of the fuel consumption reduction achievable, with respect to the basic configuration, under the same operating conditions, this is referred to simply with the term "gain" in the following. The heat exchanger efficiency η and the gain G are defined as follows.

In Fig. 6 a quick scheme of the thermal powers at play is shown. The nominal power $\dot{Q}_n$, generated by the combustion of the fuel, summed to the power recovered by the heat exchanger $\dot{Q}_e$, forms the total power $\dot{Q}_t$ supplied by the burner into the chamber. Part of the total power is dissipated through room walls $\dot{Q}_{d,r}$, while the remaining amount $\dot{Q}_{i,e}$ enters the heat exchanger. Of the latter, part is recovered $\dot{Q}_e$, part is dissipated through the burner walls $\dot{Q}_{d,e}$, and part exits the system with the exhaust gas $\dot{Q}_{o,e}$ and is sent to the global heat exchange system for further recovery.

All the thermal powers are obtained from the post-processing of the simulations in terms of fluxes through the domain patches. The efficiency of the heat exchanger is computed as the ratio between the power recovered along the heat exchanger $\dot{Q}_e$, and the thermal power available to the fluid at the exchanger inlet section $\dot{Q}_{i,e}$:

$$\eta = \frac{\dot{Q}_e}{\dot{Q}_{i,e}} \tag{3}$$

Table 4. Percentual gains of the design points of the sensitivity analysis.

parameter	1	2	3	4	5	6	7	8	9	10	11
max	−0.07	−1.23	0.86	0.10	0.07	−0.33	0.01	0.13	0.00	0.28	−0.03
basic					0.00						
min	0.24	1.08	−0.80	0.01	−0.08	0.39	0.06	−0.15	0.22	−0.15	0.21

The gain is defined as the difference between the recovered thermal power of a given configuration $\dot{Q}_{e,k}$ and the recovered thermal power of the basic configuration $\dot{Q}_{e,basic}$, divided by the nominal power $\dot{Q}_n$. For the generic configuration k, the gain G_k is:

$$G_k = \frac{\dot{Q}_{e,k} - \dot{Q}_{e,basic}}{\dot{Q}_n} \tag{4}$$

Thus, G is an indicator of the rise in the total power available for a given nominal power of fuel. It can also be considered an indicator of the potential fuel saving obtained under a given operating condition. In fact, in order to keep $\dot{Q}_t = \dot{Q}_n + \dot{Q}_e$ constant, if the recovery term rises, the combustible flow rate is lowered along with the nominal power.

In Tab. 4 the gains for all the 23 configurations tested are reported, of course the basic configuration has gain zero. For each parameter, the min-to-max gain variation gives an idea of the parameters influence on the thermal power recovery. From these considerations, some parameters can be neglected in the further analysis: *e.g.*, the realization of the chamfer (parameter 4) is a very expensive operation, while the effect it has on recovery is unremarkable. The same holds for the length of the swirl component (parameter 5), and for the number and the dimensions of its passages (parameter 7). Of course, the heat exchanger body should be kept as long as possible (parameter 3) because it affects significantly the thermal power recovery. On the contrary, the combustion chamber (parameter 2) has to be short, so that the combustion process is mainly completed outside the burner mixing room. This allows the temperature inside the mixing room to be lower, and prevents the chance to have backward heat flux on a small portion of the heat exchanger surface, where the hot fluid in the mixing room may warm up the exhaust gas.

Increasing the swirl impressed to the combustion air (parameter 6) also has a positive influence on the recuperative burner performances. In fact, by deflecting the flux, the effective heat transfer coefficient on the air side of the heat exchanger is increased. On the other hand, a significantly skewed swirl component may lead to very high pressure drops, thus reducing both the amount of secondary air, as well as the thermal power exchanged.

The four parameters related to the fins shape (parameters 8–11) have a moderate influence on the results, yet they must be strongly interconnected, and the simple sensitivity analysis carried out so far does not allow the investigation of their mutual interaction. Despite this, the sensitivity analysis gives useful information about the parameters impact on the results and, for such a problem, is a useful first-step operation to be followed by an optimization process or a manual fine tuning of the solution.

Solution Fine Tuning

After the sensitivity analysis, another simulation has been performed merging all the positive changes together in order to investigate, at least marginally, the combined effect of the parameters. A rather linear superposition of the effects was found. A direct optimization has been deemed unfeasible due to size of CFD model, and the computational time required. Yet, in the light of the results of this last simulation, a direct optimization would also have been of little interest for this specific case, due to the weak interactions between the parameters found. At this stage only the parameters having a significant influence on the results have been included. The remaining being left as in the basic configuration, in order to reduce the complexity and the cost of the burner.

With the new configuration (referred to as “Mod 1”) the gain grows up to 5 % as shown in Tab. 5. The optimum configuration was then checked in terms of temperature profile along the chamber floor (see Fig. 7). In fact, it is of the utmost importance that this temperature is as uniform as possible in that it is the primary marker of the product firing uniformity and quality. To increase temperature uniformity, in a real kiln operation, two staggered rows of burners are placed on the lateral walls of the kiln, facing each other. In our case, thus, it would be erroneous to consider a uniformity measure of the max-to-min temperature difference kind, since in a real kiln the colder portion in Fig. 7 would actually be warmed up by the facing burners. Then, to better focus on the left portion of the plot, we define as a performance measure the temperature difference ΔT_f between the maximum and the temperature by the burner nozzle on the room floor (coordinate zero in Fig. 7).

The difference between the “Mod 1” and the basic configurations is clear. For a quantitative comparison, in Tab. 5 the ΔT_f are reported. The improvements applied to the burner configuration, heavily affects the heat recovery, but also the geometry of the flame. In particular, the nozzle position with respect to the room walls (parameter 1), has a great influence on the floor temperature profile in the firing room.

Therefore another configuration (referred to as “Mod 2”) has been modelled and tested, where the nozzle position is unchanged from the basic configuration. The results show a modest reduction of the gain with respect to “Mod 1” (Tab. 5), on the other hand, the same temperature uniformity of the basic configuration is recovered, as shown in Fig. 7 and Tab. 5.

CONCLUSIONS

An optimized shape for the finned heat exchanger of a recuperative burner has been found. The influence of eleven geometric parameters over the heat flux from the exhaust gas to the combustion air has been investigated. The entire process was carried out by means of CFD simulations previously val-

Table 5. Results of the fine tuning configurations.

Configuration	G [%]	ΔT_f [K]
Basic	0.00	10.4
Mod 1	5.00	25.9
Mod 2	4.72	10.6

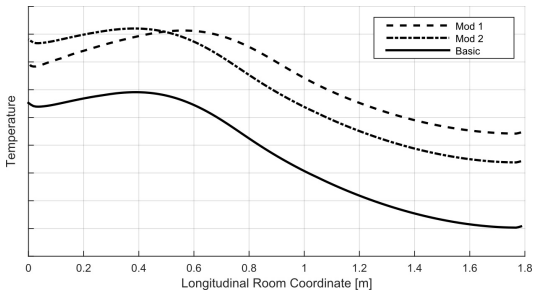

Figure 7. Temperature's profile along chamber floor in three analysed configurations.

idated with experimental tests. Two solutions have been proposed, improving the amount of thermal power recovered by the heat exchanger. The performance of these solutions have been compared to those of the basic burner configuration in terms of potential fuel savings due to better heat recoveries (gain), and temperature uniformity of the chamber floor as a marker of the product firing quality.

The first solution maximizes the heat flux through the exchanger surface, with a 5 % gain, but significant lack of temperature uniformity. The second, on the contrary, is able to address the temperature uniformity issue properly. Both cases guarantee a reasonable heat transfer efficiency improvement, with the adjustment of just a few geometrical parameters, mainly related to the double pipe heat exchanger shape.

Of course, the proposed solutions would be able to attain such performances under the assumption that the burner is operated at 13 kW of thermal power. For different operating conditions, also the working point of the heat exchanger and its efficiency would be affected. This recalls to the need of adopting different burner set-ups for the different burner operating conditions found in an actual kiln.

ACKNOWLEDGMENT

The authors thank SACMI Imola S.C. for the financial support and for providing services and facilities.

REFERENCES

[1] M.D. Bovea, E. Diaz-Albo, A. Gallardo, F.J. Colomer, J. Serrano, Environmental performance of ceramic tiles: Improvement proposals, Material and Design, 31(1), 2010, pp.35-41.

[2] D.A. Reay, A review of gas-gas heat recovery systems, Journal of Heat Recovery Systems, 1(1), 1981, pp.3-41.

[3] H. Guihua, W. Honggang, Q. Feng, Numerical simulation on flow, combustion and heat transfer of ethylene cracking furnaces, Chemical Engineering Science, 66(8), 2011, pp.1600-1611.

[4] A.J.M. Oprins, G.J. Heynderickx, Calculation of three-dimensional flow and pressure fields in cracking furnaces, Chemical Engineering Science, 58(21), 2003, pp.4883-4893.

[5] M. Cavazzuti, M.A. Corticelli, G. Masina, R. Saponelli, CFD analyses of syngas-fired industrial tiles kiln module, Engineering Applications of Computational Fluid Mechanics, 7(4), 2013, pp.533-543.

[6] A. Mezquita, J. Boix, E. Monfort, G. Mallol, Energy saving in ceramic tile kilns: Cooling gas heat recovery, Applied Thermal Engineering, 65(1-2), 2014, pp.102-110.

[7] M. Cavazzuti, M.A. Corticelli, A. Nuccio, B. Zauli, CFD analysis of a syngas-fired burner for ceramic industrial roller kiln, Proceedings of the Institution of Mechanical Engineers, Part C: Journal of Mechanical Engineering Science, 227(11), 2013, pp.2600-2609.

[8] E. Ghasemi, S. Soleimani, C.X. Lin, RANS simulation of methane-air burner using local extinction approach within eddy dissipation concept by OpenFOAM, International Communications in Heat and Mass Transfer, 54, 2014, pp.96-102.

[9] H. Sayah, M. Nemer, W. Nehme, D. Clodic, Computational fluid dynamics modeling of a self-recuperative burner and development of a simplified equivalent radiative model, Journal of Heat Transfer, 134(12), 2012.

[10] T. Ishii, C. Zhang, S. Sugiyama, Numerical simulations of highly preheated air combustion in an industrial furnace, Journal of Energy Resources Technology, Transactions of the ASME, 120(4), 1998, pp.276-284.

[11] C.H. Hwang, S. Lee, C.E. Lee, The effect of turbulence intensity of ambient air flow on NOx emissions in H2/air nonpremixed jet flames, International Journal of Hydrogen Energy, 33(2), 2008, pp.832-841.

[12] V. Fortunato, C. Galletti, L. Tognotti, A. Parente, Influence of modelling and scenario uncertainties on the numerical simulation of a semi-industrial flameless furnace, Applied Thermal Engineering, 76, 2015, pp.324-334.

[13] M.M. Huang, W.W. Shao, Y. Xiong, Y. Liu, Z.D. Zhang, F.L. Lei, Y.H. Xiao, Effect of fuel injection velocity on MILD combustion of syngas in axially-staged combustor, Applied Thermal Engineering, 66(1-2), 2014, pp.485-492.

[14] A. Ortona, D. Trimis, V. Uhlig, R. Eder, S. Gianella, P. Fino, G. D'Amico, E. Boulet, C. Chazelas, T. Gramer, E. Cresci, J.G. Wunning, H. Altena, F. Beneke, M. Debier, SiSiC heat exchangers for recuperative gas burners with highly structured surface elements, International Journal of Applied Ceramic Technology, 11(5), 2014, pp.927-937.

[15] S. Chalasani, E.A. Luke, V. Senguttuvan, D.S. Thompson, Assessing generalized mesh quality via CFD solution validation, 43rd AIAA Aerospace Sciences Meeting and Exhibit - Meeting Papers, 2005, pp.2927-2940.

[16] B.F. Magnussen, B.H. Hjertager, On mathematical modeling of turbulent combustion with special emphasis on soot formation and combustion, Symposium (International) on Combustion, 16(1), 1977, pp.719-729.

References

[1] M.D. Bovea, E. Diaz-Albo, A. Gallardo, F.J. Colomer, J. Serrano, Environmental performance of ceramic tiles: Improvement proposals, Material and Design, 31(1), 2010, pp.35-41.

[2] D.A. Reay, A review of gas-gas heat recovery systems, Journal of Heat Recovery Systems, 1(1), 1981, pp.3-41.

[3] J. Marino and Jared S. Kautman, Regenerative Burners or Oxy-fuel Burners for your furnace upgrade. June 2, 2011.

[4] C.H. Hwang, S. Lee, C.E. Lee, The effect of turbulence intensity of ambient air flow on NOx emissions in H2/air nonpremixed jet flames, International Journal of Hydrogen Energy, 33(2), 2008, pp.832-841.

[5] V. Fortunato, C. Galletti, L. Tognotti, A. Parente, Influence of modelling and scenario uncertainties on the numerical simulation of a semi-industrial flameless furnace, Applied Thermal Engineering, 76, 2015, pp.324-334.

[6] M.M. Huang, W.W. Shao, Y. Xiong, Y. Liu, Z.D. Zhang, F.L. Lei, Y.H. Xiao, Effect of fuel injection velocity on MILD combustion of syngas in axially-staged combustor, Applied Thermal Engineering, 66(1-2), 2014, pp.485-492.

[7] H. Guihua, W. Honggang, Q. Feng, Numerical simulation on flow, combustion and heat transfer of ethylene cracking furnaces, Chemical Engineering Science, 66(8), 2011, pp.1600-1611.

[8] A.J.M. Oprins, G.J. Heynderickx, Calculation of three-dimensional flow and pressure fields in cracking furnaces, Chemical Engineering Science, 58(21), 2003, pp.4883-4893.

[9] M. Cavazzuti, M.A. Corticelli, G. Masina, R. Saponelli, CFD analyses of syngas-fired industrial tiles kiln module, Engineering Applications of Computational Fluid Mechanics, 7(4), 2013, pp.533-543.

[10] A. Mezquita, J. Boix, E. Monfort, G. Mallol, Energy saving in ceramic tile kilns: Cooling gas heat recovery, Applied Thermal Engineering, 65(1-2), 2014, pp.102-110.

[11] M. Cavazzuti, M.A. Corticelli, A. Nuccio, B. Zauli, CFD analysis of a syngas-fired burner for ceramic industrial roller kiln, Proceedings of the Institution of Mechanical Engineers, Part C: Journal of Mechanical Engineering Science, 227(11), 2013, pp.2600-2609.

[12] H. Sayah, M. Nemer, W. Nehme, D. Clodic, Computational fluid dynamics modeling of a self-recuperative burner and development of a simplified equivalent radiative model, Journal of Heat Transfer, 134(12), 2012.

[13] T. Ishii, C. Zhang, S. Sugiyama, Numerical simulations of highly preheated air combustion in an industrial furnace, Journal of Energy Resources Technology, Transactions of the ASME, 120(4), 1998, pp.276-284.

[14] ANSYS Fluent Guide

[15] J.D. Anderson Jr., Computational Fluid Dynamics, 1995

[16] S.R. Turns, An introduction to combustion: concepts and applications, 2000

[17] D. Veynante, L. Vervisch, Turbulent combustion modeling, Progress in Energy and Combustion Science, 28, 2002, pp. 193-266.

[18] B.F. Magnussen, B.H. Hjertager, On mathematical models of turbulent combustion with special emphasis on soot formation and combustion, 16th Symp. on Combution, The Combustion Institute, 1976.

[19] S.V. Patankar, Numerical heat transfer and fluid flow, CRC Press., 1980.

[20] M. Cavazzuti, Optimization methods: from theory to design, Springer, 2013.

[21] A. Olsson, G. Sandberg, O. Dahlblom, On latin hypercube sampling for structural reliability analysis, Structural Safety, 25(1), 2003, pp. 47-68.

[22] W. Spendley, G.R. Hext, F.R. Himsworth, Sequentially application of simplex design in optimization and evolutionary operation, Technometrics, 4, 1962, pp. 441-461.

[23] J.A. Nelder, R. Mead, A simplex method for function minimization, Computer Journal, 7(4), 1965, pp. 308-313.

[24] A.V. Sudarev, Heat transfer and drag of a turbulent swirling air stream in the entrance section of an annular channel, Journal of engineering physics, 15(5), 1968, pp. 1049-1052

[25] S. Chapman, T.G. Cowling, The mathematical theory of non-uniform gases, Cambridge University Press, 1939.

[26] W. Sutherland, The viscosity of gases and molecular force. The London, Edinburgh, and Dublin Philosophical Magazine and Journal of Science, 36(223), 1893, pp. 507-531.

[27] D.G. Krige, A statistical approach to some mine valuation and allied problems on the Witwatersrand, Master's thesis of the University of Witwatersrand, 1951.